UNIVERSITY OF CALIFORNIA,
IRVINE

Mathematical modeling of tumor-microenvironment dynamics

DISSERTATION

submitted in partial satisfaction of the requirements
for the degree of

DOCTOR OF PHILOSOPHY

in Mathematics

by

Anna Konstorum

Dissertation Committee:
Professor John S. Lowengrub, Chair
Professor Marian L. Waterman
Professor Natalia Komarova

2015

DEDICATION

This thesis is dedicated to my grandmother, Inessa Bashneva. The strength and kindness she displayed under all the circumstances in her life have been a continuous source of motivation and inspiration for me.

TABLE OF CONTENTS

LIST OF FIGURES

LIST OF TABLES

ACKNOWLEDGMENTS

I would like to thank my advisor, Dr. John Lowengrub, for his unparalleled guidance and assistance throughout the thesis process. I would also like to thank my collaborators, including Dr. Marian Waterman, Dr. Thomas Hillen, Dr. Arthur Lander, and Stephanie Sprowl-Tanio for their valuable contributions. I am also grateful to my thesis committee, Dr. Lowengrub, Dr. Waterman, and Dr. Natalia Komarova.

I am grateful for the fellowships awarded by the National Institute for Biomedical Imaging and Bioengineering (NIBIB) and National Institute of Human Health and Child Development (NIHCD), which have allowed me to devote a majority of my doctoral years to research.

The permission to use copyrighted material in Chapter 2 of this thesis has been granted by American Scientific Publishers. The material originally appeared in Konstorum et al., J. Coupled Syst. Multiscale Dyn, 1(4), 459-467. I am grateful to the co-authors, Stephanie Sprowl-Tanio, Dr. Arthur Lander, Dr. Marian Waterman, and Dr. John Lowengrub, for their help in preparation of the manuscript. Dr. Lowengrub, the final author listed in this publication, directed and supervised research which contributes to the basis for the dissertation.

Finally, I would like to acknowledge the help of my family and friends without whom this thesis would not have come together. I would especially like to thank my father, Boris Konstorum, for his unwavering support.

CURRICULUM VITAE

Anna Konstorum

EDUCATION

Doctor of Philosophy in Mathematics **2015**
University of California, Irvine *Irvine, CA*

Master of Science in Mathematics **2013**
University of California, Irvine *Irvine, CA*

Master of Science in Physiological Sciences **2010**
University of California, Los Angeles *Los Angeles, CA*

Bachelor of Science in Biology **2005**
McGill University *Montreal, Quebec; Canada*

PUBLICATIONS

Konstorum, A., Sprowl, S.A., Lander, A.D., Waterman, M.L., Lowengrub, J.S. (2013) Predicting mechanism of biphasic growth factor action on tumor growth using a multi-species model with feedback control, **J. Coupled Syst. Multiscale Dyn**, 1(4), 459-467.

Lim M., Hou A., Congdon N., Chua J. (2013) Feature Identification for Colon Tumor Classification, **SIAM Undergraduate Journal Online**, 6, 264-274. (Served as faculty advisor).

Konstorum, A., Sprowl, S.A., Lander, A.D., Waterman, M.L., Lowengrub, J.S. (2013) Elaboration of a multispecies model of solid tumor growth with tumor-host interactions, **Proc. 3rd Int Conf. Appl. Nonlinear Dynamics**, Seattle, WA Springer Verlag p.295-303.

Zhou, B., Tieu, K.H., Konstorum, A., Duong, T., Wells, WM, Brown, G.G., Stern, H., and Shahbaba, B. (2013) A hierarchical modeling approach to data analysis and study design in a multi-site experimental fMRI study, **Psychometrika**, 78(12), 260-278.

Wang, T.T., Tavera-Mendoza, L., Laperriere, D., Nagai, Y., Burton MacLeod, N., Libby, E., Zhang, R., Bourdeau, V., Konstorum, A., Lallemant, B., Mader, S. and White, J.H. (2005) Large-scale in silico and microarray-based genomic screening of 1,25-dihydroxyvitamin D3 target genes, **Mol. Endocrinol**. 19, 2685-95.

TEACHING AND OUTREACH

Graduate Assistant (NSF-sponsored iCAMP) **2012-2015**
University of California, Irvine *Irvine, CA*

Teaching Assistant (Calculus AB, Numerical Analysis) **2014**
University of California, Irvine *Irvine, CA*

Teaching Assistant (Physiology and Systems Biology) **2008-2010**
University of California, Los Angeles *Los Angeles, CA*

ABSTRACT OF THE DISSERTATION

Mathematical modeling of tumor-microenvironment dynamics

By

Anna Konstorum

Doctor of Philosophy in Mathematics

University of California, Irvine, 2015

Professor John S. Lowengrub, Chair

In this thesis we explore tumor-microenvironment dynamics using three models of decreasing complexity. The first is a multispecies, spatiotemporal model of tumor development in tumor-derived growth factor responsive stroma that is activated to secrete the tumor growth and dispersal activator HGF. We show that HGF-induced invasive tumor morphology is promoted by increased heterogeneity at the tumor-host boundary. The second model is a system of ODEs that explores hypotheses based on experimental observations that tumor growth inhibition can occur at high levels of HGF. The model allows for the prediction of the molecular mechanism of HGF action via dose-response curve analysis. The final model is a system of two ODEs for stem cell and chemical activator of stem cell self-renewal concentrations, and allows for the approximation of the separatrix of the phase space that divides the space into basins of attraction for tumor eradication and tumor maintenance. The multiple models allow us to consider tumor-host interactions at various levels of abstraction and thus to infer both qualitative and quantitative results regarding tumor response to host and tumor-derived growth activators.

Introduction

Background

The tumor microenvironment consists of vascular endothelial cells, pericytes, immune inflammatory cells, and cancer associated fibroblasts (CAFs), all which contribute to the hallmarks of cancer [38, 36]. CAFs include both tissue-derived fibroblasts and recruited myofibroblasts, and promote tumor invasion and metastasis via secretion of growth factors and extracellular matrix (ECM) components [50, 4]. CAF-derived Hepatocyte Growth Factor, HGF, contributes to a pro-tumorigenic environment by activating its cognate receptor, c-Met. High HGF/c-Met activity has been identified in a large number of cancers and is correlated with more severe tumor grade and poor patient survival [20, 74, 83]. The signaling cascades triggered by c-Met include the PI3K/AKT, ERK/MAPK, NF-κB, Wnt/β-catenin, and STAT/JNK, among others. These and other cascades contribute to a complex phenotypic response to HGF, which also depend on the cell type and culture conditions. Nevertheless, common responses of tumor cells include increased anchorage-independent growth, motility, and proliferation. Moreover, epithelial tubulogenesis is also observed in some cell types [5, 110, 83]. Tumor cells secrete growth factors, including PDGF, TNFα, bFGF, and others (depending on tumor-type) that upregulate HGF production in CAFs [24, 74], thereby establishing a dynamic tumor-host signaling program.

An additional heterogeneity in tumors results from intratumoral lineage hierarchies, which are generally less robustly controlled and more heterogeneous than in normal tissues [94, 75]. Tumor lineage research has resulted in emergence of cancer stem cells (CSCs) as potential targets of new cancer therapeutics [49]. CSCs are currently regarded as a highly dynamic population, whose behavior is determined by both genetic and environmental factors, and may be, instead of a specific cell type amenable to therapeutic targeting, a phenotype that a large population of cancer cells can achieve in the appropriate environmental conditions [127, 59]. We will consider a mathematical model of tumor growth that incorporates multiple tumor cell species and CAF-induced HGF production to better understand how lineage dynamics and the microenvironment contribute to the tumor growth phenotype.

Moreover, in development and tissue regeneration post-injury, a large number of growth factors have been found to elicit a biphasic response from the tissue: at lower concentrations the growth factor exerts a mitogenic or cell size growth effect, and at higher concentrations this effect is abrogated and cells quiesce or differentiate [11, 93]. For example, a long list of endogenous and exogenous agents display a biphasic dose-response curve with respect to neurite outgrowth both *in vitro* and *in vivo*, including Nerve Growth Factor (NGF), Fibroblast Growth Factor (FGF), Vascular Endothelial Growth Factor (VEGF), and adrenocorticotropic hormone (ACTH) [12, 128]. Purported mechanisms for the biphasic dose response include presence of a high affinity and a low affinity receptor [42, 57, 122, 13], receptor internalization at high growth factor concentration [100], and/or concentration-dependent biphasic receptor response via activation of opposing pathways [123].

During skeletal muscle injury, dormant satellite myogenic stem cells are activated to enter the cell cycle by low concentrations of HGF, which is released from extracellular stores (as well as produced by spleen, liver, and the satellite cells themselves) after injury [95, 104]. But, at concentrations of greater than 10ng/ml, HGF inhibits satellite cell division [63, 108], and it was shown that this inhibition is due to increased myostatin (a TGFβ family member)

production at higher levels of HGF [123]. As with the growth factors involved in neurite outgrowth, while the mitogenic action of HGF is well understood, the molecular nature of the inhibitory effect of HGF at high concentrations has not yet been established. Yamada et al. provided two hypotheses: that differential activation of c-Met is the cause of proliferation arrest, as evidenced by requirement of phosphatase SHP2 for the arrest, which is recruited by actived c-Met, and/or the presence of as yet unidentified low affinity receptors for HGF [123, 63, 109]. In this thesis, we will also derive a mathematical model that may help to ascertain the molecular nature of HGF-induced growth arrest at high HGF concentration.

Mathematical models of tumor growth now compose several classes, including continuous, discrete, and hybrid; single compartment and multi-compartment (see [10], [68], [25], for comprehensive reviews of the aforementioned model types). Incorporation of the microenvironment into these models involves adding an extra layer of complexity to an underlying model structure. Angiogenesis, macrophage infiltration, stromal-mechanical perturbations, and chemical influences have all been modeled by one or more of the previous model classes [89, 70, 17, 27, 52, 2]. With respect to chemical influences, gradients of nutrients and metabolites have been shown to have an effect on tumor phenotype. For example, Anderson et al. used a hybrid discrete-continuum model to show that a heterogeneous ECM or nutrient-deprived microenvironment may select for a morphologically invasive tumor phenotype. Both microenvironments led to selection pressure on the tumor for more aggressive phenotypes [2]. Despite the prevalence of tumor and tumor-microenvironment models, based on our current knowledge, no tissue-level models of the CAF-tumor dynamic has been developed that specifically addresses the HGF/c-Met and tumor-derived growth-factor signaling pathway dynamics.

Thesis Outline

In this thesis, we address certain heterogeneities introduced by the tumor microenvironment using models of decreasing complexity. In Chapter 1, we derive a multiscale, multispecies spatiotemporal model of tumor growth with host-produced HGF and tumor-produced HGF-stimulating factors. We explore the effect of reduced negative growth feedback as well as targeted therapy on the growth phenotype at increasing levels of HGF responsiveness. We also investigate how HGF-induced cell motility can increase cell-species heterogeneity at the tumor-host boundary, thereby destabilizing tumor morphology.

In Chapter 2, we derive a simpler model, a homogeneous system of ODEs, to explore an experimental result associated with the tumor-HGF dynamic, namely that while application of lower concentration of HGF to colon cancer initiating cell (CCIC) tumor spheroids results in an (expected) increased growth rate, application of higher concentrations of HGF abrogates growth. Since the molecular method of HGF-induced growth retardation is unknown, the simplified mathematical model is used to explore how different hypotheses of HGF-action on a negative growth regulator can result in different dose-response curves of colon spheroid growth with respect to increasing HGF concentrations. The model thus allows us to derive a first hypothesis on how HGF can act as a negative growth regulator at higher concentrations.

Finally, in Chapter 3, we simplify the model even further to a system of two ordinary differential equations of stem cells, $S(t)$, and stem cell self-renewal activator molecules, $a(t)$. The system is simplified in order to gain an analytical understanding of under which circumstances therapy can eradicate a tumor, or the tumor can undergo spontaneous remission. We use the Stable Manifold Theorem to approximate the separatrix that divides system behavior between remission and sustained growth. This model sets the stage for more complex, but analytically tractable, models that can involve microenvironmental components (such as HGF) or more complex relationships between $S(t)$ and other parameters that can provide a

framework for prediction of the qualitative behavior of a tumor under therapy given known microenvironmental conditions.

The complementary strengths of each model allow for a multifaceted mathematical exploration of tumor development in a growth-promoting microenvironment.

Chapter 1

The HGF/c-Met axis in tumor growth: a multispecies model

Using, as a starting point, a spatiotemporal, multispecies model of tumor growth [126], we investigate how the development and spread of a tumor is impacted by a dynamic interaction between tumor-derived growth factors and CAF-derived HGF.

1.1 The Mathematical Model

1.1.1 Overview

By incorporating lineage dynamics of different tumor cell types, Youssefpour et al. have recently developed a multispecies continuum model of tumor growth [126]. In this paper, we elaborate on the model to incorporate tumor-CAF interactions. The tumor tissue is modeled to be composed of three cell types: stem, terminal, and dead. While many cell lineage models also include committed progenitor cells as an intermediate phenotype between stem

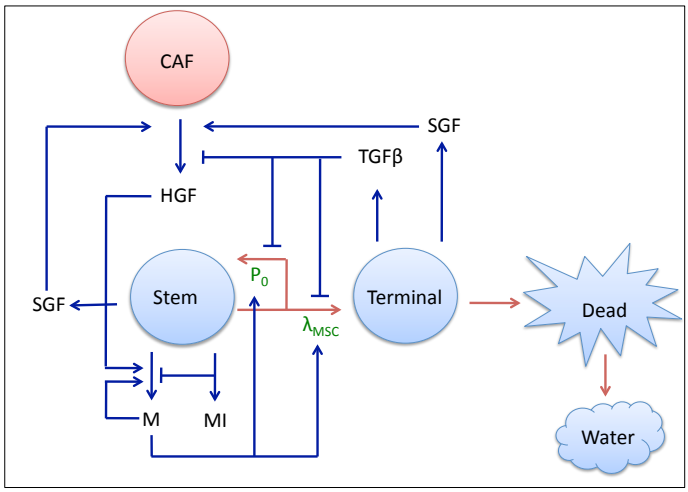

Figure 1.1: Tumor-CAF interaction model.
Tumor components (stem, terminal, and dead cells, and water) are in blue, host component (CAF) is in red, associated growth factors and proteins (M, MI, HGF, SGF, TGFβ, SGF) in black. Critical parameters in green. Red arrows represent tumor species interconversion, blue arrows represent chemical production and action. Stem cells renew with probability P_0, and divide with rate λ_{MSC}. Terminal cells die either apoptosis and dead cells are converted to water. P_0 is promoted by M and HGF, and lowered by TGFβ, which is produced by the differentiated cells. M production, in turn, is promoted by itself and HGF, and lowered by MI. HGF production is promoted by SGF, which are produced by stem and terminal cells.

and terminal cells, our model classifies both committed progenitor and cancer stem cells in the stem cell category. We do this in order to lower the parameter burden and to simplify the model. In future work, we will consider these two compartments separately.

Stem cells have a probability of self-renewal, P_0, and a division rate, λ_{MSC}, that are dependent upon negative feedback from TGFβ family members produced by terminal cells and positive feedback by products of the c-Met signaling cascade, M. Moreover, M are inhibited by stem-cell produced c-Met inhibitors, MI, allowing for a mechanism of pattern formation that is exhibited in Youssefpour et al. HGF is produced by CAFs at a low basal rate, and is stimulated by production of SGF by the stem and terminal cells. HGF, in turn, promotes production of M products. Terminal cells die via apoptosis or necrosis, and dead cells are eventually converted to water (Figure 2.1).

1.1.2 Cell species conservation, HGF-induced cell-spread, and cell velocity

Local volume fractions of the cell species ($\phi_{CSC,TC,DC}$), host (ϕ_H) and water (ϕ_W) make up the dependent variables, which sum to 1. Assuming that that the total solid and water fractions are constant allows us to determine the water component via solid component dynamics. A conservation equation of the form

$$\frac{\delta \phi_*}{\delta t} = \overbrace{-\nabla \cdot \mathbf{J}_*}^{\text{Generalized Diffusion}} + \overbrace{\text{Src}_*}^{\text{Reaction}} + \overbrace{-\nabla \cdot (\mathbf{u}_s \phi_*)}^{\text{Advection}} \tag{1.1}$$

is produced for each cell type, where $*$ denotes tumor cell species. A Helmholtz free energy of global adhesion is given by [119, 126]

$$E = \frac{\gamma}{\epsilon} \int_\Omega F(\phi_T) + (\epsilon)^2 |\nabla \phi_T|^2 dx, \tag{1.2}$$

where $\Omega = \phi_T + \phi_H$, $F(\phi_T)$ models energy from local adhesion, $\epsilon^2 |\nabla \phi_T|^2$ models longer range interactions, and γ is a global measure of cell-cell adhesion (incorporating both local and longer-range contributions to adhesion). Generalized diffusion is represented by $-\nabla \cdot \mathbf{J}$, where $\mathbf{J}_* = -\text{Mb}\phi_* \nabla \mu$. Here, Mb is mobility and μ is the chemical potential,

$$\mu = \frac{\delta E}{\delta \phi_T} = \frac{\gamma}{\epsilon} \left(\frac{dF}{d\phi_T}(\phi_T) - \epsilon^2 \nabla^2 \phi_T \right). \tag{1.3}$$

The effect of HGF on cell spread was one of the first physiological effects reported for this molecule, HGF was first termed scatter factor for its scattering effect on epithelial cells [103]. Since then, HGF has been shown to have a pro-migratory effect on cells in the contexts of development, wound healing, and cancer [5]. The pro-migratory effect is mediated by several pleiotropic effects of activated c-Met on cell physiology. The c-Met-activated Ras cascade has been shown to be critical for disassembly of adherens junctions

between tumor cells [88, 113]. Additionally, activated c-Met results in increased production of the proteolytic enzyme urokinase-type plasminogen activator (uPA) and its receptor (uPAR) [46, 82]. uPA catalyzes ECM degradation and remodeling, and is correlated with increased malignancy in several cancers [97, 26, 114]. In MDCK cells, HGF-activated c-Met was found to further promote cell dispersal by enhancing cell-ECM interaction via modification of cellular transmembrane integrin protein activity [111].

We model the effect of c-Met on cell spread by having it act on the local interaction energy: $F(\phi_T)$,

$$F(\phi_T) = \frac{\tilde{E}}{4}\left(\left(\left(\phi_T - \frac{1}{2}\right)^4 + \frac{1}{16}\right) - \frac{1}{2}\left(\phi_T - \frac{1}{2}\right)^2 g(C_M)\right), \tag{1.4}$$

$$g(C_M) = \frac{1}{1+\delta_1 C_M} \tag{1.5}$$

$$\tilde{E} = 1 + \frac{\delta_2 C_M}{1+\delta_2 C_M} \tag{1.6}$$

where $\tilde{E} > 0$ is an energy scale. When $g(C_M) = 1$, F is a double-well potential that is minimized in the tumor ($\phi_T = 1$) and host ($\phi_T = 0$). As $g(C_M)$ decreases, F tends towards a single-well potential at $\phi_T = 1/2$. By taking $g(C_M)$ as in (1.5), where δ_1 is the strength of c-Met effect on g, we can obtain a shift towards the single-well potential with increasing c-Met. This allows us to model the break-down of cell-cell adhesion and increase in cell-matrix adhesion promoted by c-Met. Additionally, by taking $\tilde{E}$ as in (1.6), where δ_2 indicates strength of c-Met action on $\tilde{E}$, we can model the local effect of c-Met on ECM remodeling, since an increased $\tilde{E}$ increases local energy of components independently of whether F is a single- or double-well potential. We take $\delta_{1,2} = 0.02$, as we have found that at these values, the effect of c-Met on cell spread in the absence of HGF is negligible, whereas at higher HGF dynamics (see below), c-Met effect on cell spread becomes physiologically significant.

The cell velocity, $\mathbf{u}_s$, is assumed to satisfy the generalized Darcy's law, which is a constitutive

equation that models fluid flow through a porous media, [119, 68],

$$\mathbf{u}_s = -\kappa(\nabla p - \frac{\gamma}{\epsilon}\mu\nabla\phi_T) \tag{1.7}$$

where κ reflects combined effects of cell-cell and cell-matrix adhesion, p is the solid pressure generated by cell proliferation, and $\mu\nabla\phi_T$ is the contribution from adhesion forces described above [119, 126]. We can sum the conservation equations to obtain an equation for velocity

$$\nabla \cdot \mathbf{u}_S = \mathrm{Src}_{CSC} + \mathrm{Src}_{TC} + \mathrm{Src}_{DC}, \tag{1.8}$$

with the assumption that the host is under homeostatic conditions ($\mathrm{Src}_H = 0$). The pressure p can be solved for using Equations (1.7) and (1.8).

At the boundary, Σ_∞ of the domain, Ω, we impose homogeneous Neumann boundary conditions: $\nabla\phi_{T,CSC,TC} = \omega_\infty = 0$, where ω_∞ is the outwards-pointing normal vector on Σ_∞. Chemical potential, μ, and pressure, p, have homogeneous Dirichlet conditions on Σ_∞, allowing the tumor to move across the outer boundary [119].

1.1.3 The mass-exchange equations

Src_* represents the mass-exchange terms, which incorporate mitosis, differentiation, death, and species conversion. The self-renewal rate of the CSCs is P_0, and both self-renewal and mitosis rates are proportional to concentration of oxygen and nutrients, represented by a single variable C_O. Cell death occurs by apoptosis (necrosis is considered as negligible). The

source terms are as follows:

$$\mathrm{Src}_{CSC} = \overbrace{\lambda_{\mathrm{MSC}}(2P_0 - 1)\phi_s C_O G(\phi_{CSC})}^{\text{Stem cell self-renewal}} \tag{1.9}$$

$$\mathrm{Src}_{TC} = \overbrace{2\lambda_{MSC}(1 - P_0)\phi_{CSC} C_O G(\phi_{CSC})}^{\text{Differentiation of CSCs}} + \overbrace{\lambda_{MTC}\phi_{TC} C_O G(\phi_{TC})}^{\text{Mitosis}} - \overbrace{\lambda_{ATC}\phi_{TC}}^{\text{Apoptosis}} \tag{1.10}$$

$$\mathrm{Src}_{DC} = \overbrace{\lambda_{ATC}\phi_{TC}}^{\text{Apoptosis}} - \overbrace{\lambda_L \phi_{DC}}^{\text{Lysis}} \tag{1.11}$$

where mitosis, apoptosis, necrosis, and lysis rates are denoted by λ_M, λ_{A*}, λ_{H*}, and λ_{L*}, respectively, where $*$ indicates cell type. Proliferation is cut off at sufficiently low concentration by $G(\phi_*)$, specifically, we take

$$G(\phi_*) = \begin{cases} 1 & \text{if } \phi_* > \frac{3}{2}\epsilon, \\ \phi_* - \frac{1}{2}\epsilon & \text{if } \frac{1}{2}\epsilon < \phi_* < \frac{3}{2}\epsilon, \\ 0 & \text{if } \phi_* < \frac{1}{2}\epsilon. \end{cases} \tag{1.12}$$

1.1.4 Stem cell self-renewal and division

HGF/c-Met induces cellular proliferation via multiple signaling cascades, including Ras/Raf, PI3K/Akt, NF-κB, and Wnt/β-catenin [5, 110, 83, 78, 64]. Moreover, HGF/c-Met has been implicated in CSC development and maintenance in colon cancer [116], glioblastoma [65, 48] and head and neck squamous cell carcinoma (HNSCC) [66]. For example, Vermeulen et al. showed that HGF-induced β-catenin nuclear localization and activation of canonical Wnt signal was associated with increased cellular clonogenicity in primary colon cancer spheroid cultures, implicating the cascade in promoting the CSC phenotype [116]. Similarly, Lim. et al have shown that in head an neck squamous cell carcinoma (HNSCC) HGF/c-Met promoted HNCSCC CSC marker expression and cell sphere-forming capacity. When c-Met was knocked down, the cells showed increased radiosensitivity and decreased ability to form tumors in a mouse xenograft model [66]. HGF has also been shown to have an effect on reducing apoptosis rates [121].

TGFβ is a potent growth inhibitor [44] and differentiation promoter [117] for many cell types and early-stage tumors. We model the effect of HGF and TGFβ on stem cell self-renewal and proliferation below. To lower the parameter burden, we maintain a low, and constant, apoptotic rate in the Src equations that is not dependent on the growth factors. We take

$$P_0 = P_{\min} + (P_{\max} - P_{\min}) \left(\frac{\xi_0 C_M}{1 + \xi_0 C_M} \right) \left(\frac{1}{1 + \psi_0 C_{TGF\beta}} \right), \tag{1.13}$$

$$\lambda_{MSC} = \lambda_{MSC_{min}} + (\lambda_{MSC_{max}} - \lambda_{MSC_{min}}) \left(\frac{\xi_1 C_M}{1 + \xi_1 C_M} \right) \left(\frac{1}{1 + \psi_1 C_{TGF\beta}} \right), \tag{1.14}$$

where $P_{min,max}$ and $\lambda_{MSC_{min,max}}$ are the minimum and maximum rates of self renewal and stem cell division rates, respectively. $\xi_{0,1}$ represent the strength of M effect on P_0 (ξ_0) and λ_{MSC} (ξ_1). $\psi_{0,1}$ represent the strength of inhibitory TGFβ action on P_0 (ψ_0) and λ_{MSC} (ψ_1).

1.1.5 Chemical Species

Oxygen / Nutrients

The combined effect of oxygen and nutrients is denoted as O. Uptake is assumed to be negligible in the host in comparison to the tumor species, and diffusion rapid [119, 126]. Hence, C_O can be modeled using a quasi-steady state equation:

$$0 = \nabla \cdot (D_O \nabla C_O) - (\nu_{UOCSC} \phi_{CSC} + \nu_{TC} \phi_{TC}) C_O + \nu_{PO} (\bar{C}_{AO} - C_O) \phi_H, \tag{1.15}$$

where ν_{UOSC}, ν_{UOTC} are the uptake rates by the CSCs and TCs, respectively, and D_O is the diffusion coefficient. Rate of O entering the microenvironment is modeled by ν_{PO}, and concentration of O in the medium sufficiently far from the tumor is given by $\bar{C}_{AO}$, which is also taken to be the boundary condition on Σ_∞, $C_O = \bar{C}_{AO}$.

TGFβ

A diffusible differentiation promoter, produced by differentiated cells, is modeled by the variable TGFβ, which represents the TGFβ superfamily [77, 67]. Although in later stages of cancer TGFβ may be produced by other cell types (namely stroma and immune), we do not model that here since this progression coincides with inactivation of certain TGFβ downstream signaling components and results in a phenotypically distinct role of TGFβ from its tumor-suppressing effects [72]. We model loss of responsiveness to TGFβ in Section 1.2.3 and discuss approaches to modeling the TGFβ 'paradox' (i.e. its tumor-promoting actions) in Section 1.3.

Rapid diffusion is assumed for TGFβ due to the long-range action of some of its family members, such as Activin [47], which is directly involved in regulating epithelial tumorigenesis [62]. Hence, we use a quasi-steady reaction-diffusion equation for $C_{TGF\beta}$,

$$0 = \nabla \cdot (D_{TGF\beta} \nabla C_{TGF\beta}) - (\nu_{UTGF\beta}\phi_{CSC} + \nu_{DTGF\beta}) C_{TGF\beta} + \nu_{PTGF\beta}\phi_{TC}, \tag{1.16}$$

where $\nu_{UTGF\beta}$ is the uptake rate by CSCs, $\nu_{DTGF\beta}$ is the decay rate, $\nu_{PTGF\beta}$ is the production rate by TCs, and $D_{TGF\beta}$ is the TGFβ diffusion coefficient. The boundary condition for $C_{TGF\beta}$ is taken to be Dirichlet ($C_{TGF\beta} = 0$) on Σ_∞.

c-Met and c-Met inhibitors

A generalized Geirer-Meinhard-Turing system is used to model c-Met products, M, as the activator and their inhibitors MI [112, 29]. Such a system, with Wnt/Dkk as the activator/inhibitor has been suggested in hair follicle development [96], and crypt generation [129]. The large number of cross-activating downstream signaling components of c-Met, some of which include positive feedback loops amongst themselves [115, 105], motivate a nonlinear M activation term. Inhibitors of c-Met and its downstream effectors activated by induced c-Met include the autocrine-acting c-CBL [85], paracrine-acting Delta [101], and the secreted factor Dkk. Since c-Met products are autocrine or paracrine effectors, we take M products to have a short-range and MI a long-range diffusion

coefficient. The functional correlation between cancer stem cells and enhanced c-Met activity has been discussed in 2.4, hence we model M and MI production to be limited primarily to CSCs. We also include low-level background production of M by all viable tumor cell types. Since HGF activates M products and induces c-Met production, we model the effect of HGF on M by its positive effect on the production rate of M, ν_{PM}. Finally, production is made dependent on nutrient (O) levels (in this model, we do not consider hypoxia-dependent c-Met upregulation [110]). We take

$$\frac{\partial C_M}{\partial t} + \nabla \cdot (\mathbf{u}_s C_M) = \nabla \cdot (D_M \nabla C_M) + f(C_M, C_{MI}), \tag{1.17}$$

$$\frac{\partial C_{MI}}{\partial t} + \nabla \cdot (\mathbf{u}_s C_{MI}) = \nabla \cdot (D_{MI} \nabla C_{MI}) + g(C_M, C_{MI}), \tag{1.18}$$

$$f(C_M, C_{MI}) = \nu_{PM} \frac{C_M^2}{C_{MI}} C_O \phi_{CSC} - \nu_{DW} C_M + \eta_M C_O (\phi_{CSC} + \phi_{TC}), \tag{1.19}$$

$$\nu_{PM} = \nu_0 + \lambda_{HGF} C_{HGF}, \tag{1.20}$$

$$g(C_M, C_{MI}) = \nu_{PMI} C_M^2 C_O \phi_{CSC} - \nu_{DMI} C_{MI}, \tag{1.21}$$

where D_M is the diffusion coefficient for downstream M effectors, which is assumed to be small. λ_{HGF} represents the strength of positive feedback of HGF on M. η_M represents background production of M signal promoters, ν_{PM}, ν_{DM} are the respective production and decay rates of M-activated genes and ν_{PMI}, ν_{DMI} are the respective production and decay rates of M inhibitor proteins. ν_{PM} is a sum of ν_0, the auto-activation rate of M, and $\lambda_{HGF} C_{HGF}$, the HGF-dependent activation rate of M. The boundary conditions for M and MI chemical fields are assumed to be homogeneous Neumann, $\omega_\infty \cdot \nabla C_W = \omega_\infty \cdot \nabla C_{MI} = 0$ on Σ_∞.

HGF and stromal-acting growth factors (SGF)

Cancer cells secrete growth factors and cytokines such as TNFα, bFGF, and PDGF, which cause upregulation of HGF production in stromal cells [30, 92, 24, 74]. We cannot currently specify whether the stem cells preferentially release these growth factors and if increased M signal results in an increased release of these factors from neighboring tumor cells, which would indicate a positive

feedback mechanism. With the data available, we model a positive effect of growth factors from viable tumor tissue on HGF production in the stroma.

Additionally, there is substantial evidence that TGFβ is a negative regulator of HGF production in stromal cells, and thus we include its inhibitory effect in the model [31, 41, 74]. We take

$$\frac{\partial C_{HGF}}{\partial t} = \nu_{PHGF}\frac{C_{SGF}}{\zeta + C_{TGF\beta}}C_O\phi_H + \eta_0 C_O\phi_H - \nu_{DHGF}C_{HGF} + \nabla\cdot(D_{HGF}\nabla C_{HGF}).,\ (1.22)$$

$$\frac{\partial C_{SGF}}{\partial t} = C_O(\nu_{SGFS}\phi_{CSC} + \nu_{SGFT}\phi_{TC}) - \nu_{DSGF}C_{GF} + \nabla\cdot(D_{SGF}\nabla C_{SGF}),\ (1.23)$$

where ν_{PHGF} and ν_{DHGF} are the production and decay rates, respectively, of HGF. C_{SGF} represents the concentration of HGF-promoting factors and $C_{\mathrm{TGF}\beta}$ represents the concentration of HGF-inhibiting factors from the TGFβ superfamily. ζ is a value close to zero, and added to regularize the equation while D_{HGF} is the diffusion coefficient for HGF. D_{HGF} is taken to be lower than the diffusion coefficients for the other growth factors due to its high molecular weight [81]. ν_{SGFS} and ν_{SGFT} represent respective production rates of the stem cell fraction, and the differentiated cell fraction. ν_{DSGF} is the decay rate for the growth factors and D_{SGF} is the diffusion rate of the growth factors. For the primary results, we let $\nu_{SGFS} = \nu_{SGFT}$, and test the case for asymmetrical SGF production in Appendix B.

1.1.6 Nondimensionalized Equations

The equations are nondimensionalized as in [119, 126]: we take the O diffusion scale, $l = \sqrt{D_O/\nu_{UOSC}}$, and the mitosis time scale $\tau = (\lambda_{MSC_M}\bar{C}_{AO})^{-1}$, where λ_{MSC_M} represents the midpoint of $\lambda_{MSC_{min}}$ and $\lambda_{MSC_{max}}$. The diffusion length scale, l, is estimated to be $l \approx 150\mu m$ and the mitosis time scale to be $\tau \approx 1$ following [28]. The nondimensionalization procedure is described in Appendix A, and the nondimensionalized equations are as follows. Taking $*$ to be CSC, TC, or DC, the equations for the volume fractions are

$$\frac{\partial \phi_*}{\partial t} = Mb\nabla\cdot(\phi_*\nabla\mu) + \mathrm{Src}_* - \nabla\cdot(\mathbf{u}_S\phi_*),\ (1.24)$$

with the chemical potential as $\mu = (\partial F/\partial \phi_T)(\phi_T) - \epsilon^2 \nabla^2 \phi_T$ and velocity

$$\mathbf{u}_S = -\kappa \left(\nabla p - \frac{\gamma}{\epsilon} \mu \nabla \phi_T \right). \tag{1.25}$$

Pressure can be solved for using (1.25) and

$$\nabla \cdot \mathbf{u}_S = \mathrm{Src}_{CSC} + \mathrm{Src}_{TC} + \mathrm{Src}_{Dc}. \tag{1.26}$$

The source terms are

$$\mathrm{Src}_{CSC} = \lambda_{MSC}(2P_0 - 1)\phi_{CSC} C_O G(\phi_{CSC}), \tag{1.27}$$

$$\mathrm{Src}_{TC} = 2\lambda_{MSC}(1 - P_0)\phi_{CSC} C_0 G(\phi_{CSC}) + \lambda_{MTC}\phi_{TC} C_O G(\phi_{TC}) - \lambda_{ATC}\phi_{TC}, \tag{1.28}$$

$$\mathrm{Src}_{DC} = \lambda_{ATC}\phi_L \phi_{DC}, \tag{1.29}$$

where the P_0, the self-renewal fraction and λ_{MSC}, the stem-cell division rate are

$$P_0 = P_{\min} + (P_{\max} - P_{\min}) \left(\frac{\xi_0 C_M}{1 + \xi_0 C_M} \right) \left(\frac{1}{1 + \psi_0 C_{TGF\beta}} \right),$$
$$\lambda_{MSC} = \lambda_{MSC_{min}} + (\lambda_{MSC_{max}} - \lambda_{MSC_{min}}) \left(\frac{\xi_1 C_M}{1 + \xi_1 C_M} \right) \left(\frac{1}{1 + \psi_1 C_{TGF\beta}} \right).$$

The equations for O and TGFβ, respectively, are

$$0 = \nabla^2 C_O - C_O(\phi_{CSC} + \nu_{UOTC}\phi_{TC}) + \nu_{PO}(1 - C_O)\phi_H, \tag{1.30}$$

$$0 = \nabla^2 C_{\mathrm{TGF}\beta} - (\nu_{UT}\phi_{CSC} + \nu_{DT}) C_{\mathrm{TGF}\beta} + \nu_{P\mathrm{TGF}\beta}\phi_{TC}. \tag{1.31}$$

The equations for M and MI are

$$\frac{\partial C_M}{\partial t} = \nabla \cdot (D_M \nabla C_M) + Rf(C_M, C_{MI}), \tag{1.32}$$

$$\frac{\partial C_{MI}}{\partial t} = \nabla \cdot (D_{MI} \nabla C_{MI}) + Rg(C_M, C_{MI}), \tag{1.33}$$

$$f(C_W, C_{MI}) = (\nu_0 + \lambda_{HGF} C_{HGF}) \frac{C_M^2}{C_{MI}} C_O \phi_{CSC} - C_M + \eta_M C_O (\phi_{CSC} + \phi_{TC}), \tag{1.34}$$

$$g(C_M, C_{MI}) = C_M^2 C_O \phi_{CSC} - \nu_{DMI} C_{MI}. \tag{1.35}$$

We note that we neglect the advection terms in (1.17) and (1.18) following [126]. The equations for HGF and SGF are

$$\frac{\partial C_{HGF}}{\partial t} = \nu_{_{PHGF}} \frac{C_{SGF}}{\zeta + C_{TGF\beta}} C_o \phi_H - \nu_{DHGF} C_{HGF} + \nabla \cdot (D_{HGF} \nabla C_{HGF}), \tag{1.36}$$

$$\frac{\partial C_{SGF}}{\partial t} = C_O (\nu_{_{SGFS}} \phi_{CSC} + \nu_{_{SGFT}} \phi_{TC}) - \nu_{_{DSGF}} C_{GF} + \nabla \cdot (D_{SGF} \nabla C_{SGF}). \tag{1.37}$$

1.1.7 Parametrization

The model was parametrized as follows. Parameters that overlap with the Youssef. et al model were maintained. Parameters novel to the model were selected based on background literature and preliminary simulations. Choice of specific parameter values are described alongside model presentation, and summarized in Appendix A.1.

1.2 Results

An adaptive finite difference-nonlinear multigrid method [119, 118, 126] is used to solve the governing equations efficiently on a computational domain of $[-20, 20]^2$. We solve for $\phi_T = \phi_{CSC} + \phi_{TC} + \phi_{DC}$, then we can calculate $\phi_{TC} = \phi_T - (\phi_{CSC} + \phi_{DC})$ and $\phi_H = 1 - \phi_T$. To remove a high-order time step constraint incurred by an explicit method, we use an implicit 2nd order accurate time discretization of Crank-Nicholson type, and spatial derivatives are discretized using 2nd order ac-

curate central difference approximations. In regions of large gradients, block structured Cartesian refinement is used to provide enhanced local resolution. For further details, see [126].

We initialize the tumor with an asymmetrical shape and a 45/50/5 homogenous fractional distribution of SCs, TCs, and DCs (respectively). We note that changing the initial fractional distribution of cell compartments does not have a qualitative effect on resultant simulations. The initialized asymmetrical shape can be visualized in Figure 1.5 (a), and is created as follows

$$\phi_T(x,0) = \frac{1}{2}\left(1 - \tan h \frac{I(x,y)-1)}{2\sqrt{2}\epsilon}\right), \tag{1.38}$$

$$I(x,y) = \frac{\sqrt{3} + r(x,y)}{\sqrt{x^2+y^2}+0.001}, \tag{1.39}$$

where $r(x,y) = \sum_{i=1}^{2} a_i \cos(b_i\theta(x,y)) + \sum_{i=3}^{4} a_i \sin(b_i\theta(x,y))$, $\theta(x,y) = \tan^{-1}(y/x)$, $a_i \in (0,1)$, $b_i \in \mathbb{N}$ give the initial shape asymmetry. For specific values of $\{a_i, b_i\}$, we take $(a_1,a_2,a_3,a_4) = (0.2,0.1,0.1,0.1)$ and $(b_1,b_2,b_3,b_4) = (2,5,8,3)$. We then take $\phi_{CSC}(x,0) = 0.45 \cdot \phi_T(x,0)$, $\phi_{DC}(x,0) = 0.05 \cdot \phi_T(x,0)$, and $\phi_{TC}(x,0)$ can be solved for from the previous two equalities to obtain $\phi_{TC}(x,0) = 0.5 \cdot \phi_T(x,0)$. This initial condition allows for a diffuse interface representation of an asymmetrical tumor centered at the origin with maximum radius of $\sqrt{3}$.

Since parameters in the equations for C_W, C_{HGF}, and C_{SGF} are changed for varying HGF dynamics, we do not initialize a steady-state values as in [126], or we would have different initial conditions for different simulations. Instead, we take initial conditions for C_M and C_{MI} as identical to those for C_W and C_{WI} in [126] in order to maintain continuity with the former model in the sense that we want the control condition to be qualitatively similar to the model presented in [126]. Hence, we take $C_M(x,0) = (1.2 + 0.1(rand - 0.5))\phi_T$ and $C_{MI}(x,0) = 1.44\phi_T$, where *rand* is a random number uniformly distributed over $[0,1]$ and different at every point in the computational domain (the *rand* value used for each simulation remains the same for comparison purposes). The initial concentrations for C_{HGF} and C_{SGF} are taken to be $C_{HGF} = (1.0 + 0.1(rand - 0.5))\phi_H$ and $C_{SGF} = (1.0 + 0.1(rand - 0.5))\phi_T$. We note that other initial conditions for M, MI, HGF, and SGF produce qualitatively similar results. Since and C_O and $C_{\mathrm{TGF}\beta}$ satisfy quasi-steady diffusion equations, we need not take initial conditions for these fields.

1.2.1 Tumor progression with varying HGF feedback

We begin by simulating HGF dynamics in a tumor in its early stages, when response to inhibitory growth feedback is relatively strong. We do this by setting the TGFβ self-renewal feedback parameter, ψ_0, to $\psi_0 = 1$. In [126], the authors showed that a growing tumor with no HGF feedback grows slower and is more stable than a tumor with $\psi_0 = 0.5$. In the next section, we will show how HGF feedback alters tumor behavior with lowered response to TGFβ.

Since the strength of the dynamic relationship between HGF and SGF feedback is unknown, we simulate growth of the tumor in four distinct conditions: none, low, intermediate (int), and high HGF feedback. To change the strength of feedback, we focus on three parameters found in equations (1.36) and (1.37), ν_{PHGF}, ν_{SGFS}, and ν_{SGFT}. The strength of C_{SGF} action on C_{HGF} is represented by ν_{PHGF}, and $\nu_{SGFS,T}$ are the respective production rates of C_{SGF} by the stem and terminal tissue fractions. For low (respectively, int, high) HGF, we set $\nu_{PHGF} = \nu_{SGFS} = \nu_{SGFT} = 5$ (respectively $10, 15$). In Figure 1.2 the resulting simulations for the stem cell fraction for T = 50, 100, and 150 are shown. The outline of the tumor body is clearly visible in all simulations, and is highlighted in green for the no HGF, T = 50 case. We see that at low HGF, the number of spots increases in comparison to no HGF, and there is a minor change to more asymmetrical morphology. As HGF dynamics increase to int and high modes, the number of stem cell spots decreases, but the spot size increases, and there is a large change in morphology with increase in invasive fingering and tumor fragmentation in the T = 150, high HGF case.

We fix T = 100 in order to more closely observe other variables associated with the simulations, namely concentrations of c-Met, HGF, and SGF (Figure 1.3(a)) and total tumor, terminal cell, and dead cell fractions (Figure 1.3 (b)). In Figure 1.3(a), we observe that c-Met levels in the spots increase with increasing HGF dynamics, along with increased HGF concentration at the tumor-host boundary and SGF concentration within the tumor. In Figure 1.3(b), we see that a large fraction of all the cases contain terminal cells, with a smaller co-localized percentage of dead cells, and with both cell types concentrated outside of the areas with stem cell spots.

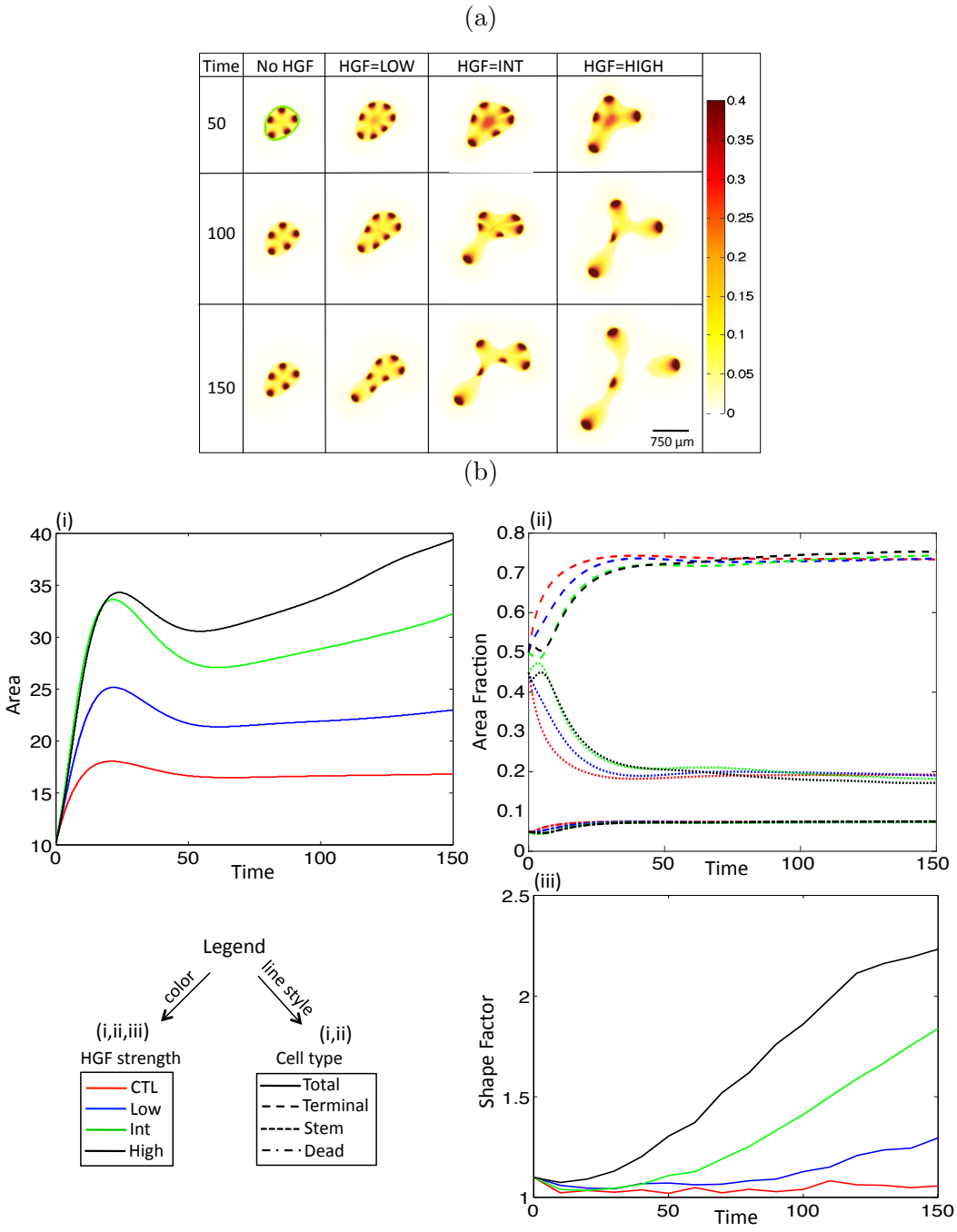

Figure 1.2: Simulation results for baseline parameters.
(a) Stem cell fractions for increasing HGF dynamics and T = 50, 100, 150. (b) Area, Area Fraction, and Shape Factor. (i) Total area and (ii) area fraction for Control (red), Low HGF (blue), Int HGF (green) and High HGF (black). Area fraction is shown for different cell types: differentiated, dash; stem: dot; dead: dash-dot). (iii) Shape factor results for the four treatment types.

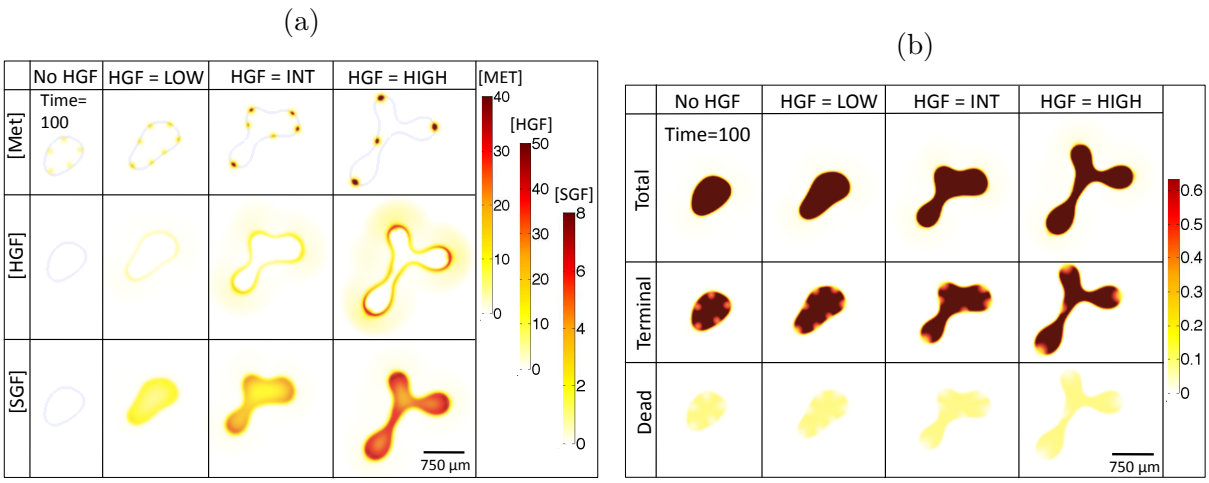

Figure 1.3: Chemical species (a) and cell species (b) concentrations with baseline parameters at T = 100.

In Figure 1.2 (b) (i,ii) we observe that the increase in total area for tumors with higher HGF dynamics is mainly due to increases in terminal cell concentration. Yet, in Figure 1.2 (b) (ii), we see that the different cell fractions remain similar over all the simulations. Indeed, it has been observed that cancer stem cells constitute a stable fraction of the tumor population [23]. In order to measure the changes in morphology induced by HGF dynamics, we consider the shape factor, f_{sf}, for an object, which is calculated by $f_{sf} = P^2/(4\pi A)$, where P and A are the perimeter and area, respectively, of an object. The shape factor for a circle is 1, and increases as the shape of the object becomes more asymmetrical or increases in branch count. In Figure 1.2 (b) (iii), we see that shape factor tends to increase over time in all cases, but increases more drastically as HGF dynamics increase, supporting the experimental results that HGF can induce branching and invasive morphology in exposed tissues and tumors, respectively [9, 45, 120]. We also see, in Figure 1.4 (a), that the increase in scatter with increasing HGF dynamics is primarily due to stem cell scatter. We quantify stem cell scatter by considering the stem scatter fraction (SSF): the area of stem cells in the host region normalized to the area of stem cells in the entire domain Ω. The initial non-zero fraction observed in Figure 1.4 (b) is due to the initialized diffuse interface of the tumor and host tissue. The the drop in SSF occurs during pattern formation, which decreases the stem cell pool and concentrates it in regions of high M. The latter increase in SSF is straightforward for the HGF high, low, and control conditions. With SSF highest in the HGF high condition over time,

followed by low HGF and control. The int HGF condition overtakes the high HGF at later time points due to the following phenomenon: while the effect on scatter is stronger in the high HGF condition due to higher M, stem cells are concentrated in fewer spots in the high HGF simulation than the int HGF simulation. Therefore, a larger surface area of stem cell area is exposed to the tumor-host boundary in the int HGF condition and can leave the tumor to form the host stem cell population. This result shows that while branching instability is higher in the high HGF case, with lower number of spots and greater heterogeneity at the tumor host boundary, as measured by the shape factor (Figure 1.2 (b) (iii)), the larger number of spots in the int HGF condition can destabilize the tumor via migration and scatter of the stem cell population.

1.2.2 Cell Scatter and Pattern Formation

In order to better understand how HGF dynamics influence spot formation, we examine the early and late-time dynamics of the simulations with and without c-Met-induced scatter (the latter case is simulated by setting $\delta_{1,2} = 0$ in (1.5) and (1.6)). In the early time ($0 \leq T \leq 50$), we notice that as HGF dynamics increase in simulations without scatter, spot size and number increases. With scatter, we still see an increase in spot size, but spots disappear due to early scatter of cells from high-stem regions, resulting in a lower number of spots than the simulations without scatter (Figure S2). Fixing HGF dynamics at high, we observe spot disappearance at very early time due to scatter (Figure 1.5 (a)). Comparing later time dynamics with and without scatter shows that loss of a stem cell spot in early time leads to more unstable dynamics over time, as evidenced by increase in shape factor for the $\delta_{1,2} = 0.02$ condition (Figure 1.5 (d)). Therefore, we see that scatter can have a destabilizing effect on the tumor morphology by increasing heterogeneity at the tumor-host boundary. We note that, as with the int and high HGF cases with baseline parameters, while the SSF is higher for $\delta_{1,2} = 0.02$, the SSF for $\delta_{1,2} = 0$ begins to approach the simulation with c-Met-induced scatter over time. This occurs due to the higher spot number in the $\delta_{1,2} = 0$ case, which increases the tumor stem cell fraction exposed to the tumor-host boundary. Thus, we see that increased scatter in areas with high M leads to greater morphological instability, but may reduce the overall load of migrating cells due to decreased physical exposure of the stem cell

fraction to the host.

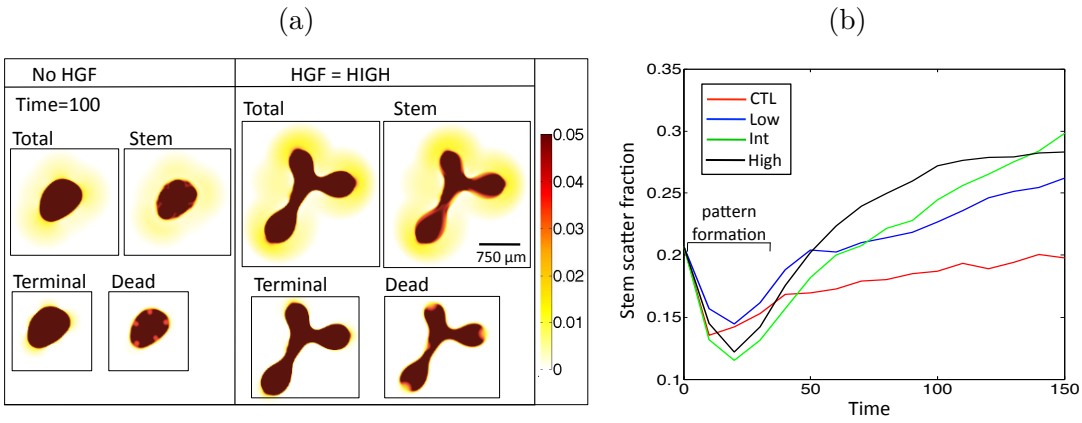

Figure 1.4: Cell dispersal with baseline parameters.
(a) Visualizing cell dispersal in no HGF and high HGF conditions for the different cell species. (b) Quantification of stem cell dispersal by the 'stem scatter fraction' (SSF) over time for increasing HGF dynamics.

1.2.3 Effect of negative feedback on tumor growth

A common characteristic of tumors that progress from pre-neoplastic lesions to neoplasms is that they lose ability to response to negative growth feedback [37]. Indeed, in colorectal cancer, resistance to TGFβ by mutation of a cognate receptor is associated with progression from adenoma to malignant carcinoma [33]. The TGFβ pathway can also be inactivated by mutation of TGFβR2 or inactivation of the downstream signaling components SMAD2, SMAD3, or SMAD4 [71].

Loss of response to members of the TGFβ family is correlated with poorer prognosis in a clinical setting [86]. Therefore, to model effect of HGF dynamics in a tumor that has progressed beyond the initial stages, we reduce the strength of TGFβ feedback on stem cell self-renewal from $\psi_0 = 1.0$ to $\psi_0 = 0.5$. When compared to the the case with $\psi_0 = 1.0$, the simulation results with reduced response to negative feedback have a greater area and shape factor, indicating the enhanced invasive potential of such tumors (Figure 1.6).

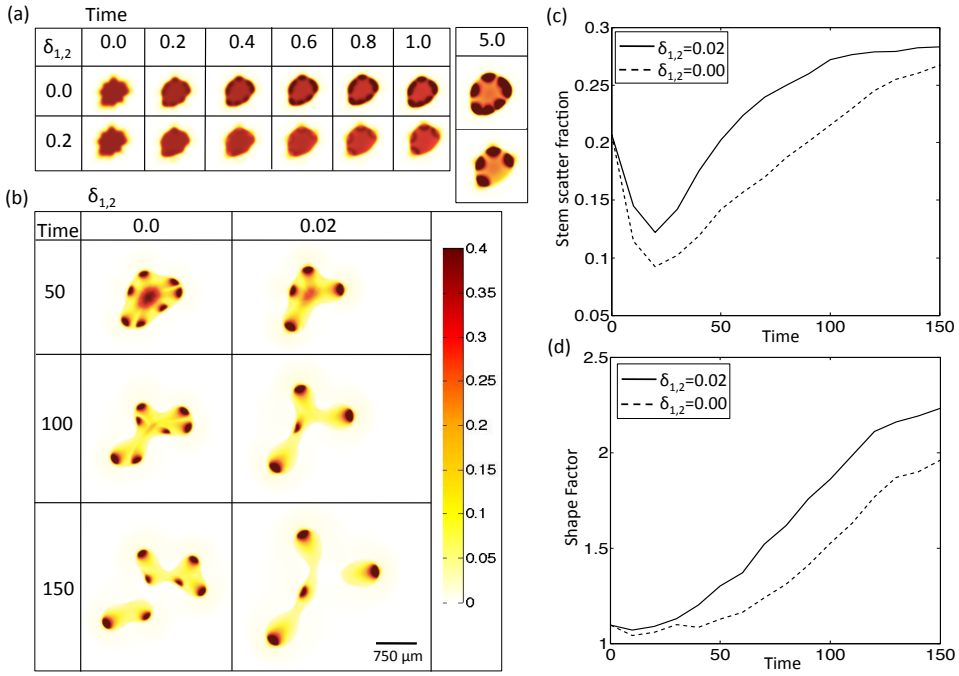

Figure 1.5: Comparison of baseline simulation with no c-Met effect on cell dispersal. Stem cell fraction in (a) very early time and (b) longer time and (c) stem scatter fraction (SSF) and (d) shape factor for high HGF condition with ($\delta_{1,2} = 0.02$) and without ($\delta_{1,2} = 0.0$) c-MET-induced cell scatter.

1.2.4 Therapy

Therapies targeting various aspects of the HGF/c-Met axis, including antibodies against HGF and c-Met, HGF-competitive analogs, tyrosine kinase inhibitors (TKIs) targeting c-Met, and downstream pathway inhibitors are currently in development [54, 7]. Over 20 drugs are currently in clinical Phase I-III clinical trials [16], indicating strong interest by the biomedical community in translating the accumulated knowledge of the HGF/c-Met axis into cancer therapeutics. We model targeted therapy by changing two parameters of the model which compromise ν_{PM}: λ_{HGF} and ν_0, found in Equation 1.20. While ν_0 represents the strength of c-Met auto-activation without HGF, λ_{HGF} represents the strength of HGF-induced c-Met activation. Lowering λ_{HGF} models drugs that act by inhibiting HGF, while lowering ν_{PM} represents drugs that specifically disrupt c-Met auto-catalysis. Drugs that inhibit c-Met or its downstream effectors lower both auto-catalysis rates and the ability of HGF to upregulate c-Met products. Therefore, activity of such drugs should

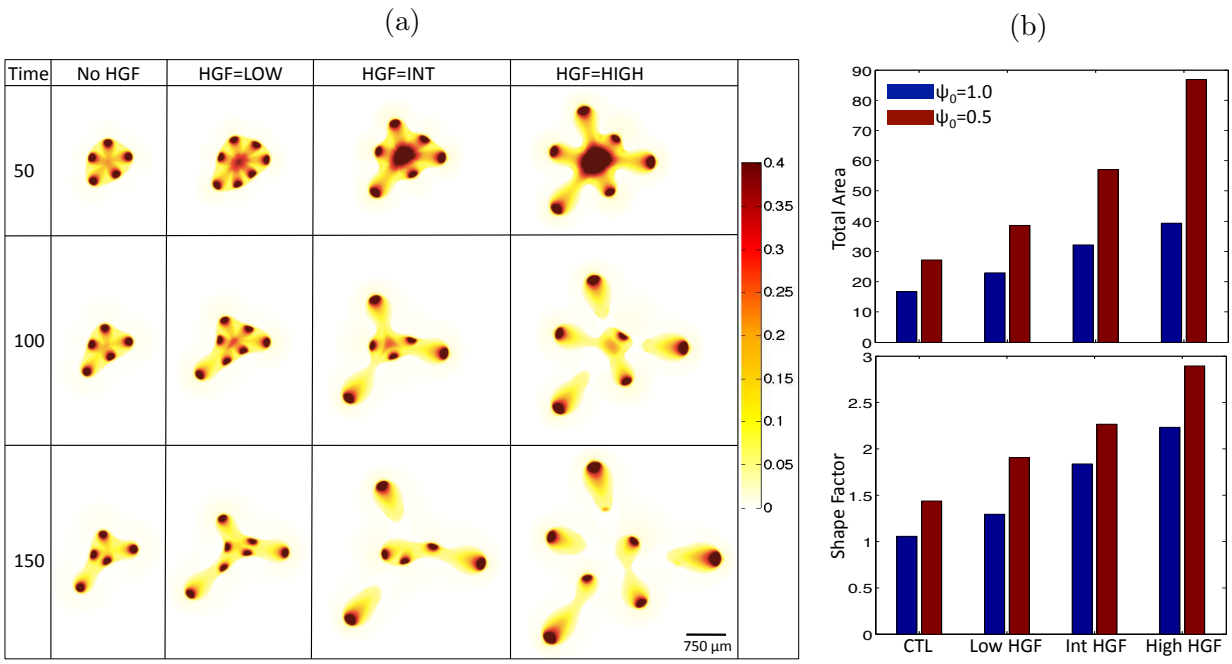

Figure 1.6: Response of tumor to decreased negative feedback ($\psi = 0.5$).
(a) Stem cell fractions for increasing HGF dynamics. (b) Difference of total area (top panel) and shape factor (bottom panel) between $\psi = 1$ (blue) and $\psi = 0.5$ (red) simulations at T = 150.

be modeled by lowering both parameters. We model two therapies applied at T = 50: T1 lowers λ_{HGF} from 0.5 to 0.05, and T2 lowers λ_{HGF} to 0.005 and ν_0 from 0.1 to 0.001. We choose these two therapies as they represent two different classes of therapy results that we observed when both parameters were systematically lowered for high HGF (Figure B.3). Therapy is applied until the last time point, T = 150. We find that when therapy is terminated prematurely, the tumor grows back rapidly (Figure B.4), indicating that ultimate tumor eradication requires combination therapy and/or surgical resection alongside anti-HGF/c-Met drugs. The first class, represented by T1, when c-Met levels are lowered above the threshold, results in decreased total area, but maintenance of invasive morphology, as evidenced by maintenance of a relatively high shape factor. The second class, represented by T2, results in even further decreases in total area, as well as a much less invasive morphology (Figure 1.7). It has been shown that very strong inhibition of c-Met phosphorylation ($> 90\%$) is required for significant inhibition of tumor growth ($> 50\%$) in a tumor xenograft mouse model [125], which is consistent with our simulation results.

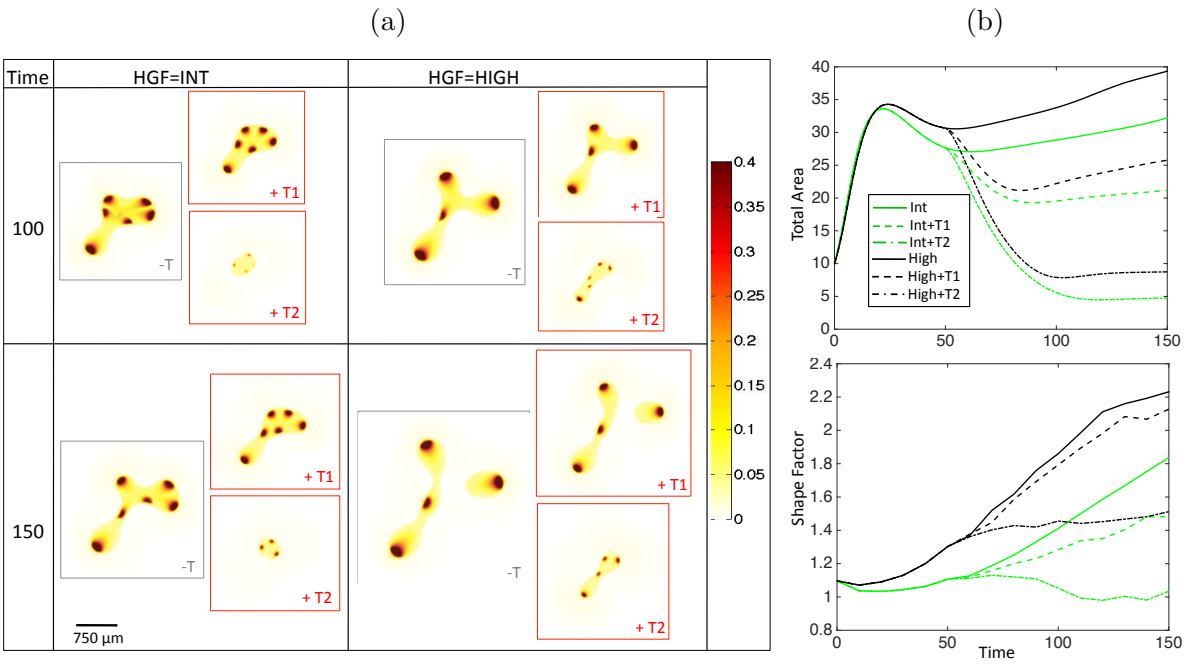

Figure 1.7: Application of therapy to disrupt the HGF/c-Met axis.
Response of tumor to anti-HGF (T1, λ_{HGF} lowered from 0.5 to 0.05) and anti-c-Met (T2, λ_{HGF} lowered from 0.5 to 0.05 and ν_{PM} lowered from 1 to 0.01) therapy applied at T = 50. (a) Representative stem cell fraction and (b) total area and shape factor for no therapy, T1, and T2 applied to Int and High HGF tumors.

1.3 Discussion

By incorporating tumor-produced SGF and the HGF/c-Met axis into a multispecies model of tumor growth, we have shown that establishment of this dynamic interaction between the tumor and its microenvironment results in increased tumor growth and morphological instability, the latter due in part to increased cell-species heterogeneity at the tumor-host boundary. Indeed, such a phenomenon has been investigated by Cristini et al [22]. Using both experimental and simulations, Cristini et al. showed that spatially heterogeneous cell proliferation, alongside disruption of cell-cell adhesion, results in invasive fingering and migration of cell clusters. In their model, the heterogeneity occurred due to heterogeneous distribution of oxygen, nutrients, and pH levels caused by atypical tumor vasculature and other disruptions to diffusion in the tumor. In our model, the heterogeneity occurs due to formation of stem cell spots at the tumor-host boundary via a Turing mechanism of c-Met and c-Met inhibitors. This heterogeneity is exacerbated by the presence of an HGF-SGF dynamic

since the effect of HGF on cell dispersal causes loss of some spots, and the effect of HGF on proliferation/self-renewal increases the size of the remaining spots. Indeed, when effect of HGF on cell dispersal is removed from the model, the tumor becomes more stable due to a more uniform distribution of stem cell spots at the tumor-host boundary, even though there are more of them than in the original model (Figure 1.5). Cristini et al. propose that suppression of morphologic instability via homogenization of cell proliferation and increase in cell-cell adhesion will result in a more compact, noninvasive tumor morphology. Our therapy results support their conclusions: when we block the HGF/c-Met axis sufficiently enough to reduce the highly proliferative spot size, the tumor does not only grow more slowly, but it grows in a more compact manner (Figure 1.7).

We find that invasive behavior is further increased if the tumor lowers responsiveness to tumor-derived pro-differentiation signals, which is a traditional hallmark of neoplastic development [37]. We have not addressed a portion of the pleiotropic effects of TGFβ that constitute the 'TGFβ paradox'. Namely, our model does not consider that in certain cases, TGFβ can increase cellular motility, as well as hasten the Epithelial-to-Mesenchymal Transition (EMT) of tumorigenic epithelial cells [86]. Moreover, it has been found that in advanced cancers, immune components and fibroblasts can produce TGFβ, which has tumor-promoting effects [72]. In this study, we only model the anti-proliferative effects of TGFβ, with its production localized to terminal cells. Incorporation of the tumor-promoting action of TGFβ may be best done using a specific cancer model and data, since such effects show greater diversity among different cancers than the other growth factors modeled in this paper.

By modeling anti-HGF and anti-c-Met therapy, we show how disruption of the HGF/c-Met cascade can lower tumor invasiveness and growth, thereby providing theoretical evidence that targeting tumor-microenvironment dynamics is a promising avenue for therapeutic development. An important consideration in clinical development of anti-HGF/c-Met therapies is patient selection and stratification. Indeed, studies on efficacy of HGF/c-Met targeted therapies have consistently shown that patients with high c-Met expression levels respond best to these therapies [34], indicating that patient pre-selection based on tumor biomarkers of HGF/c-Met axis activation can improve therapy outcomes [7]. As our model assumes c-Met as a main driver in stem cell self-renewal and division

rate, it is most directly applicable to patients with high c-Met activity.

Chapter 2

Modeling mechanisms of biphasic growth factor action on tumor growth

2.1 Introduction

We have recently found that culture of tumor spheroids derived from Colon Cancer Initiating Cells (CCICs), a primary colon cancer cell line [91, 98], in presence of increasing concentrations of HGF, has a biphasic effect on tumor growth [55]. Based on the research from Yamada et al., as well as findings that addition of HGF at a concentration of 40ng/ml induces expression of several members of the TGFβ family in an *in vitro* liver organoid culture [76], we have developed a simple model of biphasic HGF action on tumor growth where HGF stimulates canonical Wnt signal at low concentrations and TGFβ signal at higher doses. We focus in this chapter on HGF action on Wnt signal rather than all c-Met downstream effectors since colon cancer has a high incidence of Wnt-activating mutations that are modulated by HGF [116]. We show that the shape of the resulting dose-response curve of the model is dependent on the assumption of linearity (or non-linearity) of the effect of HGF on TGFβ production, hence demonstrating that the shape of the dose-response curve can give insight into the molecular nature of the biphasic response.

2.2 Mathematical Model

The mathematical model is specific to our experimental system, namely of HGF action on tumor cells, in order to optimize parametrization. Nevertheless, the model is simple enough that it can represent a more general system of a growth factor action on a tissue in a non-monotonic fashion. In this study, we develop a single-scale, spatially homogeneous model of HGF action on a multi-species tumor which consists of a coupled system of nonlinear ordinary differential equations representing changes in stem and terminal cell tumor species, as well as positive regulators (W) and negative regulators of tumor growth (T), as summarized in Figure 2.1 and discussed in the remainder of the section.

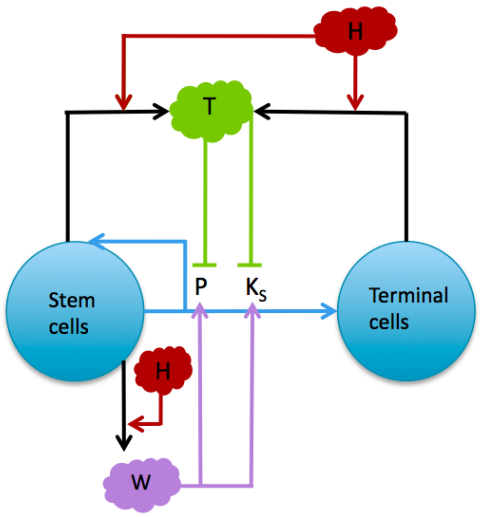

Figure 2.1: A multispecies model of tumor signaling.
Tumor tissue is composed of two cell types: cancer stem cells (S), and terminally differentiated cells (TC). Stem cells have a probability of self renewal P, differentiate into TCs with probability $1-P$, and divide at a rate K_S. P and K_S are promoted by W signals produced by the stem cells and inhibited by T, which are produced by S and TCs in response to high H, which represents HGF. H acts by both increasing production of W (at low concentrations) and T (at high concentrations). Adapted from [126].

2.2.1 Tumor cell species

We characterize tumor cell dynamics using the cell lineage hypothesis [61, 126]. It has been shown that tumor cells progress through lineage stages where the ability to self-renew is gradually lost [90, 6]. We consider a simplified lineage with cancer stem cell (S) and terminal cell (TC) species that make up the viable fraction of the tumor. Stem cells self-renew, i.e. form new stem cells upon division, with a probability P. We note that in our continuum model, results from asymmetric or symmetric stem cell division are identical, thus we do not make a distinction between these mechanisms of self-renewal. Change in species concentration is a function of the fraction of daughter cells that either remain after division $(2P-1)$ in the case of stem cells, with the factor of '2' accounting for the production of two daughter cells from each parent cell at each cell division, or the fraction of cells that differentiate, $2(1-P)$, in the case of terminal cells, and the cell division rate of each species,

$$\frac{\partial S}{\partial t} = (2P-1)K_S S, \tag{2.1}$$

$$\frac{\partial TC}{\partial t} = 2(1-P)K_S S + K_{TC} TC, \tag{2.2}$$

where $K_{S,TC}$ are the stem and differentiated cell division rates, respectively. We discuss the dependence of K_S on various growth factors below, and assume K_{TC} to be constant, since terminal cells have less variable and lower division rates than CSCs [124]. We set $K_{TC} = 0.1$, as it falls below the lowest observed CCIC division rate of 0.13, which was observed in a mixed (i.e. CSC and TC) population of CCICs [55]. Moreover, we assume that nutrient and oxygen concentrations are not limiting, which is applicable to an experimental cell culture system with proper media, and hence necrosis and apoptosis are negligible.

2.2.2 Stem cell self-renewal rate and division rate

It has been shown that microenvironmental feedback on self-renewal in a tissue cell lineage is necessary for robust control of lineage progression [61]. Current data shows that elements of such

a control system are also present in cancer cell lineages, although often in a dysregulated manner. Indeed, the Wnt/β-catenin system, which involves stem cell-produced glycoproteins from the Wnt family which cause nuclear translocation and activation of transcription factor β-catenin, and is associated with increased cell proliferation and self-renewal in normal tissues, has been shown to be overactivated in several types of tumors, including glioma, meduloblastoma, colon cancer, and hepatocellular carcinoma [32, 1, 43]. These factors are represented by W in the model. Moreover, it has been shown across several tissues and in both normal and early cancerous tissue that growth factors, most notably those from the TGFβ superfamily, are produced that feedback on to the stem cells to reduce rates of cell proliferation and self-renewal [40, 99, 72]. We model the effect of this class of factors using T. Hence, P and K_S are modeled as follows,

$$P = P_{min} + (P_{max} - P_{min})M_P, \tag{2.3}$$

$$K_S = K_{S_{min}} + (K_{S_{max}} - K_{S_{min}})M_{K_S}, \tag{2.4}$$

$$M_{P,K_S} = \left(\frac{\xi_{P,K_S}W}{1+\xi_{P,K_S}W}\right)\left(\frac{1}{1+\psi_{P,K_S}T}\right), \tag{2.5}$$

where P_{min} and P_{max} are minimum and maximum rates of self-renewal, respectively, and $K_{S_{min}}$ and $K_{S_{max}}$ are the minimum and maximum rates of stem cell division, respectively. The functions M_P and M_{K_S} represent the feedback of W and T on P and K_S, respectively. We set $P_{min} = 0.2$ and $P_{max} = 1.0$ to represent the possible extremes of P, and $K_{S_{min}} = 0.1$ and $K_{S_{max}} = 1.0$ as we have found that CCICs have division rates of approximately 0.15 to 0.5 in culture [55]. The upper limit is set to 1.0 since our findings were based on growth rates of CCICs that may have been differentiating, hence the division rates of the stem cells would have to be slightly greater than the aggregated division rate. ξ_{P,K_S} represent the positive effect of W on P and K_S, respectively, and ψ_{P,K_S} represent the inhibitory effect of T on P and K_S, respectively. We set $\xi_P = 1.0$ and $\psi_P = 0.5$. These values were derived by Youssefpour et al. in a model of this system that includes, in addition to Equations (1)-(5), generalized diffusion and convection terms for the cell species [126]. We set $\xi_{K_S} = 0.01$ and $\phi_{K_S} = 0.5$, which were derived using an extension of the Youssefpour model to parametrize growing CCICs in culture [55].

2.2.3 Growth factor concentration

A hallmark of colorectal cancer is disruption and over-activation of the Wnt/β-catenin signaling pathway, often through inactivation of the cytoplasmic β-catenin binding protein APC, or through activating mutations in β-catenin itself [87]. Moreover, it has been shown that several distinct downstream factors of the β-Catenin signal, including Phospholipase D and BMI1, act as activators of the Wnt/β-catenin pathway, creating a positive feedback loop that is nonlinear due to the multiple feedback mechanisms on the pathway [51, 53, 19]. We model this aspect of the W auto regulation using a modified Michaelis-Menten equation, in order to account for signal saturation. Additionally, HGF, acting through its CSC-expressed cognate receptor c-Met, results in translocation of β-catenin to the nucleus, and hence also potentiates Wnt signal. Moreover, as discussed in the introduction, there is evidence that HGF also acts on T at high concentrations [123, 76], although the mechanism by which it does so is currently unknown. Therefore, we model changes to W and T as follows,

$$\frac{\partial W}{\partial t} = \left(\lambda_H H + \frac{\lambda_{PW1} W^2}{1 + \lambda_{PW2} W^2}\right) S - \nu_{DW} W, \tag{2.6}$$

$$\frac{\partial T}{\partial t} = g_i(H)(S + TC) - \nu_{DT} T \quad i = 1, 2, 3, \tag{2.7}$$

where λ_H represents the feedback response of W on H, λ_{PW1} is the strength of the autocrine positive feedback response of W, λ_{PW2} is the Michaelis-Menton constant for W, $\nu_{DW,DT}$ are the decay rates for W and T, respectively, and $g_i(H)$ is the positive feedback function of H on T, which becomes increasingly nonlinear with increasing i (see below). λ_H, λ_{PW1}, and λ_{PW2} are estimated to fit a maximum peak of the dose response curve to approximately 1000%. The value of 1000% is derived from the following observation: in the original experiments with CCICs, the observed maximum growth rate was found to be approximately 2000% [55], but we have found that this growth rate was dependent on initial spheroid size, and when normalized for average spheroid size, the predicted maximum growth rate is approximately 1000% (unpublished observations). Currently,

in vitro decay rates for W and T are unavailable, and hence we set, as a first approximation, $\nu_{DW} = \nu_{DT} = 1.0$ and note that since calculation of λ_H, $\lambda_{PW1,2}$ are dependent on ambient W and T, a change in ν_{DW} or ν_{DT} would necessitate a change in λ_H and $\lambda_{PW1,2}$ to match the tumor growth rate, hence the output in S and TC would be similar to the results for $\nu_{DW} = \nu_{DT} = 1.0$. The effect of H on T is modeled using three different functions, each which differ by (1) the degree of the nonlinearity of H and (2) the modulating factor, which is set to allow the maximum peak growth to be similar between the different functions. We note that, in nature, i need not be an integer, but nevertheless, as i increases, we will show that the post-peak curvature of the dose-response curve will increase, hence while it may not be possible to determine the specific i of the growth factor from the dose-response curve alone, it will be possible to determine the qualitative degree of nonlinearity of action of the negative growth regulator. Therefore, our choice of i act as representative values of the (non-)linear effect of the negative growth regulator. For this study, we set $g_1(H) = 5^{-3}H$, $g_2(H) = 3^{-4}H^2$, and $g_3(H) = 2^{-5}H^3$. We summarize all parameter values in Table 1.

Table 2.1: Summary of parameter values for Equations (2.1) - (2.7).

Parameter	Description	Value
K_{TC}	TC mitosis rate	0.1
P_{min}	Min. CSC self-renewal rate	0.2
P_{max}	Max. CSC self-renewal rate	1.0
$K_{S_{min}}$	Min. CSC mitosis rate	0.1
$K_{S_{max}}$	Max. CSC mitosis rate	1.0
ξ_P	Pos. feedback response of P	1.0
ψ_P	Neg. feedback response of P	0.5
ξ_{K_S}	Pos. feedback response of K_S	0.01
ψ_{K_S}	Neg. feedback response of K_S	0.5
λ_{PW1}	Pos. feedback response of W	1
λ_{PW2}	M-M constant for W	1
λ_H	H feedback response of W	2
$\nu_{D(W,T)}$	Decay rates for W and T, respectively	1

2.2.4 Quasi-steady state Growth factor concentration

In order to analyze the dynamics, we reduced the system by assuming quasi-steady state concentrations for W and T. Setting the time derivatives to 0 in Equations 2.6 and **??** allowed us to solve for W in terms of S and H, and for T in terms of H, S and TC. In the case of W, we obtained the cubic function $0 = -W^3 + W^2S(2H+1) - W + 2H$, and in the case of T, we have $0 = g(H)(CS+TC) - T$. The real solution to the first equation was calculated using the MATLAB symbolic solver,

$$\begin{aligned} W = {} & S/3 + (H - S/6 + (S + 2HS))^{3/27} \\ & + (H - S/6 + (S + 2HS))^{3/27} - ((HS)/3)^2 \\ & - (1/9(S + 2HS)^2 - 1/3)^3)^{1/2} - ((HS)/3)^{1/3} \\ & + (S + 2HS)^{2/9} - 1/3)/(H - S/6 + (S + 2HS)^{3/27} \\ & + ((H - S/6 + (S + 2HS)^{3/27} - (HS)/3)^2 \\ & - (1/9(S + 2HS)^2 - 1/3)^3)^{1/2} - (HS)/3)^{1/3} \\ & + (2HS)/3 \end{aligned} \tag{2.8}$$

For the second equation, we obtain:

$$T = g(H)(S + TC) \tag{2.9}$$

2.3 Results

The equations were numerically solved in MATLAB using MATLAB's standard solver for ordinary differential equations, ode45. Initial conditions were set to model a CCIC culture system. Since CCICs are composed of stem cells derived from primary colon tumors [91], we set $S = 1$ and $TC = 0$, where 1 simulation cell corresponds to 10 biological cells, which is the average number of cells initially in each experiment [55]. Since stem cells produce W but not T, we set $2.0 = W >> T = 0.01$ as initial conditions, with units for all growth

factors in ng/ml. We chose the specific value of 2.0 for W as double to the decay rate so that it does not artificially decay to zero, and 0.01 for T to account for any background levels of the growth factor. The simulation was run over various H values (H is assumed to be constant throughout the simulation). The simulation was run from $t = 0$ to $t = 9$, where t represents the number of days of the simulation. The dose-response curve for % tumor growth at day 9 in increasing concentrations of HGF for the full system is found in Figure **??** and for the quasi-steady state system in Figure 2.3. Note that growth curves for the

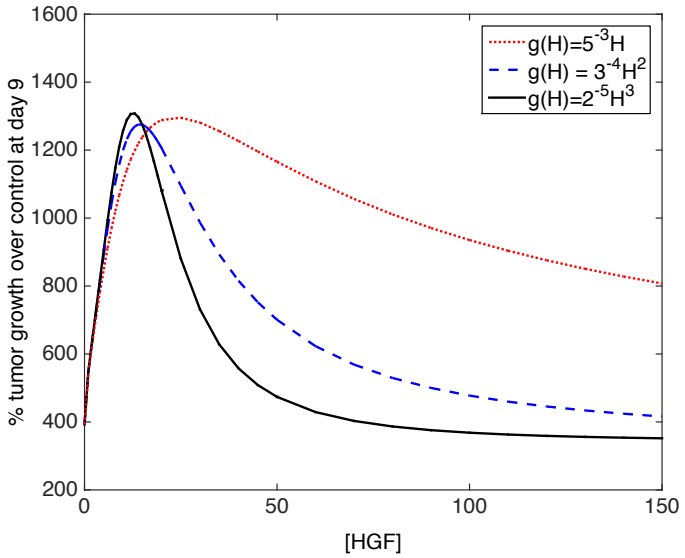

Figure 2.2: Dose-response curve of original ode system (Equations 2.1) - (2.7) for a linear $g(H) = 5^{-3}H$, quadratic $g(H) = 3^{-4}H^2$, and cubic $g(H) = 2^{-5}H^3$.

original and quasi-steady state model are not identical, indeed at very low, but non-zero, concentrations of H, the curve for nonlinear g overestimates cellular growth. This is because if $g(H) = 2^{-5}H^3$, then $T = g(H)(S + TC)$ is very small at low H, and its effect is negligible on P and K_s, resulting in increased growth and proliferation of stem cells, and thus rapid production of W (Figure 2.4 (ii)), therefore the assumption that W is in a quasi-steady state at this concentration of H is not accurate.

Nevertheless, the stem cell, terminal cell, W, and T dynamics are very similar between the two models at both $H = 0$ and higher values of H (Figure 2.5). The peak of both curves

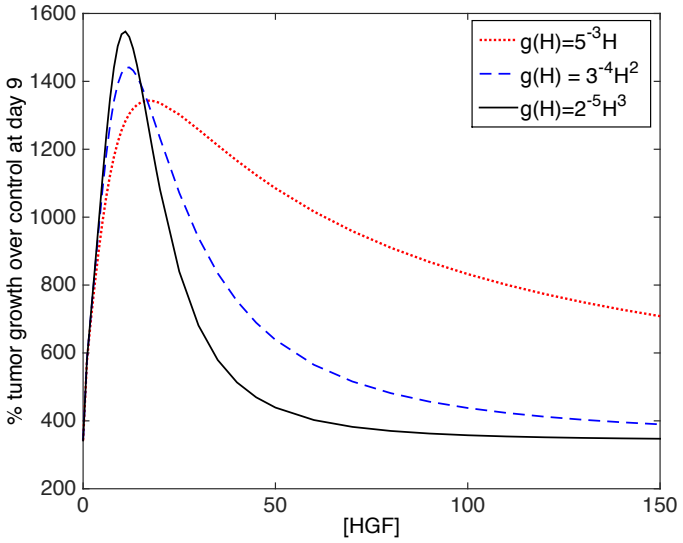

Figure 2.3: Dose-response curve of quasi-steady state system (Equations (1) - (5), (8), (9)) for a linear $g(H) = 5^{-3}H$, quadratic $g(H) = 3^{-4}H^2$, and cubic $g(H) = 2^{-5}H^3$.

occurs at approximately $H = 20$, and at this HGF concentration, stem cell concentrations increase throughout the simulation in both models. Therefore, since our analysis is concentrated on curve behavior in control conditions and after the growth peak is attained, we assume that the quasi-steady state system provides a good approximation of the cell numbers.

A phase plane analysis of stem and terminal cell dynamics shows that at a concentration of H=100, stem cell concentrations tend to 0 over time while terminal cell concentrations increase, whereas at $H = 20$, both stem and terminal cell concentrations increase independent of initial conditions (Figure 2.6 (b),(c)). Interestingly, there is a divergence of stem cell response for $H = 0$, at initial concentrations of less than 2, the stem cell concentration tends to 0, whereas at higher initial concentrations, stem cell concentrations also increase over time. This occurs due to a higher production of W at the initial time points that potentiates the stem cell populations. Therefore, if initial concentrations of stem cells is high, the growth peak would move left on the dose-response curve due to the increase in stem cell growth.

To investigate whether a different choice of g resulted in different relative fractions of stem

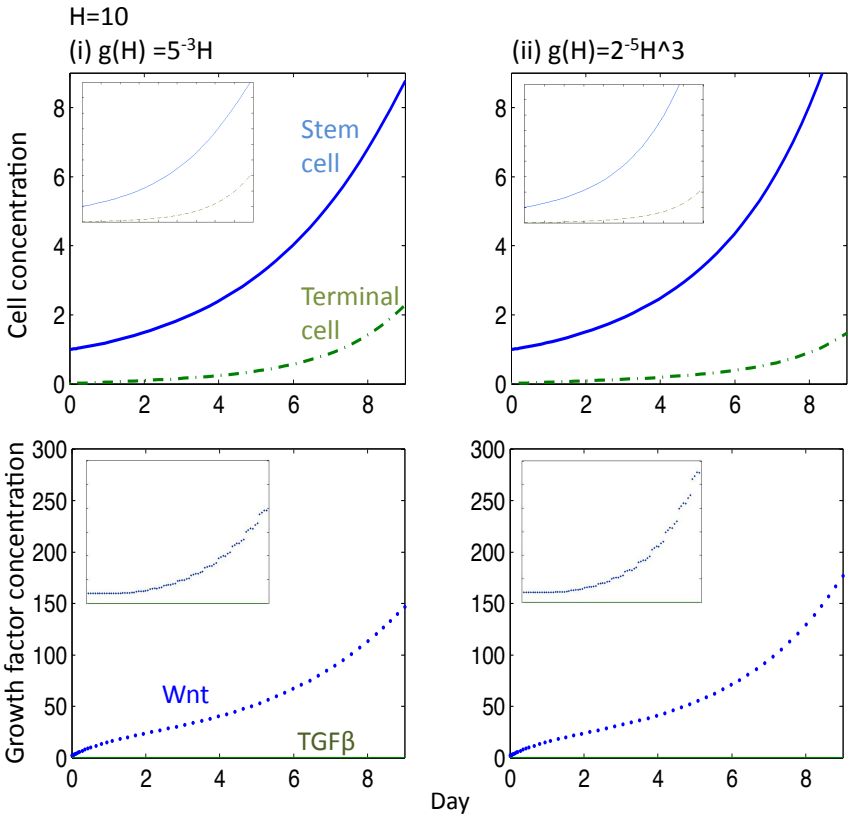

Figure 2.4: Cell and chemical dynamics for the ode model at $H = 10$.
Dynamics of stem cell, terminal cell, W, and T concentrations in the original ode model for linear and cubic g and at H=10. The graph insets for each simulation are the dynamics of the same factor in the quasi-steady state model.

vs. terminal cells at concentrations of H after the peak growth phase, we plotted the stem cell fraction at linear and cubic g at the final time point over concentrations of H ranging from $20 - 100$. Indeed, a cubic g resulted in a nonlinear decrease in stem cell fraction after the peak growth phase, whereas a linear g resulted in a more linear decrease in the stem cell fraction, consistent with the the action of T on stem cell self-renewal (Figure 2.7).

2.4 Discussion

In this study, we analyze the relationship between the mechanism of growth factor-mediated activation of a growth inhibitor at high concentrations and the shape of a biphasic dose-response curve of tissue growth in response to increasing concentrations of growth factor. Since the molecular nature of the inhibitor activation is often unknown, the shape of an experimental growth curve can serve as an aid in generating hypotheses of growth factor action. For example, if the curve post-peak segment (CPPS) displays low curvature (i.e. is near linear), then most likely there is no synergy of inhibitor activation by the growth factor. For example, in the Yamada et al. study on HGF effect on muscle satellite cell proliferation, the CPPS is linear (Figure 2.8). Therefore, we hypothesize that *either* HGF acts via biphasic activation of c-Met, *or* via a low-affinity growth receptor to stimulate myostatin production. On the other hand, if the CPPS shows high curvature, then we hypothesize that the growth factor increases expression of the growth inhibitor in a non-linear fashion. Experimental examples of such growth curves include NGF action on neurite outgrowth and copper chloride action on bacterial colony formation (Figure 2.9). In biological signaling, a nonlinear signal is often indicative of activation of multiple downstream effectors [8, 79]. Hence, a nonlinear CPPS may be indicative of pleiotropic action of the growth factor on growth inhibition.

Moreover, we also show that nonlinear activation of an inhibitor results in a nonlinear decline in the stem cell fraction in the cell population with increasing H after the peak growth concentration (Figure 2.7). Experimental establishment of this relationship requires use of a CSC marker such as CD133, which is specific to colon CSCs [15], and can serve to provide evidence that the growth antagonist acts on P and K_S, hence further substantiating details of the mathematical model. Additionally, use of a CSC marker can give insight into the predictions of the phase plane analysis, specifically that peak growth is dependent on the steady state of CSCs: peak growth occurs at H concentration where CSC populations increase during the entire time course of the experiments (i.e., do not tend towards the

alternative steady state of 0) (Figure 2.6). A simplification of the current model to make it amenable to analytical analysis may also be used to confirm the stability results.

2.5 Conclusions

Our simple model of HGF action on cell proliferation in a multi-species colon cancer models serves to establish the hypothesis that a shape analysis of a dose-response curve can inform molecular mechanism of growth factor action. Moreover, the model can be extended to include different hypotheses on activator induction by the growth factor, or in cases where the growth curve is monotonic, the shape analysis can be performed on the pre-peak curve segment or the entire curve, respectively. Generation of experimental dose-response curves and subsequent curve shape analysis using a system where the molecular mechanism of action of a growth factor on the phenotypic output is known can be used to test the model predictions.

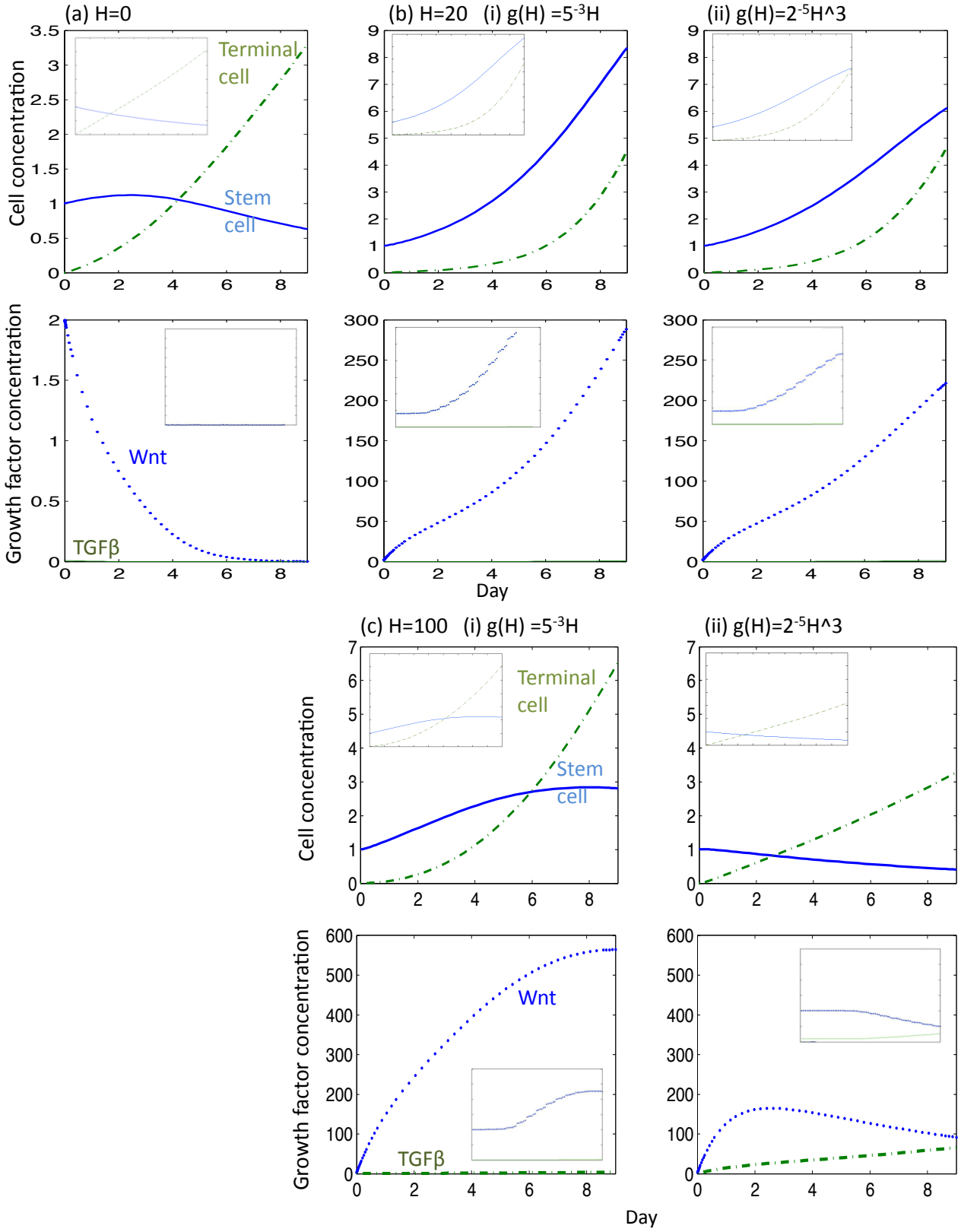

Figure 2.5: Dynamics of stem cell, terminal cell, W, and T concentrations in the original model for linear and cubic g and at concentrations of (a) H=0, (b) H=20, and (c) H=100. The graph insets for each simulation are the dynamics of the same factor in the quasi-steady state model.

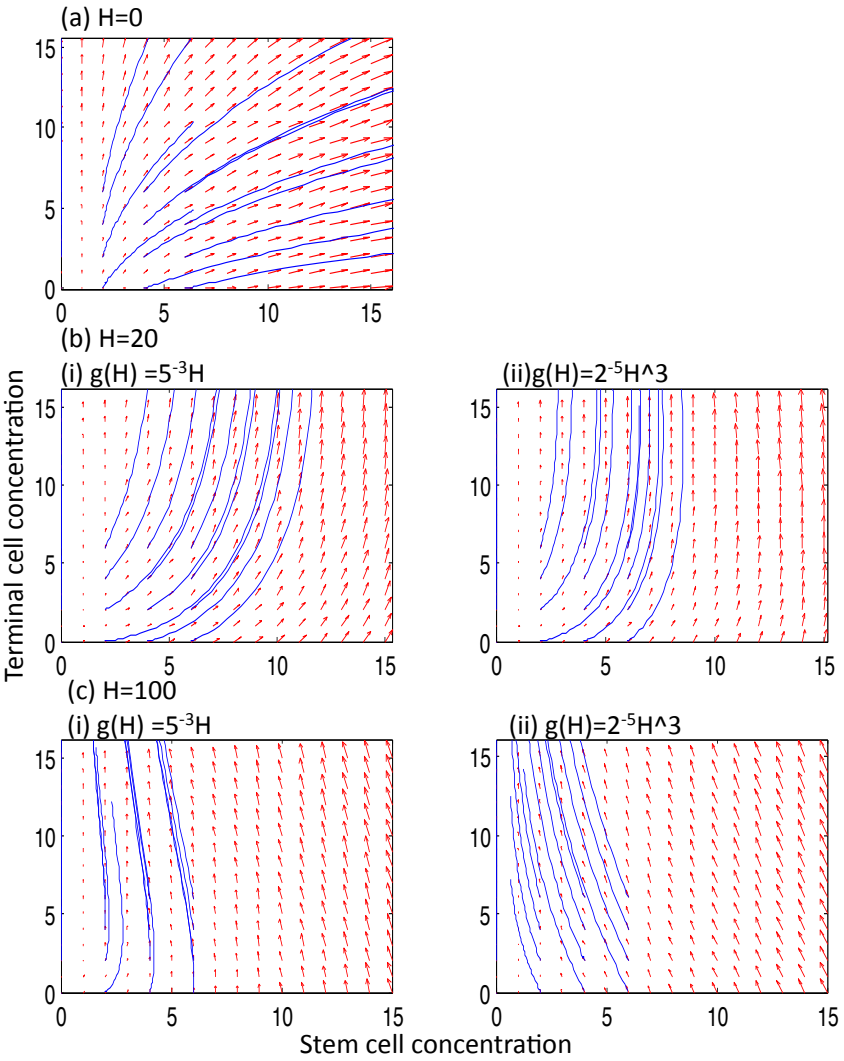

Figure 2.6: Phase planes of stem and terminal cell dynamics for the quasi-steady state system at (a) $H = 0$, (b) $H = 20$, with linear and cubic $g(H)$, and (c) $H = 100$, with linear and cubic $g(H)$. Solutions are plotted for initial conditions ranging from 0-6 stem and terminal cells (each).

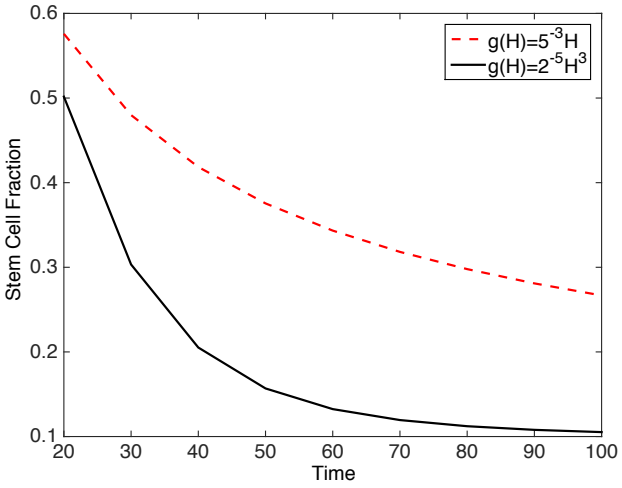

Figure 2.7: Stem cell fraction at $t = 9$ and $20 \leq H \leq 100$ for the quasi-steady state system at linear and cubic $g(H)$.

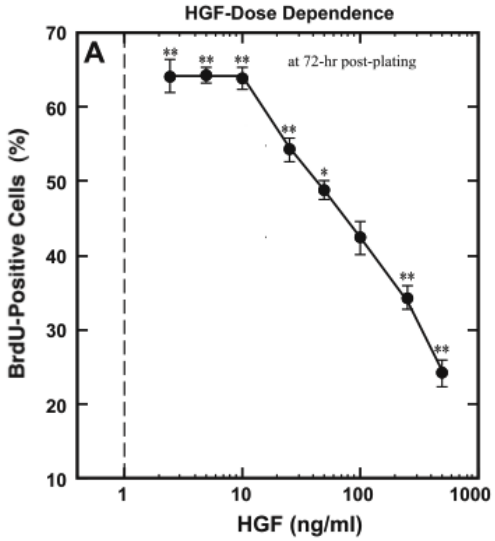

Figure 2.8: Example of a linear dose-response curve
BrdU, a thymidine analogue, is incorporated into newly synthesized DNA of replicating cells, and can be detected using anti-BrdU antibodies. Hence, it acts as a marker of cell proliferation. The dose-response curve of BrdU uptake by satellite muscle cells in response to increasing HGF shows a linear post-peak decline in BrdU-positive cells with increasing HGF (Reprinted with permission from [123]).

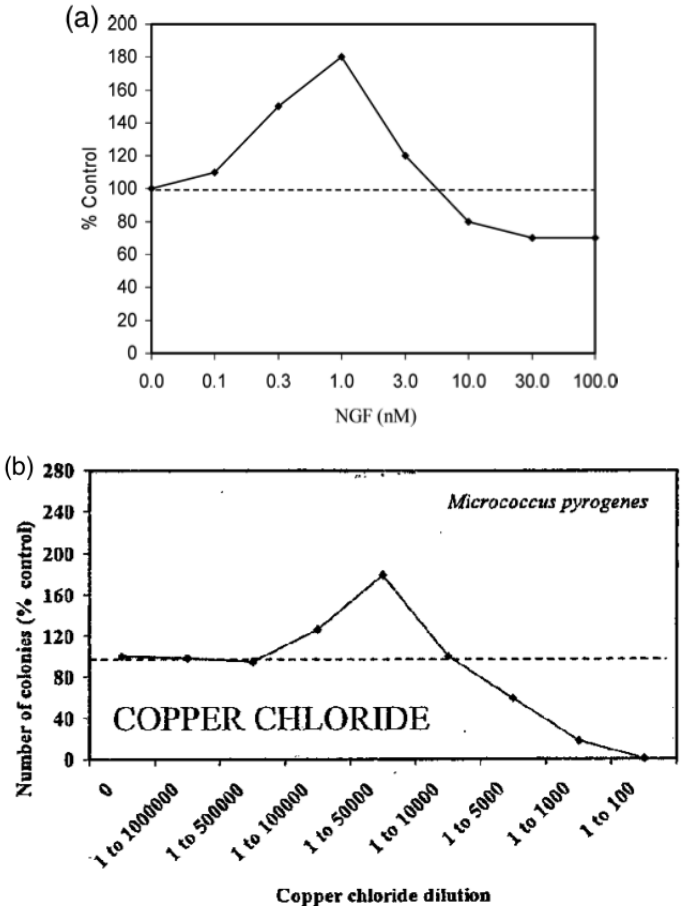

Figure 2.9: Examples of non-linear dose-response curves
(a) effect of NGF on neuronal outgrowth in dorsal root ganglion neurons of rat lumbar region (reprinted with permission from [12]), (b) effect of Copper Chloride on growth of *Micrococcus Pyrogenes* bacterial cultures (reprinted with permission from [14]).

Chapter 3

Feedback control in a stem cell model can cause an Allee effect

3.1 Introduction

Over the past several years, Lowengrub and collaborators have developed a sophisticated model for tumor growth in tissue [119, 68, 126]. Their model consists of approximately 12 coupled partial differential equations, which account for cancer cell growth in tissue including volume effects, tissue stiffness and viscosity, external and internal forces, cell differentiation into cancer stem cells (SC), transient cells (TC), terminally differentiated cells (TD), and dead cells. In addition, they incorporate a feedback, which regulates the self-renewal of the stem cell population. This feedback mechanism is based upon two signaling proteins, a short-range activator (Wnt) and a long-range inhibitor (Dkk). The dynamics of these two proteins is modeled through a Turing mechanism, which allows for spatial patterning.

Lowengrub et al. use their model to investigate several scenarios which are relevant for tumor growth and treatment. In particular, they design a combination treatment, which,

in simulations, results in tumor extinction [126]. The purpose of this chapter is to try to understand the basic underlying mechanism which leads to treatment success. We claim that the feedback mechanisms used in this model lead to an Allee effect for tumor stem cell growth. The Allee effect is a phenomenon, studied in ecology, that there exists a positive correlation between population density and individual fitness [102]. In the case of a tumor, the Allee effect can manifest itself through treatment, which can cause the stem cell count to fall below a threshold such that the tumor cannot recover and dies out, or in spontaneous tumor remission [56]. This Allee effect is not easily seen in the fully coupled PDE model. Hence, here we simplify down to the essential dynamics and prove mathematically that an Allee effect exists.

Our simplification focuses on the interplay between the stem cell concentration, $S(t)$, and the self-renewal activator Wnt, $a(t)$. In the original model of Lowengrub et al., the activator Wnt ($a(t)$) is coupled to the inhibitor ($b(t)$) by the Turing mechanism

$$\begin{aligned} a_t &= D_1 \Delta a + \gamma \frac{a^2}{b} S - a \\ b_t &= D_2 \Delta b + \gamma a^2 S - \nu b, \end{aligned} \tag{3.1}$$

where D_1, D_2 are the diffusion coefficients, Δ denotes the Laplacian operator, γ and ν are positive parameters and the index notation denotes partial derivatives. The dynamics of the stem cell concentration, $S(t)$, is given by

$$S_t = (2p(T, a) - 1)kS, \tag{3.2}$$

which includes two feedback mechanisms. The variable $p(T, a)$ denotes the probability of self renewal of stem cells, and this depends on concentration of T, a differentiation promoter, and on the activator a. For simplification purposes, the proliferation rate k is taken to be constant and non-negative.

In Youssefpour et al [126], the probability of self renewal has the following specific form

$$p(T,a) = p_{min} + (p_{max} - p_{min}) \left(\frac{\xi a}{1+\xi a} \right) \left(\frac{1}{1+\psi T} \right), \tag{3.3}$$

where T is concentration of soluble differentiation promoters (most importantly, these include members the TGFβ superfamily). p_{min} and p_{max} are respective minimum and maximum rates of self-renewal and ξ and ψ are the respective positive, by a, and negative, by T, feedback strengths on p. In our simplified model, we substitute T for S using the following reasoning: any probability of self-renewal < 1 will lead to production of differentiated cells, D, from stem cells. Differentiated cells will, in turn, produce T. Therefore, there exists a positive relationship between S and D, and hence T. We take the simplest assumption that S and T are directly correlated to obtain

$$p(S,a) = p_{min} + (p_{max} - p_{min}) \left(\frac{\xi_1 a}{1+\xi_1 a} \right) \left(\frac{1}{1+\xi_2 S} \right),$$

Further simplifying by setting $p_{min} = 0$ and $p_{max} = 1$, we obtain

$$p(S,a) = \left(\frac{\xi_1 a}{1+\xi_1 a} \right) \left(\frac{1}{1+\xi_2 S} \right), \tag{3.4}$$

where ξ_1 and ξ_2 represent the respective strengths of positive and negative feedback on p.

In our numerical investigations, we find that the Turing mechanism is not essential for the Allee effect. However, the Wnt production terms in the a equation are relevant. Hence in our simplification, we focus on the kinetic part of the activator equation (now written as an ODE, since space dependence is ignored):

$$\dot{a}(t) = \gamma \frac{S}{b} a^2 - a, \tag{3.5}$$

where we assume that the inhibitor b is a given constant value. For given S, this equation

(3.5) is a bistable equation. Solutions to initial conditions $a(0) < b/S$ converge to zero, while solutions to initial conditions $a(0) > b/S$ blow up in finite time. This blow-up is not seen in the full Turing model, since the inhibitor controls unbounded growth. To mitigate this effect, we introduce λ, the strength of the saturation (thus forcing $\dot{a}$ to saturate to a linear rate). We believe that this is a biologically reasonable assumption, since experimental evidence has shown that tumor cells are highly responsive to external drivers of a, such as activation of the c-MET receptor by stromal-produced HGF, in a concentration-dependent manner [39, 80]. Therefore, in a model with no external drivers of a, which we present here, we do not assume that a can saturate. Therefore, we study

$$\dot{a} = a\left(\frac{\beta S a}{1+\lambda a} - 1\right), \tag{3.6}$$

where $\beta = \gamma/b$. Then the model, which describes the feedback mechanism on the stem cells, is given by

$$\begin{aligned} \dot{S} &= (2p(S,a)-1)kS = f_1(S,a) \\ \dot{a} &= a\left(\frac{\beta S a}{1+\lambda a} - 1\right) = f_2(S,a) \\ p(S,a) &= \frac{\xi_1 a}{1+\xi_1 a}\frac{1}{1+\xi_2 S}, \end{aligned}$$

3.2 Analysis of the Allee-effect

For the analysis below, we consider the following system of two differential equations:

$$\begin{aligned} \dot{S} &= (2p(S,a)-1)kS = f_1(S,a), \\ \dot{a} &= a\left(\frac{\beta S a}{1+\lambda a} - 1\right) = f_2(S,a), \end{aligned} \tag{3.7}$$

where $p(S,a) = (\xi_1 a)/((1+\xi_1 a)(1+\xi_2 S))$. The main result shows that the above system (3.7) does show an Allee-effect.

For linear stability analysis, we will need to use p_S, p_a, F_S, and F_a, therefore we calculate them now.

$$\begin{aligned}
p_S &= -\frac{a\xi_2}{(1+\xi_1 a)(1+\xi_2 S)^2} \leq 0 \text{ where } p_S = 0 \text{ only when } a = 0,\\
p_a &= \frac{1}{(1+\xi_2 S)(1+\xi_1 a)^2} > 0,\\
(f_2)_S &= \frac{\beta a^2}{1+\lambda a} \geq 0 \text{ where } F_S = 0 \text{ only when } a = 0,\\
(f_2)_a &= \frac{2\beta S a(1+\lambda a) - (\beta S a^2)\lambda}{(1+\lambda a)^2} - 1 = \frac{2\beta S a + 2\lambda\beta S a^2 - \lambda\beta S a^2}{(1+\lambda a)} - 1,\\
&= \frac{2\beta S a + \lambda\beta S a^2}{(1+\lambda a)^2} - 1 = \frac{\beta S a(2+\lambda a)}{(1+\lambda a)^2} - 1.
\end{aligned}$$

Therefore, we have

$$(f_2)_a = \frac{\beta S a(2+\lambda a)}{(1+\lambda a)^2} - 1. \tag{3.8}$$

Note that the sign of $(f_2)_a$ depends upon β, S, a and λ.

Theorem 3.1. *1. The domain $\Omega = [0,\infty) \times [0,\infty)$ is positively invariant for (3.7).*

2. The system (3.7) has two steady states in Ω, $P_1(0,0)$ and $P_2(S_2, A_2)$, where P_2 is the unique intersection of the curves

$$\{p(S,a) = 0.5\} \quad \textit{and} \quad \{f_2(S,a) = 0\}.$$

3. P_1 is asymptotically stable and P_2 is a saddle point.

4. Under specific assumptions on parameter relationships, there exists a separatrix which separates the basin of attraction of P_1 from an attractor with non-zero S. This sepa-

ratrix forms the threshold between population extinction P_1 and population growth.

Proof. Consider system (3.7). We observe that $\dot{S} \geq -kS$ and $\dot{a} \geq -a$. Setting $\dot{S}+kS = l(1)$ and $\dot{a}+a = l(2)$ and solving each differential equation under the condition that $(l(1), l(2)) \geq (0,0)$ gives us the condition that $(S(t), a(t)) \geq (0,0)$ for all initial $(S,a) \geq (0,0)$. Thus, $\Omega = [0,\infty] \times [0,\infty)$ is positively invariant for (3.7).

We find $\dot{S} = 0$ if and only if $S = 0$, $p(S,a) = 0.5$, or $k = 0$. The second equation is in steady state if $a = 0$ or $a = a^*(S) = (\beta S - \lambda)^{-1}$, $S > 0$. We note that when $S = 0$, $a^*(S) = \frac{-1}{\lambda} < 0$ since λ is assumed to be non-negative. This cannot be a steady state since $a \geq 0$. Similarly, if $a = 0$, then $p(S,0) = 0$. Hence, the only steady state with $S = 0$ or $a = 0$ is $P_1(0,0)$.

We next want to determine if there exist, and if yes, how many, pairs of (S,a) such that $p(S,a) = 0.5$ and $F(S,a) = 0$. This can be found by solving the system:

$$\begin{cases} \dfrac{\xi_1 a}{1+\xi_1 a}\dfrac{1}{1+\xi_2 S} = 0.5 \\ \\ \dfrac{\beta S a}{1+\lambda a} = 1 \end{cases} \tag{3.9}$$

Solving the first equation for S, we obtain $S = (\xi_1 a - 1)/(\xi_2(1+\xi_1 a))$. We first note that the function is monotone increasing in a. This is true since $S' = (2\xi_1)(\xi_2(1+\xi_1 a)^2) > 0$. Moreover, we have

$$\lim_{a\to 0}\left(\frac{\xi_1 a - 1}{\xi_2(1+\xi_1 a)}\right) = -\frac{1}{\xi_2} \text{ and } \lim_{a\to\infty}\left(\frac{\xi_1 a - 1}{\xi_2(1+\xi_1 a)}\right) = \frac{1}{\xi_2}$$

Repeating the process for the second equation, we obtain $S = (1+\lambda a)/(\beta a) = 1/(\beta a)+\lambda/\beta$, $S' = \frac{-1}{\beta a^2} < 0$, hence the function is monotone decreasing, and

$$\lim_{a\to 0}\frac{1}{\beta a} + \frac{\lambda}{\beta} = \infty \text{ and } \lim_{a\to\infty}\frac{1}{\beta a} + \frac{\lambda}{\beta} = \frac{\lambda}{\beta}.$$

Therefore, the constraints on S, a and the parameters guarantee existence of a unique solution if $\frac{\lambda}{\beta} < \frac{1}{\xi_2}$ $(*)$. In the linear stability analysis below, whenever we discuss $P_2(S_2, A_2)$, the steady state corresponding to (3.7), we assume that the inequality $(*)$ is satisfied. The Jacobian of (3.7) is

$$J(S,a) = \begin{pmatrix} 2p_S kS + (2p-1)k & 2p_a kS \\ (f_2)_S & (f_2)_a \end{pmatrix} \tag{3.10}$$

For $P_1(0,0)$ we have we have $p(0,0) = 0$, $p_S = 0$, $p_a = \xi_2$, $(f_2)_S = 0$, and $(f_2)_a = -1$. Therefore, we have

$$J(0,0) = \begin{pmatrix} -k & 0 \\ 0 & -1 \end{pmatrix},$$

which gives two negative eigenvalues. Hence the system is an asymptotically stable node.

For $P_2(S_2, A_2)$, where we denote $p_{(S,2)} = p_S(S_2, A_2)$, $p_{(a,2)} = p_a(S_2, A_2)$, $(f_2)_{(S,2)} = (f_2)_S(S_2, A_2)$, and $(f_2)_{(a,2)} = (f_2)_a(S_2, A_2)$, the Jacobian is

$$J(S_2, A_2) = \begin{pmatrix} 2p_{(S,2)} kS_2 & 2p_{(a,2)} kS_2 \\ (f_2)_{S,2} & (f_2)_{a,2} \end{pmatrix}$$

We recall that $p_S < 0$, $p_a > 0$, and $(f_2)_S > 0$. Since we also have $(\beta S_2 A_2)/(1 + \lambda A_2) = 1$ by (3.9), we obtain

$$(f_2)_{a,2} = \frac{\beta S_2 A_2 (2 + \lambda A_2)}{(1 + \lambda A_2)^2} - 1 = \frac{2 + \lambda A_2}{1 + \lambda A_2} - 1 = \frac{1}{1 + \lambda A_2} > 0.$$

Therefore, we have $(f_2)_{a,2} > 0$, and hence the determinant of $J(S_2, A_2)$ is

$$\det J(S_2, A_2) = 2p_{(S,2)} kS_2 (f_2)_{(a,2)} - 2p_{(a,2)} kS_2 (f_2)_{(S,2)} < 0, \tag{3.11}$$

which makes P_2 a saddle point.

The Stable Manifold Theorem (SMT) [84] guarantees existence of a separatrix, M, separating the basins of attraction of P_1 from a non-zero attractor when $(*)$ is satisfied. $\square$

3.3 Dependence of the separatrix on parameters

For the system (3.7) to have a steady state other than $P_1(0,0)$, it must satisfy the inequality $\lambda/\beta < 1/\xi_2$ $(*)$. In biological terms, λ is the saturation term for $\dot{a}$, and β is a positive parameter of a auto-activation, normalized by a constant level of stem-cell derived Wnt inhibitor, b. Therefore, λ/β is increased when there is strong saturation and / or low self-activation strength, and is decreased when the saturation strength is low and / or self-activation strength is high. In more advanced cancers, it has been shown that the Wnt cascade is often constitutively activated and response to growth inhibitors is lowered [39, 58], which means that a-saturation strength decreases and β increases, hence λ/β decreases in more advanced cancers. ξ_2 represents the inhibitory effect of S on p. Therefore, if the inhibitory effect of S on p is strong, then $1/\xi_2$ will be low, and the inequality is less likely to be satisfied, thereby leading to one steady state of $P_1(0,0)$. On the other hand, a low strength of p-inhibition (hence giving a relatively high $1/\xi_2$) occurs with more advanced cancers. Thus, we see that as a cancer progress, the inequality $(*)$ is more likely to be satisfied, thereby altering the long-term system dynamics towards a higher probability that $(S,a) \not\to (0,0)$.

The Stable Manifold Theorem (SMT) [84] allows us to approximate the separatrix, M, when $(*)$ is satisfied. In Appendix C, a second approximation to M, in a transformed coordinate system (y_1, y_2), is calculated and given by (C.15), we relabel this approximation as M^*. To simplify notation, we will also refer to this approximation as M^* after coordinate

transformation to (S, a). Since it will be unreasonable to continue to the third approximation by the SMT, we check whether M^* is a good approximation of M by comparing its output to the separatrix predicted for a given set of parameters by a numerical ODE analysis program (in this case, pplane8 in Matlab, [3]). We choose two sets of parameters, $Pr_1(\xi_1, \xi_2, \lambda, k, \beta) = (1, 1, 1, 1, 2)$ and $Pr_2 = (5, 0.5, 1, 1, 4)$, where Pr_2 represents a more invasive set of parameters than Pr_1. To plot M^*, we input a discreet set of values for y_1 and use $y_2 = M^*(y_1)$ to obtain $(S^*, a^*) = C^{-1}y$, $(S^*, a^*) = (S - S_2, a - A_2)$ with y and C defined in Appendix C. Using pplane8, we see that the stable manifold for Pr2 is shifted southwest of Pr_1, with the result that the Pr_2 system will have a non-zero steady state for a lower threshold of S, a then Pr_1 (Figure 3.1 a,b). We plot M^* for Pr_1 and Pr_2, overlay these results with the stable manifold predicted by pplane8, and note that the shape and location M^* is near the numerically-predicted stable manifold (Figure 3.1 c,d). We proceed to analyze M^* in order to establish a dependence between the parameters of the model and behavior of the separatrix.

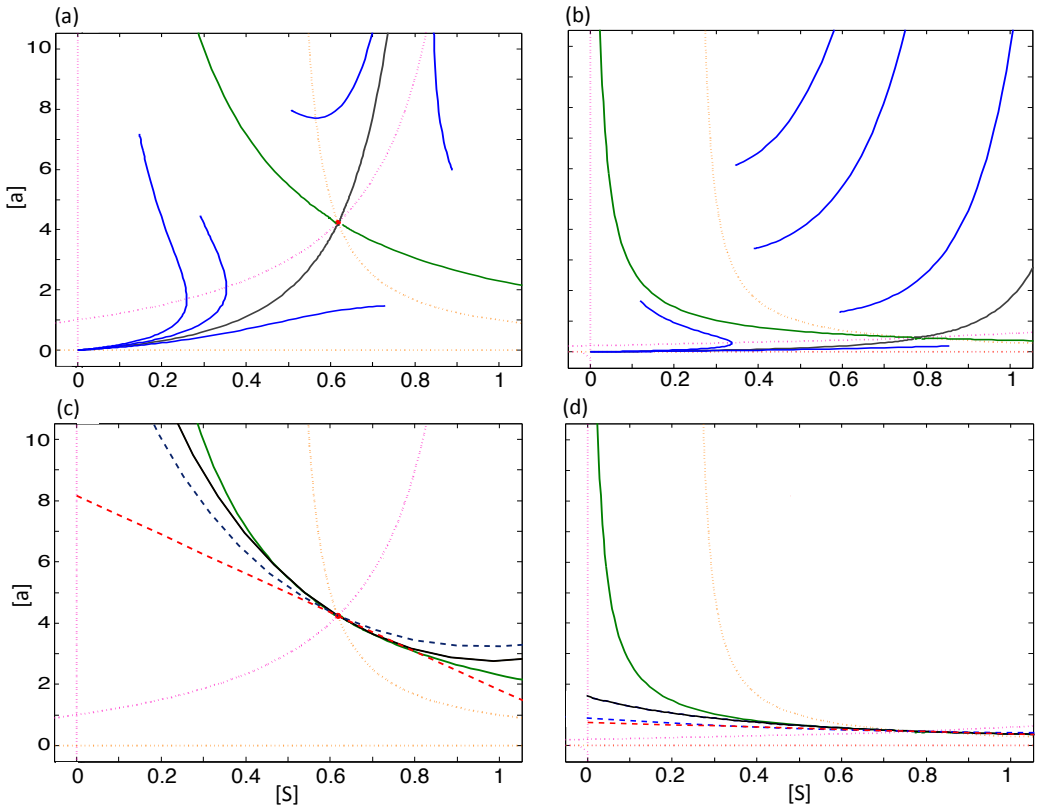

Figure 3.1: Application of the Stable Manifold Theorem to approximate the separatrix of System (3.7).
(a,b) pplane8 plots of (3.7) with parameters (a) Pr_1 and (b) Pr_2. The descending curve in each graph is the pplane approximation of the stable manifold (separatrix) (green), the pplane approximation of the unstable manifold is the ascending curve (grey), and the blue curves represent forward solutions of the respective system. Note that solutions to the right of the separatrix tend to a non-zero equilibrium, whereas solutions to the left tend to $(0, 0)$. (c,d) The separatrices predicted by pplane8 (green) of Pr_1 (c) and Pr_2 (d) are plotted along with the SMT approximation of the separatrix, M^* (black), the quadratic approximation, M_q^* (dash, blue), and the linear approximation, M_l^* (dash, red). For all panels, the a nullcline is orange and S nullcline purple.

Due to the complex dependence of M^* on parameters, we take the linear and quadratic portion of M^*, M_l^* and M_q^*, respectively, given in Equations (C.27) and (C.29). We plot M_l^* and M_q^* for the two parameter sets, Pr_1 and Pr_2 in Figure 3.1 c,d. Noting that M_l^* gives an approximation of the tangent line to the separatrix, we concentrate our analysis on the parameter dependence of M_l^*.

From the linear approximation of M^*, M_l^*, we develop an 'Allee index', A_I, given by the area below M_l^*. This 'Allee Region' is the basin of attraction for the steady state representing tumor extinction, $P_1(0,0)$, and hence $A_I = A_I(\xi_1, \xi_2, k, \beta, \lambda)$ is inversely correlated with tumor invasiveness. The dependence of A_I on various parameter regimes provides information on how parameter values influence the susceptibility of the tumor to the Allee effect (Fig. 3.2). We find that increasing ξ_2, the strength of inhibition of p_0 by S, increases A_I for all parameter regimes. The increase in A_I comes about due to a ξ_1-dependent increase in A_2 and magnitude of m_l, the slope of M_l^* (which is always negative) (Figs. 3.3, 3.4). Although S_2 decreases as ξ_2 increases, it does not tend to zero, indeed, as $\xi_2 \to \beta/\lambda$, by (3.9), $S_2 \to \lambda/\beta$. Conversely, increasing ξ_1, the strength of activation of p_0 by a, results in a decreased A_I by the opposite mechanisms as decreasing ξ_2: there is an increase in magnitude of m_l, a decrease of A_2, and an increase of S_2 that cannot compensate for the decrease in A_I (Figure 3.2 (i,iii)). Generally, increasing β from 2 to 4 also decreases A_I due to the same mechanisms as when increasing ξ_1, and the increase also extends the range of ξ_2 that satisfies $(*)$. For low ξ_2 and ξ_1, increasing β from 2 to 4 decreases A_I by a different mechanism. For example, at $\xi_2 = 0$, $\lambda = 1$, and $k = 1$, the m_l increase in magnitude from ≈ -15 to ≈ -35. A_2 does not change significantly but S_2 decreases from ≈ 0.5 to ≈ 0.25 (indeed, $\lim(S_2)_{\xi_1 \to 0} = \lambda/\beta$). From the above discussion, we observe that invasive regimes come about due to an (S_2, A_2) that is near the (S, A) axis, with a slope that is close to parallel to the nearest axis if (S_2, A_2) is not near $(0,0)$.

Finally, we consider the dependence of A_I on k, the stem cell division rate. Unlike the

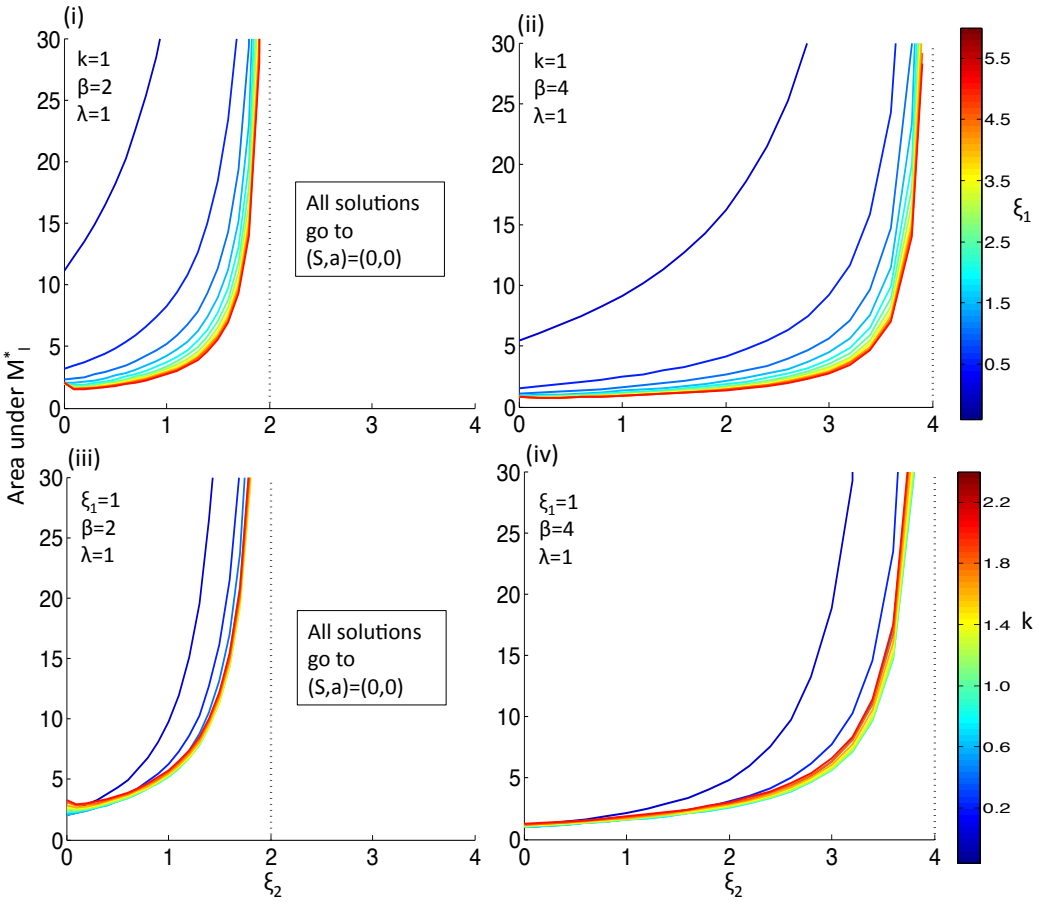

Figure 3.2: The Allee Index as a function of parameters.
The Allee Index, the area in the region bounded above by M_l^*, is plotted for increasing ξ_2 and for increasing ξ_1 (i, ii) or k (iii, iv) under less ($\beta = 2$, (i,iii)) or more ($\beta = 4$, (ii,iv)) invasive conditions. Note that the range of ξ_2 is dependent on β and λ, since for the system to have a non-trivial attractor, the inequality $\lambda/\beta < 1/\xi_2$ must be satisfied.

other parameters, (A_2, S_2) is not dependent on k. In Figure 3.2 (iii),(iv) we see that as k initially increases from 0, there is a drop in A_I (except for very low ξ_2), but afterwards there is a minor increase in A_I with increasing k. The slope, m_l, decreases in magnitude with increasing k (Figure 3.3 (iii),(iv)). Since (A_2, S_2) does not change with increasing k and the slope becomes less negative, the loss in A_I from shifting the a intercept towards the origin is compensated for by increasing the S intercept of M_l^* (Figure 3.5).

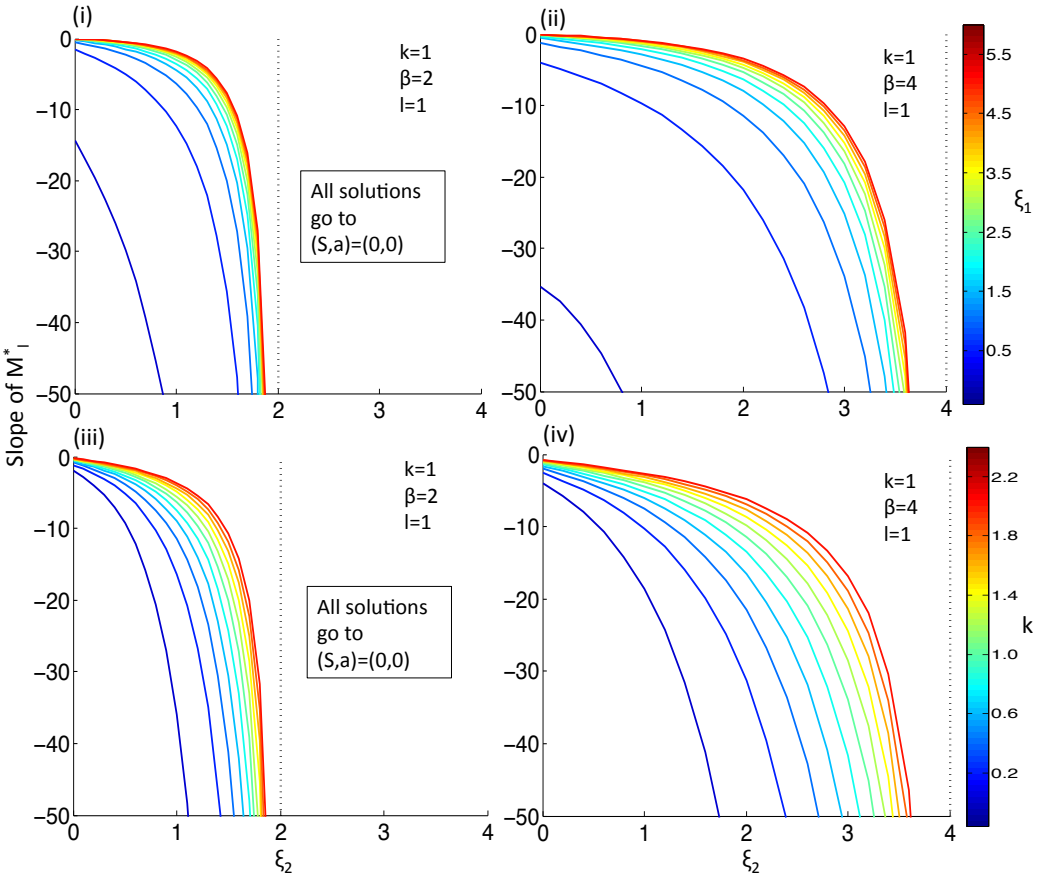

Figure 3.3: The slope of M_l^*, m_l, as a function of parameters.
The slope of M_l^*, m_l, is plotted for increasing ξ_2 and for increasing ξ_1 (i, ii) or k (iii, iv) under less ($\beta = 2$, (i,iii)) or more ($\beta = 4$, (ii,iv)) invasive conditions.

3.4 Long-term system behavior

We now consider how the system (3.7) behaves for longer time. Returning to our two parameter sets, $\mathrm{Pr}_1(\xi_1, \xi_2, \lambda_k, \beta) = (1, 1, 1, 1, 2)$ and $\mathrm{Pr}_2(\xi_1, \xi_2, \lambda_k, \beta) = (5, 0.5, 1, 1, 4)$, we consider two sets of initial conditions. We take $\mathrm{IC}_1(S, a) = (0.2, 3)$ and $\mathrm{IC}_2(S, a) = (0.5, 5)$. From Fig. 3.1, we see that IC_1 lies in the Allee Region for Pr_1, but not Pr_2. In Fig. 3.6(a), we plot the trajectories obtained from solving (3.7) numerically (using the ode45 function in Matlab) for initial conditions IC_1 at Pr_1 (solid lines) and Pr_2 (dashed lines). For Pr_1, (S, a) predictably tend to $(0, 0)$, whereas for Pr_2, a continues to increase while S stabilzes at $S = 2$. For initial conditions IC_2 (Fig. 3.6(b)), a increases for both Pr_1 and Pr_2, but the

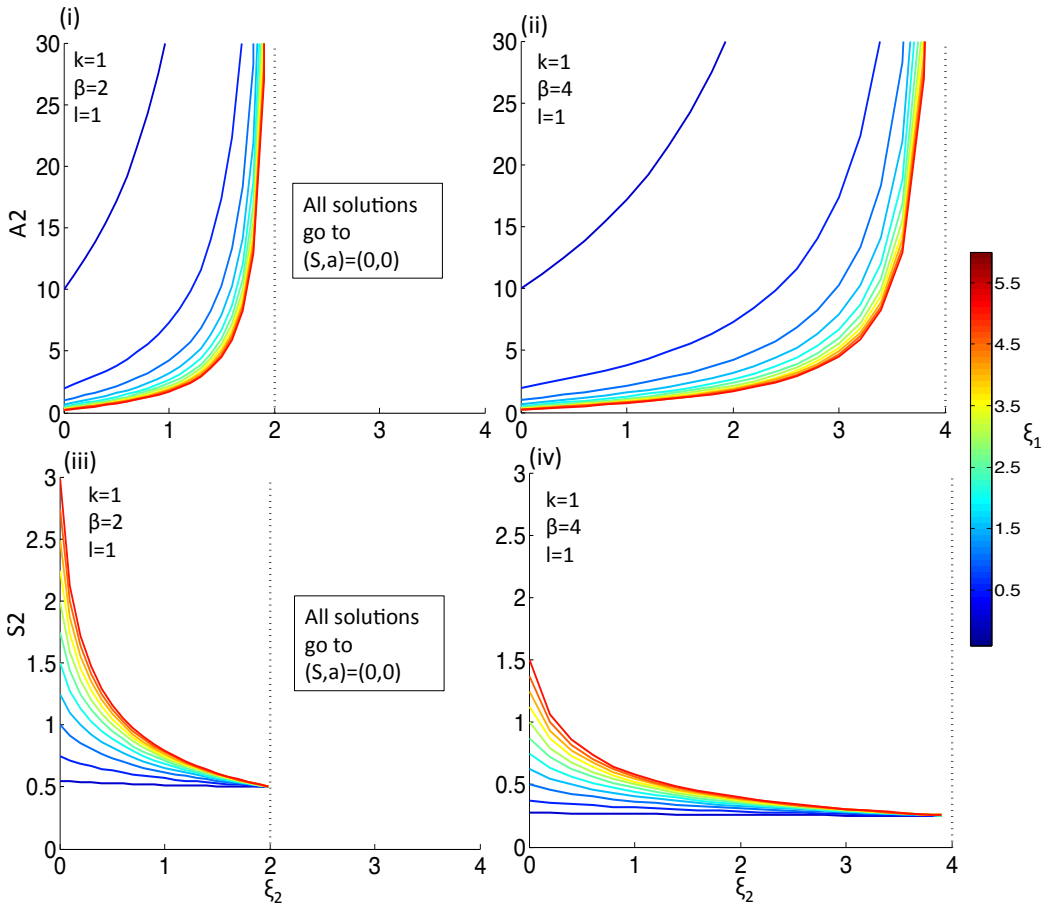

Figure 3.4: The steady state $P_2(S_2, A_2)$ as a function of parameters.
The steady state $P_2(S_2, A_2)$ is plotted for increasing ξ_2 and for increasing ξ_1 (i, ii) or k (iii, iv) under less ($\beta = 2$, (i,iii)) or more ($\beta = 4$, (ii,iv)) invasive conditions.

rate of increase is higher for Pr_1. S stabiles for both Pr_1 (at $S = 1$) and Pr_2 (at $S = 2$). When the initial conditions are in the invasive region, the limiting behavior on $\dot{a}$ is a linear function in a proportional to $(\beta S)/\lambda$. The limiting behavior on S as a increases can be found by considering $\dot{S}_{\lim_{a\to\infty}} = \{(2p(S,a) - 1)kS\}_{\lim_{a\to\infty}}$,

$$\dot{S}_{\lim_{a\to\infty}} = \left(\frac{2}{1+\xi_2 S} - 1\right) kS \tag{3.12}$$

This is a separable differential equation with positive solution

$$S(t)^\star = \frac{2\xi_2 + e^{(-kt)-c}(\sqrt{4\xi_2 e^{kt+c} + 1} + 1)}{2\xi_2^2} \tag{3.13}$$

Figure 3.5: Example of dependence of System 3.7 on k.
We consider the system (3.7) with $\mathrm{Pr}_1 = (\xi_1, \xi_2, \lambda, k, \beta) = (1, 1, 1, 1, 2)$ (solid lines) and $\mathrm{Pr}_1^* = (\xi_1, \xi_2, \lambda, k, \beta) = (1, 1, 1, 2, 2)$ (dashed lines) and plot M (green) and M_I^* (red). R_1 represents the region in the phase space that is invasive for Pr_1^*, but in the basin of attraction of $(0, 0)$ for Pr_1. Conversely, R_2 represents the region in the phase space that is invasive for Pr_1, but in the basin of attraction of $(0, 0)$ for Pr_1^*.

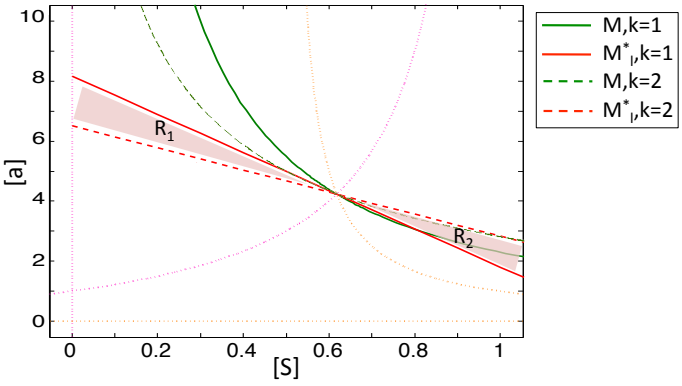

where c is an arbitrary constant and $S(t)^\star$ is the solution to (3.12). We observe that $\lim_{t\to\infty} S(t)^\star = 1/\xi_2$, indicating that the long-term behavior of S in the invasive regime is only proportional to ξ_2. We note that for Pr_1, where $\xi_2 = 1$, $\lim_{t\to\infty} S^*(t) = 1$ and for Pr_2, where $\xi_2 = 0.5$, $\lim_{t\to\infty} S^*(t) = 2$.

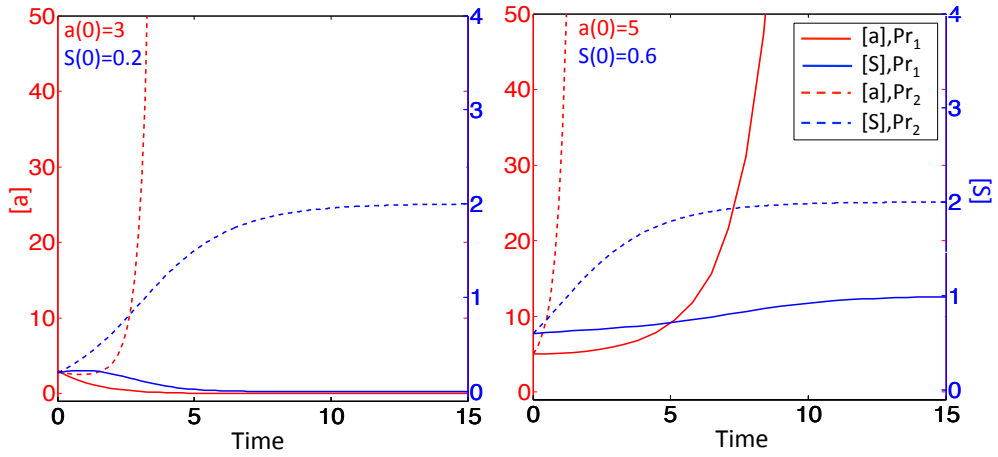

Figure 3.6: Sample trajectories for Pr_1 and Pr_2
Plotting the numerical solutions of (3.7) with initial conditions $(S, a) = (0.2, 3)$ (left panel) and $(S, a) = (0.6, 5)$ (right panel) with parameters $\mathrm{Pr}_1(\xi_1, \xi_2, \lambda_k, \beta) = (1, 1, 1, 1, 2)$ (solid lines) and $\mathrm{Pr}_2(\xi_1, \xi_2, \lambda_k, \beta) = (5, 0.5, 1, 1, 4)$ (dashed lines).

3.5 Discussion

It has recently been suggested that exploitation of the Allee effect in tumor growth should be considered for therapy development [56]. We have simplified a model of tumor growth in order to understand the principles under which a tumor can become eradicated, i.e. exhibit an Allee effect. We have shown that for such a simplified system, there exists a separatrix which distinguishes between trajectories of (S, a) tending to $(0, 0)$ and non-zero solutions. The location of the separatrix depends on the various parameters in the model, specifically on strength of a-dependent activation (ξ_1) and S-dependent inhibition (ξ_2) of the probability of self-renewal p_0, the stem cell division rate, k, and the strength of a self-activation, β. An approximation of the separatrix by the Stable Manifold Theorem has allowed us to explore the dependence of the separatrix on parameters. We can use this system to consider how different therapies can modify tumor behavior and, in some cases, lead to tumor eradication. Conversely, we can also use the system to consider how common events in tumor progression can also modify tumor behavior.

Classical chemotherapeutic drugs against cancer are cytotoxic drugs that target rapidly dividing cells [69, 73]. In our model, such drugs would correspond to lowering the k and S of a system. We have observed that lowering k decreases the slope of M_l^* without changing (A_2, S_2). Following a sample parameter scheme (Pr_1) in Figure 3.5, we see that lowering k from 2 to 1 changes region 1, R_1, which has high a and low S values, from an invasive regime to a regime that is susceptible to the Allee effect. Thus, our model predicts that cytotoxic chemotherapy may make cells more resistant to high levels of activator. Moreover, while the regime 2, R_2 which has high S and low a values changes from being an attractor for tumor extinction to an attractor for the invasive phenotype, the tumor is less likely to be in this region after cytotoxic chemotherapy since the level of S will be reduced. Since chemotherapy is often administered alongside radiation and surgery, both therapies which reduce S, our system shows that these types of therapy may cause tumor extinction not only by lowering

S until the (S, a) values lie in the Allee region, but by expanding the Allee region to be more inclusive of tumors with high levels of activator.

Another major modality in cancer treatment is what is known as targeted therapy, which acts by interfering with proteins involved in carcinogenesis [60]. A number of Wnt pathway inhibitors are currently in preclinical development and have shown promise in slowing growth and inducing cell death in *in vitro* and *in vivo* experimental systems [1]. In our model, targeted Wnt therapy corresponds to either lowering ξ_1, which increases A_I, or a directly, which may move the system into the basin of attraction for extinction. Additionally, our model can also give insight into patient outcomes. For example, elevated levels of nuclear β-catenin, a downstream signaling target of the Wnt cascade, in the excised tumors of patients who had undergone surgery and therapy for colorectal cancer, were strongly correlated with poor patient survival [18]. In our model, this phenomenon translates to a system where lowered levels of S and k via surgery and therapy do not induce tumor extinction because high a levels maintain the system in the invasive region. Our model thus predicts that treatments that combine traditional cancer therapy (surgery and cytotoxic chemotherapy) with targeted inhibitors would be more effective by pushing the system into the Allee region of the phase space.

The dependence of the system behavior on the strength of inhibition of p by S, ξ_2, is of particular interest since tumor response to growth inhibitors decreases throughout tumor progression [37]. A decrease in ξ_2 in our system decreases A_I and increases the limiting value of S in the invasive region to $1/\xi_2$. Therefore, a decrease in response to growth inhibitors has the dual effect of decreasing the probability that traditional chemotherapy and/or surgery will cause the tumor to become extinct, and increasing the long-term population of stem cells. Indeed, a decrease in response to the growth inhibitors of the TGFβ family is correlated with poorer clinical prognosis. It may be this dual action in promoting tumor survival and growth that has selected the decreased response to growth inhibitors to be a major hallmark

of cancer.

We have shown, with a simple stem cell and chemical activator model, that a tumor can undergo the Allee effect either spontaneously or after treatment when the system is in the basin of attraction for extinction. By considering tumor remission in the language of dynamical systems, we have been able to quantify and observe how various parameters of the system, include strength of action of activators and inhibitors of stem cell probability of self-renewal, strength of activator self-propagation, and cell division rate, all contribute to defining the Allee region in the phase space of the tumor and activator. We have kept the model purposefully simple in order to allow an analytical approach to the question of tumor eradication, but a careful extension to include microenvironmental components, such as host-produced HGF upregulation of a, and/or more complex assumptions on the cell division rate k (for example, assuming that k is positively correlated with a) or other parameters may be able to provide further insight on the dependence of the Allee effect in cancer to external and internal system behavior.

Discussion

In this thesis, we have explored the effect of the microenvironment on tumor growth using mathematical models of varying complexity. In Chapter 1, a spatiotemporal, multiscale, multiphase model was used to examine the phenotypic outcome of a tumor-host dynamic signaling program involving production of HGF by the host tissue and HGF-stimulating growth factors by the tumor tissue. Simulation results of the model showed that activation of the HGF/c-Met axis increased cell dispersal, and contributed to heterogeneity at the tumor-host boundary, leading to morphological instability. Lowering response of the tumor to negative feedback signal served to further increase the morphological instability. Therapy targeted at disrupting the HGF/c-Met axis was effective in stabilizing tumor growth and morphology, making it more likely that complementary treatment, including surgery and chemotherapy, would lead to cancer remission. The model in Chapter 1 did not incorporate recent finding that at very high HGF, tumor growth is abrogated, due to lack of knowledge of molecular mechanism of the phenomenon.

In Chapter 2, the original model was simplified to a system of 4 ordinary differential equations that incorporated a negative effect of HGF on tumor growth via positive up regulation of TGFβ at high concentration. By testing several models of HGF action on TGFβ, we were able to derive simulated dose-response curves that could help to distinguish different mechanisms of HGF action. The results predicted that the shape of dose-response curves could be informative in predicting how a growth factor can act as a negative growth regulator.

Finally, we simplified the model even further to a system of two ordinary differential equations for stem cells and activators of stem cell self-renewal in order to analytically explore the conditions under which a tumor can undergo an Allee effect, or die out, when its density is small enough. The resulting analysis showed that the strength of both positive and negative feedback on stem-cell self-renewal, as well as strength of self-activation of the activator molecules and rate of stem cell division all contribute to determining how likely a tumor will die out, given a certain concentration of stem cells and activator molecules. This system provides a framework from which one can examine how specific patient / tumor characteristics can be predictive of therapy effectiveness.

Many of our assumptions and results are based upon quantification of specific features of the tumor and its microenvironment, including, especially for Chapter 1, the spatially-distributed stem cell fraction of the tumor, and chemical diffusion, uptake, and activity coefficients. In order to better align our model with experimental observations, it is necessary to use an experimental system that is capable of recapitulating and capturing some of the complexities of the TME. In their review of emerging technologies in this field, Guldner and Zhang noted that new technology is necessary to explore TME that incorporates spatial and temporal dynamics of TME interactions, and can measure cell-type specific behavior. They discuss emerging technologies that can aide in this goal, including deep tissue optical sectioning, intravital microscopy (IVM, the imaging of live animal tissue), and *in situ* cell-type specific genetic isolation [35]. For example, Tanaka et al. used IVM in a liver metastatic xenograft system where RFP-labeled human colorectal cells were injected into GFP-expressing nude mice to obtain a time-series of of the phenotypic changes in tumor and host during liver metastasis and with and without chemotherapy [107]. In addition, development of sophisticated 3D-culture systems where protein and drug diffusion and uptake rates can be measured via techniques such as FRAP or FLIM-FRET, are already in use [21, 106]. The hypotheses generated by our models regarding quantifiable tumor behavior with activated HGF/c-Met axis, such as increased invasiveness, formation of areas with high stem-cell concentration at

the tumor-host boundary, decrease in growth rates at very high HGF, and eradication under certain therapies, can be tested in an appropriate experimental system.

The overarching goal of this thesis has been to examine and quantify, via mathematical methods, tumor microenvironment dynamics, with a specific focus on host-derived HGF action on solid tumor growth. With the results and modeling frameworks developed in this thesis, we hope to contribute to the burgeoning mathematical oncology community in order to aide in development of more mathematically and quantitatively oriented cancer therapeutics.

Bibliography

[1] J. N. Anastas and R. T. Moon. Wnt signalling pathways as therapeutic targets in cancer. *Nat Rev Cancer*, 13(1):11–26, Jan 2013.

[2] A. R. A. Anderson, A. M. Weaver, P. T. Cummings, and V. Quaranta. Tumor morphology and phenotypic evolution driven by selective pressure from the microenvironment. *Cell*, 127(5):905–15, Dec 2006.

[3] D. Arnold and J. Polking. *Ordinary Differential Equations using Matlab*. Prentice Hall, second edition, 1999.

[4] N. A. Bhowmick, E. G. Neilson, and H. L. Moses. Stromal fibroblasts in cancer initiation and progression. *Nature*, 432(7015):332–7, Nov 2004.

[5] C. Birchmeier, W. Birchmeier, E. Gherardi, and G. F. Vande Woude. Met, metastasis, motility and more. *Nat Rev Mol Cell Biol*, 4(12):915–25, Dec 2003.

[6] C. Blanpain and B. D. Simons. Unravelling stem cell dynamics by lineage tracing. *Nat Rev Mol Cell Biol*, 14(8):489–502, Aug 2013.

[7] G. R. Blumenschein, Jr, G. B. Mills, and A. M. Gonzalez-Angulo. Targeting the hepatocyte growth factor-cmet axis in cancer therapy. *J Clin Oncol*, 30(26):3287–96, Sep 2012.

[8] E. P. Böttinger and M. Bitzer. Tgf-beta signaling in renal disease. *J Am Soc Nephrol*, 13(10):2600–10, Oct 2002.

[9] V. Brinkmann, H. Foroutan, M. Sachs, K. Weidner, and W. Birchmeier. Hepatocyte growth factor/scatter factor induces a variety of tissue-specific morphogenic progrmas in epithelial cells. *J Cell Biol*, 131(6 Pt 1):1573–86, 1995.

[10] H. M. Byrne. Dissecting cancer through mathematics: from the cell to the animal model. *Nat Rev Cancer*, 10(3):221–30, Mar 2010.

[11] E. J. Calabrese. Paradigm lost, paradigm found: the re-emergence of hormesis as a fundamental dose response model in the toxicological sciences. *Environ Pollut*, 138(3):379–411, Dec 2005.

[12] E. J. Calabrese. Enhancing and regulating neurite outgrowth. *Crit Rev Toxicol*, 38(4):391–418, 2008.

[13] E. J. Calabrese. Hormetic mechanisms. *Crit Rev Toxicol*, 43(7):580–606, Aug 2013.

[14] E. J. Calabrese and L. A. Baldwin. Hormesis: a generalizable and unifying hypothesis. *Crit Rev Toxicol*, 31(4-5):353–424, Jul 2001.

[15] V. Catalano, S. Di Franco, F. Iovino, F. Dieli, G. Stassi, and M. Todaro. Cd133 as a target for colon cancer. *Expert Opin Ther Targets*, 16(3):259–67, Mar 2012.

[16] F. Cecchi, D. C. Rabe, and D. P. Bottaro. Targeting the hgf/met signaling pathway in cancer therapy. *Expert Opin Ther Targets*, 16(6):553–72, Jun 2012.

[17] M. A. J. Chaplain, S. R. McDougall, and A. R. A. Anderson. Mathematical modeling of tumor-induced angiogenesis. *Annu Rev Biomed Eng*, 8:233–57, 2006.

[18] P. Y. Cheah, P. H. Choo, J. Yao, K. W. Eu, and F. Seow-Choen. A survival-stratification model of human colorectal carcinomas with beta-catenin and p27kip1. *Cancer*, 95(12):2479–86, Dec 2002.

[19] J.-H. Cho, M. Dimri, and G. P. Dimri. A positive feedback loop regulates the expression of polycomb group protein bmi1 via wnt signaling pathway. *J Biol Chem*, 288(5):3406–18, Feb 2013.

[20] J. G. Christensen, J. Burrows, and R. Salgia. c-met as a target for human cancer and characterization of inhibitors for therapeutic intervention. *Cancer Lett*, 225(1):1–26, Jul 2005.

[21] J. R. W. Conway, N. O. Carragher, and P. Timpson. Developments in preclinical cancer imaging: innovating the discovery of therapeutics. *Nat Rev Cancer*, 14(5):314–28, May 2014.

[22] V. Cristini, H. B. Frieboes, R. Gatenby, S. Caserta, M. Ferrari, and J. Sinek. Morphologic instability and cancer invasion. *Clin Cancer Res*, 11(19 Pt 1):6772–9, Oct 2005.

[23] P. Dalerba, R. W. Cho, and M. F. Clarke. Cancer stem cells: models and concepts. *Annu Rev Med*, 58:267–84, 2007.

[24] A. De Luca, M. Gallo, D. Aldinucci, D. Ribatti, L. Lamura, A. D'Alessio, R. De Filippi, A. Pinto, and N. Normanno. The role of the egfr ligand/receptor system in the secretion of angiogenic factors in mesenchymal stem cells. *J Cell Physiol*, Dec 2010.

[25] T. S. Deisboeck, Z. Wang, P. Macklin, and V. Cristini. Multiscale cancer modeling. *Annu Rev Biomed Eng*, 13:127–55, Aug 2011.

[26] M. J. Duffy. The urokinase plasminogen activator system: role in malignancy. *Curr Pharm Des*, 10(1):39–49, 2004.

[27] R. Eftimie, J. L. Bramson, and D. J. D. Earn. Interactions between the immune system and cancer: a brief review of non-spatial mathematical models. *Bull Math Biol*, 73(1):2–32, Jan 2011.

[28] H. B. Frieboes, X. Zheng, C.-H. Sun, B. Tromberg, R. Gatenby, and V. Cristini. An integrated computational/experimental model of tumor invasion. *Cancer Res*, 66(3):1597–604, Feb 2006.

[29] A. Gierer and H. Meinhardt. A theory of biological pattern formation. *Kybernetik*, 12(1):30–39, Dec 1972.

[30] E. Gohda, T. Matsunaga, H. Kataoka, T. Takebe, and I. Yamamoto. Induction of hepatocyte growth factor in human skin fibroblasts by epidermal growth factor, platelet-derived growth factor and fibroblast growth factor. *Cytokine*, 6(6):633–40, Nov 1994.

[31] E. Gohda, T. Matsunaga, H. Kataoka, and I. Yamamoto. Tgf-beta is a potent inhibitor of hepatocyte growth factor secretion by human fibroblasts. *Cell Biol Int Rep*, 16(9):917–26, Sep 1992.

[32] A. Gong and S. Huang. Foxm1 and wnt/-catenin signaling in glioma stem cells. *Cancer Res*, 72(22):5658–62, Nov 2012.

[33] W. M. Grady, A. Rajput, L. Myeroff, D. F. Liu, K. Kwon, J. Willis, and S. Markowitz. Mutation of the type ii transforming growth factor-beta receptor is coincident with the transformation of human colon adenomas to malignant carcinomas. *Cancer Res*, 58(14):3101–4, Jul 1998.

[34] C. R. Graveel, D. Tolbert, and G. F. Vande Woude. Met: a critical player in tumorigenesis and therapeutic target. *Cold Spring Harb Perspect Biol*, 5(7), Jul 2013.

[35] I. H. Guldner and S. Zhang. A journey to uncharted territory: new technical frontiers in studying tumor-stromal cell interactions. *Integr Biol (Camb)*, 7(2):153–61, Feb 2015.

[36] D. Hanahan and L. M. Coussens. Accessories to the crime: functions of cells recruited to the tumor microenvironment. *Cancer Cell*, 21(3):309–22, Mar 2012.

[37] D. Hanahan and R. Weinberg. The hallmarks of cancer. *Cell*, 100(1):57–70, 2000.

[38] D. Hanahan and R. A. Weinberg. Hallmarks of cancer: the next generation. *Cell*, 144(5):646–74, Mar 2011.

[39] D. Hanahan and R. A. Weinberg. Hallmarks of cancer: the next generation. *Cell*, 144(5):646–74, Mar 2011.

[40] A.-P. G. Haramis, H. Begthel, M. van den Born, J. van Es, S. Jonkheer, G. J. A. Offerhaus, and H. Clevers. De novo crypt formation and juvenile polyposis on bmp inhibition in mouse intestine. *Science*, 303(5664):1684–6, Mar 2004.

[41] P. Harrison, L. Bradley, and A. Bomford. Mechanism of regulation of hgf/sf gene expression in fibroblasts by tgf-beta1. *Biochem Biophys Res Commun*, 271(1):203–11, Apr 2000.

[42] E. M. Hol, W. H. Gispen, and P. R. Bär. Acth-related peptides: receptors and signal transduction systems involved in their neurotrophic and neuroprotective actions. *Peptides*, 16(5):979–93, 1995.

[43] J. D. Holland, A. Klaus, A. N. Garratt, and W. Birchmeier. Wnt signaling in stem and cancer stem cells. *Curr Opin Cell Biol*, 25(2):254–64, Apr 2013.

[44] S. S. Huang and J. S. Huang. Tgf-beta control of cell proliferation. *J Cell Biochem*, 96(3):447–62, Oct 2005.

[45] T. Ikari, A. Hiraki, K. Seki, T. Sugiura, K. Matsumoto, and K. Shirasuna. Involvement of hepatocyte growth factor in branching morphogenesis of murine salivary gland. *Dev Dyn*, 228(2):173–84, 2003.

[46] M. Jeffers, S. Rong, and G. F. Vande Woude. Enhanced tumorigenicity and invasion-metastasis by hepatocyte growth factor/scatter factor-met signalling in human cells concomitant with induction of the urokinase proteolysis network. *Mol Cell Biol*, 16(3):1115–25, Mar 1996.

[47] C. M. Jones, N. Armes, and J. C. Smith. Signalling by tgf-beta family members: short-range effects of xnr-2 and bmp-4 contrast with the long-range effects of activin. *Curr Biol*, 6(11):1468–75, Nov 1996.

[48] K. M. Joo, J. Jin, E. Kim, K. Ho Kim, Y. Kim, B. Gu Kang, Y.-J. Kang, J. D. Lathia, K. H. Cheong, P. H. Song, H. Kim, H. J. Seol, D.-S. Kong, J.-I. Lee, J. N. Rich, J. Lee, and D.-H. Nam. Met signaling regulates glioblastoma stem cells. *Cancer Res*, 72(15):3828–38, Aug 2012.

[49] C. T. Jordan, M. L. Guzman, and M. Noble. Cancer stem cells. *N Engl J Med*, 355(12):1253–61, Sep 2006.

[50] R. Kalluri and M. Zeisberg. Fibroblasts in cancer. *Nat Rev Cancer*, 6(5):392–401, May 2006.

[51] D. W. Kang, S.-H. Lee, J. W. Yoon, W.-S. Park, K.-Y. Choi, and D. S. Min. Phospholipase d1 drives a positive feedback loop to reinforce the wnt/beta-catenin/tcf signaling axis. *Cancer Res*, 70(10):4233–42, May 2010.

[52] P. Katira, R. T. Bonnecaze, and M. H. Zaman. Modeling the mechanics of cancer: effect of changes in cellular and extra-cellular mechanical properties. *Front Oncol*, 3:145, 2013.

[53] D. Kim, O. Rath, W. Kolch, and K.-H. Cho. A hidden oncogenic positive feedback loop caused by crosstalk between wnt and erk pathways. *Oncogene*, 26(31):4571–9, Jul 2007.

[54] B. S. Knudsen and G. Vande Woude. Showering c-met-dependent cancers with drugs. *Curr Opin Genet Dev*, 18(1):87–96, Feb 2008.

[55] A. Konstorum, S. A. Sprowl, M. L. Waterman, A. D. Lander, and J. S. Lowengrub. Elaboration of a multispecies model of solid tumor growth with tumor-host interactions. In V. In, A. Palacios, and P. Longhini, editors, *International Conference on Theory and Application in Nonlinear Dynamics*, Understanding Complex Systems, pages 295–303. Springer, 2012.

[56] K. S. Korolev, J. B. Xavier, and J. Gore. Turning ecology and evolution against cancer. *Nat Rev Cancer*, 14(5):371–80, May 2014.

[57] J. A. Krall, E. M. Beyer, and G. MacBeath. High- and low-affinity epidermal growth factor receptor-ligand interactions activate distinct signaling pathways. *PLoS One*, 6(1):e15945, 2011.

[58] M. Krausova and V. Korinek. Wnt signaling in adult intestinal stem cells and cancer. *Cell Signal*, 26(3):570–9, Mar 2014.

[59] A. Kreso and J. E. Dick. Evolution of the cancer stem cell model. *Cell Stem Cell*, 14(3):275–91, Mar 2014.

[60] E. L. Kwak, J. W. Clark, and B. Chabner. Targeted agents: the rules of combination. *Clin Cancer Res*, 13(18 Pt 1):5232–7, Sep 2007.

[61] A. D. Lander, K. K. Gokoffski, F. Y. M. Wan, Q. Nie, and A. L. Calof. Cell lineages and the logic of proliferative control. *PLoS Biol*, 7(1):e15, Jan 2009.

[62] G. F. Le Bras, H. A. Loomans, C. J. Taylor, F. L. Revetta, and C. D. Andl. Activin a balance regulates epithelial invasiveness and tumorigenesis. *Lab Invest*, 94(10):1134–46, Oct 2014.

[63] J. Li, S. A. Reed, and S. E. Johnson. Hepatocyte growth factor (hgf) signals through shp2 to regulate primary mouse myoblast proliferation. *Exp Cell Res*, 315(13):2284–92, Aug 2009.

[64] M. Li, X. Xin, T. Wu, T. Hua, H. Wang, and H. Wang. Stromal cells of endometrial carcinoma promotes proliferation of epithelial cells through the hgf/c-met/akt signaling pathway. *Tumour Biol*, Mar 2015.

[65] Y. Li, A. Li, M. Glas, B. Lal, M. Ying, Y. Sang, S. Xia, D. Trageser, H. Guerrero-Cázares, C. G. Eberhart, A. Quiñones-Hinojosa, B. Scheffler, and J. Laterra. c-met signaling induces a reprogramming network and supports the glioblastoma stem-like phenotype. *Proc Natl Acad Sci U S A*, 108(24):9951–6, Jun 2011.

[66] Y. C. Lim, H. J. Kang, and J. H. Moon. C-met pathway promotes self-renewal and tumorigenecity of head and neck squamous cell carcinoma stem-like cell. *Oral Oncol*, 50(7):633–9, Jul 2014.

[67] Y. Lombardo, A. Scopelliti, P. Cammareri, M. Todaro, F. Iovino, L. Ricci-Vitiani, G. Gulotta, F. Dieli, R. de Maria, and G. Stassi. Bone morphogenetic protein 4 induces differentiation of colorectal cancer stem cells and increases their response to chemotherapy in mice. *Gastroenterology*, 140(1):297–309, Jan 2011.

[68] J. S. Lowengrub, H. B. Frieboes, F. Jin, Y.-L. Chuang, X. Li, P. Macklin, S. M. Wise, and V. Cristini. Nonlinear modelling of cancer: bridging the gap between cells and tumours. *Nonlinearity*, 23(1):R1–R9, 2010.

[69] V. Malhotra and M. C. Perry. Classical chemotherapy: mechanisms, toxicities and the therapeutic window. *Cancer Biol Ther*, 2(4 Suppl 1):S2–4, 2003.

[70] N. V. Mantzaris, S. Webb, and H. G. Othmer. Mathematical modeling of tumor-induced angiogenesis. *J Math Biol*, 49(2):111–87, Aug 2004.

[71] S. D. Markowitz and M. M. Bertagnolli. Molecular origins of cancer: Molecular basis of colorectal cancer. *N Engl J Med*, 361(25):2449–60, Dec 2009.

[72] J. Massagué. Tgfbeta in cancer. *Cell*, 134(2):215–30, Jul 2008.

[73] R. H. J. Mathijssen, A. Sparreboom, and J. Verweij. Determining the optimal dose in the development of anticancer agents. *Nat Rev Clin Oncol*, 11(5):272–81, May 2014.

[74] K. Matsumoto and T. Nakamura. Hepatocyte growth factor and the met system as a mediator of tumor-stromal interactions. *Int J Cancer*, 119(3):477–483, Aug 2006.

[75] J. P. Medema. Cancer stem cells: the challenges ahead. *Nat Cell Biol*, 15(4):338–44, Apr 2013.

[76] G. K. Michalopoulos, W. C. Bowen, K. Mulè, and J. Luo. Hgf-, egf-, and dexamethasone-induced gene expression patterns during formation of tissue in hepatic organoid cultures. *Gene Expr*, 11(2):55–75, 2003.

[77] H. L. Moses and R. Serra. Regulation of differentiation by tgf-beta. *Curr Opin Genet Dev*, 6(5):581–6, Oct 1996.

[78] T. Muller, G. Bain, X. Wang, and J. Papkoff. Regulation of epithelial cell migration and tumor formation by beta-catenin signaling. *Exp Cell Res*, 280(1):119–133, Oct 2002.

[79] R. Najdi, R. F. Holcombe, and M. L. Waterman. Wnt signaling and colon carcinogenesis: beyond apc. *J Carcinog*, 10:5, 2011.

[80] T. Nakamura, K. Matsumoto, A. Kiritoshi, Y. Tano, and T. Nakamura. Induction of hepatocyte growth factor in fibroblasts by tumor-derived factors affects invasive growth of tumor cells: in vitro analysis of tumor-stromal interactions. *Cancer Res*, 57(15):3305–13, Aug 1997.

[81] T. Nakamura, T. Nishizawa, M. Hagiya, T. Seki, M. Shimonishi, A. Sugimura, K. Tashiro, and S. Shimizu. Molecular cloning and expression of human hepatocyte growth factor. *Nature*, 342(6248):440–3, Nov 1989.

[82] K. Nishimura, K. Matsumiya, H. Miura, A. Tsujimura, N. Nonomura, K. Matsumoto, T. Nakamura, and A. Okuyama. Effects of hepatocyte growth factor on urokinase-type plasminogen activator (upa) and upa receptor in du145 prostate cancer cells. *Int J Androl*, 26(3):175–9, Jun 2003.

[83] S. L. Organ and M.-S. Tsao. An overview of the c-met signaling pathway. *Ther Adv Med Oncol*, 3(1 Suppl):S7–S19, Nov 2011.

[84] L. Perko. *Differential equations and dynamical systems*, volume 7. Springer, New York, 3rd ed edition, 2001.

[85] A. Petrelli, G. F. Gilestro, S. Lanzardo, P. M. Comoglio, N. Migone, and S. Giordano. The endophilin-cin85-cbl complex mediates ligand-dependent downregulation of c-met. *Nature*, 416(6877):187–90, Mar 2002.

[86] M. Pickup, S. Novit, and H. Moses. The roles of tgf-beta in the tumour microenvironment. *Nat Rev Cancer*, 13(11):788–99, 2013.

[87] D. Pinto and H. Clevers. Wnt, stem cells and cancer in the intestine. *Biol Cell*, 97(3):185–96, Mar 2005.

[88] S. Potempa and A. J. Ridley. Activation of both map kinase and phosphatidylinositide 3-kinase by ras is required for hepatocyte growth factor/scatter factor-induced adherens junction disassembly. *Mol Biol Cell*, 9(8):2185–200, Aug 1998.

[89] K. A. Rejniak and L. J. McCawley. Current trends in mathematical modeling of tumor-microenvironment interactions: a survey of tools and applications. *Exp Biol Med (Maywood)*, 235(4):411–23, Apr 2010.

[90] T. Reya, S. J. Morrison, M. F. Clarke, and I. L. Weissman. Stem cells, cancer, and cancer stem cells. *Nature*, 414(6859):105–11, Nov 2001.

[91] L. Ricci-Vitiani, D. G. Lombardi, E. Pilozzi, M. Biffoni, M. Todaro, C. Peschle, and R. De Maria. Identification and expansion of human colon-cancer-initiating cells. *Nature*, 445(7123):111–5, Jan 2007.

[92] F. Roletto, A. P. Galvani, C. Cristiani, B. Valsasina, A. Landonio, and F. Bertolero. Basic fibroblast growth factor stimulates hepatocyte growth factor/scatter factor secretion by human mesenchymal cells. *J Cell Physiol*, 166(1):105–11, Jan 1996.

[93] E. F. Saunier and R. J. Akhurst. Tgf beta inhibition for cancer therapy. *Curr Cancer Drug Targets*, 6(7):565–78, Nov 2006.

[94] T. Schatton, N. Y. Frank, and M. H. Frank. Identification and targeting of cancer stem cells. *Bioessays*, 31(10):1038–49, Oct 2009.

[95] S. M. Sheehan, R. Tatsumi, C. J. Temm-Grove, and R. E. Allen. Hgf is an autocrine growth factor for skeletal muscle satellite cells in vitro. *Muscle Nerve*, 23(2):239–45, Feb 2000.

[96] S. Sick, S. Reinker, J. Timmer, and T. Schlake. Wnt and dkk determine hair follicle spacing through a reaction-diffusion mechanism. *Science*, 314(5804):1447–50, Dec 2006.

[97] N. Sidenius and F. Blasi. The urokinase plasminogen activator system in cancer: recent advances and implication for prognosis and therapy. *Cancer Metastasis Rev*, 22(2-3):205–22, 2003.

[98] S. S. Sikandar, K. T. Pate, S. Anderson, D. Dizon, R. A. Edwards, M. L. Waterman, and S. M. Lipkin. Notch signaling is required for formation and self-renewal of tumor-initiating cells and for repression of secretory cell differentiation in colon cancer. *Cancer Res*, 70(4):1469–78, Feb 2010.

[99] V. R. Skeen, I. Paterson, C. Paraskeva, and A. C. Williams. Tgf-1 signalling, connecting aberrant inflammation and colorectal tumorigenesis. *Curr Pharm Des*, 18(26):3874–88, 2012.

[100] M. Sondell, G. Lundborg, and M. Kanje. Vascular endothelial growth factor has neurotrophic activity and stimulates axonal outgrowth, enhancing cell survival and schwann cell proliferation in the peripheral nervous system. *J Neurosci*, 19(14):5731–40, Jul 1999.

[101] M. C. Stella, L. Trusolino, S. Pennacchietti, and P. M. Comoglio. Negative feedback regulation of met-dependent invasive growth by notch. *Mol Cell Biol*, 25(10):3982–96, May 2005.

[102] P. A. Stephens, W. J. Sutherland, and R. P. Freckleton. What is the allee effect? *Oikos*, 87(1):185–190, Oct 1999.

[103] M. Stoker and M. Perryman. An epithelial scatter factor released by embryo fibroblasts. *J Cell Sci*, 77:209–23, Aug 1985.

[104] S. Suzuki, K. Yamanouchi, C. Soeta, Y. Katakai, R. Harada, K. Naito, and H. Tojo. Skeletal muscle injury induces hepatocyte growth factor expression in spleen. *Biochem Biophys Res Commun*, 292(3):709–14, Apr 2002.

[105] Z. A. Syed, W. Yin, K. Hughes, J. N. Gill, R. Shi, and J. L. Clifford. Hgf/c-met/stat3 signaling during skin tumor cell invasion: indications for a positive feedback loop. *BMC Cancer*, 11:180, 2011.

[106] S. Talukdar and S. C. Kundu. A non-mulberry silk fibroin proten based 3d in vitro tumor model for evaluation of anticancer drug activity. *ADvanced Functional Materials*, 22(22):4778–4788, 2012.

[107] K. Tanaka, M. Okigami, Y. Toiyama, Y. Morimoto, K. Matsushita, M. Kawamura, K. Hashimoto, S. Saigusa, Y. Okugawa, Y. Inoue, K. Uchida, T. Araki, Y. Mohri, A. Mizoguchi, and M. Kusunoki. In vivo real-time imaging of chemotherapy response on the liver metastatic tumor microenvironment using multiphoton microscopy. *Oncol Rep*, 28(5):1822–30, Nov 2012.

[108] R. Tatsumi, A. Hattori, Y. Ikeuchi, J. E. Anderson, and R. E. Allen. Release of hepatocyte growth factor from mechanically stretched skeletal muscle satellite cells and role of ph and nitric oxide. *Mol Biol Cell*, 13(8):2909–18, Aug 2002.

[109] R. Tatsumi, Y. Sankoda, J. E. Anderson, Y. Sato, W. Mizunoya, N. Shimizu, T. Suzuki, M. Yamada, R. P. Rhoads, Jr, Y. Ikeuchi, and R. E. Allen. Possible implication of satellite cells in regenerative motoneuritogenesis: Hgf upregulates neural chemorepellent sema3a during myogenic differentiation. *Am J Physiol Cell Physiol*, 297(2):C238–52, Aug 2009.

[110] L. Trusolino, A. Bertotti, and P. M. Comoglio. Met signalling: principles and functions in development, organ regeneration and cancer. *Nat Rev Mol Cell Biol*, 11(12):834–48, Dec 2010.

[111] L. Trusolino, S. Cavassa, P. Angelini, M. Andó, A. Bertotti, P. M. Comoglio, and C. Boccaccio. Hgf/scatter factor selectively promotes cell invasion by increasing integrin avidity. *FASEB J*, 14(11):1629–40, Aug 2000.

[112] A. M. Turing. The chemical basis of morphogenesis. *j-PHILOS-TRANS-R-SOC-LOND-SER-B-BIO-SCI*, B 237(641):37–72, aug 1952.

[113] Y. Ueoka, K. Kato, Y. Kuriaki, S. Horiuchi, Y. Terao, J. Nishida, H. Ueno, and N. Wake. Hepatocyte growth factor modulates motility and invasiveness of ovarian carcinomas via ras-mediated pathway. *Br J Cancer*, 82(4):891–9, Feb 2000.

[114] S. Ulisse, E. Baldini, S. Sorrenti, and M. D'Armiento. The urokinase plasminogen activator system: a target for anti-cancer therapy. *Curr Cancer Drug Targets*, 9(1):32–71, Feb 2009.

[115] N. Verma, O. Keinan, M. Selitrennik, T. Karn, M. Filipits, and S. Lev. Pyk2 sustains endosomal-derived receptor signalling and enhances epithelial-to-mesenchymal transition. *Nat Commun*, 6:6064, 2015.

[116] L. Vermeulen, F. De Sousa E Melo, M. van der Heijden, K. Cameron, J. H. de Jong, T. Borovski, J. B. Tuynman, M. Todaro, C. Merz, H. Rodermond, M. R. Sprick, K. Kemper, D. J. Richel, G. Stassi, and J. P. Medema. Wnt activity defines colon cancer stem cells and is regulated by the microenvironment. *Nat Cell Biol*, 12(5):468–476, May 2010.

[117] T. Watabe and K. Miyazono. Roles of tgf-beta family signaling in stem cell renewal and differentiation. *Cell Res*, 19(1):103–15, Jan 2009.

[118] S. M. Wise. Unconditionally stable finite difference, nonlinear multigrid simulation of the cahn-hilliard-hele-shaw system of equations. *J. Sci. Comput.*, 44(1):38–68, 2010.

[119] S. M. Wise, J. S. Lowengrub, H. B. Frieboes, and V. Cristini. Three-dimensional multispecies nonlinear tumor growth–i model and numerical method. *J Theor Biol*, 253(3):524–43, Aug 2008.

[120] A. Wong, P. Leung, and N. Auersperg. Hepatocyte growth factor promotes in vitro scattering and morphogenesis of humanc cervical carcinomal cells. *Gynocel Oncol*, 78(2):158–65, 2000.

[121] G. H. Xiao, M. Jeffers, A. Bellacosa, Y. Mitsuuchi, G. F. Vande Woude, and J. R. Testa. Anti-apoptotic signaling by hepatocyte growth factor/met via the phosphatidylinositol 3-kinase/akt and mitogen-activated protein kinase pathways. *Proc Natl Acad Sci U S A*, 98(1):247–52, Jan 2001.

[122] X. Xu and M. Thomas. Biphasic actions of estrogen on colon cancer cell growth: possible mediation by high-and low-affinity estrogen binding sites. *Endocrine*, 3(9):661–665, 1995.

[123] M. Yamada, R. Tatsumi, K. Yamanouchi, T. Hosoyama, S.-i. Shiratsuchi, A. Sato, W. Mizunoya, Y. Ikeuchi, M. Furuse, and R. E. Allen. High concentrations of hgf inhibit skeletal muscle satellite cell proliferation in vitro by inducing expression of myostatin: a possible mechanism for reestablishing satellite cell quiescence in vivo. *Am J Physiol Cell Physiol*, 298(3):C465–76, Mar 2010.

[124] T. Yamashita and X. W. Wang. Cancer stem cells in the development of liver cancer. *J Clin Invest*, 123(5):1911–8, May 2013.

[125] S. Yamazaki, J. Skaptason, D. Romero, J. H. Lee, H. Y. Zou, J. G. Christensen, J. R. Koup, B. J. Smith, and T. Koudriakova. Pharmacokinetic-pharmacodynamic modeling of biomarker response and tumor growth inhibition to an orally available cmet kinase inhibitor in human tumor xenograft mouse models. *Drug Metab Dispos*, 36(7):1267–74, Jul 2008.

[126] H. Youssefpour, X. Li, A. D. Lander, and J. S. Lowengrub. Multispecies model of cell lineages and feedback control in solid tumors. *J Theor Biol*, 304:39–59, Jul 2012.

[127] A. Zeuner, M. Todaro, G. Stassi, and R. De Maria. Colorectal cancer stem cells: From the crypt to the clinic. *Cell Stem Cell*, 15(6):692–705, Dec 2014.

[128] L. Zhang, H. Jiang, and Z. Hu. Concentration-dependent effect of nerve growth factor on cell fate determination of neural progenitors. *Stem Cells Dev*, 20(10):1723–31, Oct 2011.

[129] L. Zhang, A. D. Lander, and Q. Nie. A reaction-diffusion mechanism influences cell lineage progression as a basis for formation, regeneration, and stability of intestinal crypts. *BMC Syst Biol*, 6:93, 2012.

Appendices

A Nondimensionalization of Equations (1.1) - (1.23)

The equations are nondimensionalized as in [119, 126]: we take the O diffusion length scale, $l = \sqrt{D_O/\nu_{UOSC}}$, and the mitosis time scale $\tau = (\lambda_{MSC_M}\bar{C}_{AO})^{-1}$, where here λ_{MSC_M} represents the midpoint of the minimum and maximum stem cell division rates. The diffusion length scale, l is estimated $l \sim 150\mu m$ and the mitosis time scale at $\tau \sim 1$ day following [28]. The characteristic tumor pressure is taken to be $\bar{p} = l^2/(\tau\bar{\kappa})$, where $\bar{\kappa}$ is the characteristic value of the pressure-dependent cell-motility, κ. We also take $\bar{C}_{\mathrm{TGF}\beta}$ to be the characteristic concentration of TGFβ, $\bar{C}_M = (\nu_{PMI})^{-1}$, $\bar{C}_{MI} = \bar{C}_{AO}/(\nu_{PMI}\nu_{DM})$, $\bar{C}_{HGF} = \bar{C}_{AO}^2/(\bar{C}_{\mathrm{TGF}\beta})$, and $\bar{C}_{SGF} = \bar{C}_{AO}$. The conservation equations are then taken to be

$$\frac{\partial \phi_*}{\partial t'} = -\nabla' \cdot \mathbf{J}'_* + \mathrm{Src}'_* - \nabla' \cdot (\mathbf{u}'_S \phi_*), \tag{A.1}$$

where $*$ refers to tumor cell species (CSCs, TCs, or DCs). Nondimensionalized variables and parameters are presented in Tables (A.1) and (A.2). For the nondimensionalized equations in the main text, all variables and parameters are rewritten without the prime notation.

Table A.1: Nondimensional variables in Equations (1.24) - (1.35).

Tumor flux	$\mathbf{J}' = Mb'\phi_t \nabla \mu'$
Chemical Potential	$\mu' = (\partial F/\partial \phi_T)(\phi_T) - \epsilon'^2 \nabla'^2 \phi_T$
Velocity	$\mathbf{u}'_\mathbf{s} = \mathbf{u}_\mathbf{s}/(l/\tau)$
Pressure	$p' = p/\bar{p}$
$[O]$	$C'_O = C_O/\bar{C}_{AO}$
[TGFβ]	$C'_{TGF\beta} = C_{TGF\beta}/\bar{C}_{TGF\beta}$
[c-Met]	$C'_M = C'_M/\bar{C}_M$
[c-Met Inhibitors]	$C'_{MI} = C_{MI}/\bar{C}_{MI}$
[HGF]	$C'_{HGF} = C_{HGF}/\bar{C}_{HGF}$
[SGF]	$C'_{SGF} = C_{SGF}/\bar{C}_{SGF}$

Table A.2: Nondimensional parameters in Equations (1.24) - (1.35).

Mobility	$M' = \tau/\tau_M$; $\tau_M = l^2\epsilon/(Mb\gamma)$	Pressure-dependent cell motility	$\kappa' = \kappa/\bar{\kappa}$
Diffuse interface thickness	$\epsilon' = \epsilon/l$	Global adhesion	$\gamma' = \tau/\tau_R$, $\tau_R = \gamma\bar{\kappa}/l^3$
Strength of M action on P_0	$\xi_0' = \xi_0 \cdot \bar{C}_M$	Strengh of TGFβ action on P_0	$\psi_0' = \psi_0 \cdot \bar{C}_{\mathrm{TGF}\beta}$
Strength of M action on λ_{MSC}	$\xi_1' = \xi_1 \cdot \bar{C}_M$	Strengh of TGFβ action on λ_{MSC}	$\psi_1' = \psi_1 \cdot \bar{C}_{\mathrm{TGF}\beta}$
TC mitosis rate	$\lambda'_{MTC} = \tau/\tau_{MTC}$; $\tau_{MTC} = (\lambda_{MTC}\bar{C}_{AO})^{-1}$	TC apoptosis rate	$\lambda'_{ATC} = \tau/\tau_{ATC}$; $\tau_{ATC} = (\lambda_{ATC})^{-1}$
DC lysis rate	$\lambda'_L = \tau \cdot \lambda_L$	Oxygen uptake rate	$\nu'_{UOTC} = \nu_{UOTC}/\nu_{UOSC}$
Oxygen transfer rate	$\nu'_{PO} = \nu_{PO}/\nu_{UOSC}$	TGFβ uptake rate by CSCs	$\nu'_{\mathrm{UTGF}\beta} = \tau_{\mathrm{TGF}\beta} \cdot \nu_{\mathrm{UTGF}\beta}$
TGFβ decay rate	$\nu'_{\mathrm{DTGF}\beta} = \tau_{\mathrm{TGF}\beta} \cdot \nu_{\mathrm{DTGF}\beta}$	TGFβ production rate by TCs	$\nu'_{\mathrm{PTGF}\beta} = \tau_{\mathrm{TGF}\beta} \cdot \nu_{\mathrm{PTGF}\beta}$; $\tau_{\mathrm{TGF}\beta} = l^2/D_{\mathrm{TGF}\beta}$
M diffusion rate	$D'_M = \tau/\tau_M$; $\tau_M = l^2/D_M$	MI diffusion rate	$D'_{MI} = \tau/\tau_{MI}$; $\tau_{MI} = l^2/D_{MI}$
Strength of HGF-independent M activation	$\nu'_0 = \nu_0$	Strength of HGF-induced M activation	$\lambda'_{HGF} = \lambda_{HGF} \cdot \bar{C}_{HGF}$
Ratio of λ_{MSC_M} to ν_{DM}	$R = \tau \cdot \nu_{DM}$	Background M production rate	$\mu'_0 = \mu_0\bar{C}_{AO}/(\bar{C}_M\nu_{DM})$
MI decay rate	$\nu'_{DMI} = \nu_{DMI}/\nu_{DM}$	HGF production rate	$\nu'_{PHGF} = \tau \cdot \nu_{PHGF}$
Regularization constant	$\zeta = \zeta/\bar{C}_{\mathrm{TGF}\beta}$	HGF decay rate	$\nu'_{DHGF} = \tau \cdot \nu_{DHGF}$
SGF production rate by SCs	$\nu_{SGFC} = \tau \cdot \nu_{SGFC}$	SGF production rate by TCs	$\nu_{SGFT} = \tau \cdot \nu_{SGFT}$
SGF decay rate	$\nu'_{DSGF} = \tau \cdot \nu_{DSGF}$	HGF diffusion rate	$D'_{HGF} = \tau/\tau_{HGF}$; $\tau_{HGF} = l^2/D_{HGF}$
SGF diffusion rate	$D'_{SGF} = \tau/\tau_{SGF}$; $\tau_{SGF} = l^2/D_{SGF}$		

A.1 Nondimensionalized parameter values for Equations (1.24) - (1.37)

Here we present all the nondimensional parameter values used in the model for Chapter 1.

Table A.3: Parameters for cell species conservation, HGF-induced cell-spread, and cell velocity.

Parameter	Description	Value
γ	Global adhesion	-0.1
ϵ	Diffuse interface thickness	0.05
Mb	Mobility	10.0
δ_1	Strength of M effect on $F(\phi_T)$	0.02
δ_2	Strength of M effect on $\tilde{E}$, the energy scale	0.02
κ	Pressure-dependent cell motility	1.0

Table A.4: Parameters for the mass-exchange equations.

Parameter	Description	Value
λ_{MTC}	TC mitosis rate	0.1
λ_{ATC}	TC apoptosis rate	0.1
λ_L	DC lysis rate	1.0

Table A.5: Parameters for stem-cell self-renewal and division.

Parameter	Description	Value
P_{min}	Min. CSC self-renewal rate	0.2
P_{max}	Max. CSC self-renewal rate	1.0
ξ_0	Strength of M action on P_0	1.0
ψ_0	Strength of TGFβ action on P_0	1.0
$\lambda_{MSC_{min}}$	Min. CSC mitosis rate	0.5
$\lambda_{MSC_{max}}$	Max. CSC mitosis rate	1.5
ξ_1	Strength of M action on λ_{MSC}	0.5
ψ_1	Strength of TGFβ action on λ_{MSC}	0.5

Table A.6: Parameters for the chemical species O and TGFβ.

Parameter	Description	Value
ν_{UOTC}	Oxygen uptake rate by TCs	1.0
ν_{PO}	Oxygen transfer rate	0.5
$\nu_{\mathrm{UTGF}\beta}$	TGFβ uptake rate by CSCs	0.05
$\nu_{\mathrm{TGF}\beta}$	TGFβ decay rate	0.0
$\nu_{\mathrm{PTGF}\beta}$	TGFβ production rate by TCs	0.1

Table A.7: Parameters for the chemical species M and MI.

Parameter	Description	Value
D_M	Diffusion of M effectors	1.0
D_{MI}	Diffusion of MI effectors	25.0
ν_0	Strength of HGF-independent M activation	1.0
λ_{HGF}	Strength of HGF-induced M activation	0.5
ν_{DM}	M decay rate	1.0
η_M	Background M production rate	0.2
ν_{PMI}	MI production rate	1.0
ν_{DMI}	MI Decay rate	1.0
R	Reaction rate	50.0

Table A.8: Parameters for the chemical species HGF and SGF.

Parameter	Description	Value
ν_{PHGF}	Strength of SGF on HGF activation	{5,10,15}
ν_{DHGF}	HGF decay rate	1.0
D_{HGF}	HGF diffusion rate	0.1
ν_{SGFS}	SGF production rate by CSCs	{5,10,15}
ν_{SGFT}	SGF production rate by TCs	{5,10,15}
ν_{DSGF}	SGF decay rate	1.0
D_{SGF}	SGF diffusion rate	1.0

B Supplementary Information for Chapter 1, 'The HGF/c-Met axis in tumor growth: a multispecies model.'

B.1 Asymmetrical HGF Feedback

The basecase simulations are based on the assumption that $\nu_{\text{SGFS}} = \nu_{\text{SGFT}}$, but this may not be the case. For example, stem (or terminal) cells may produce SGF at a much higher rate than the other tissue type, which may result in a different tumor growth phenotype. To investigate how the tumor would behave under different production rates of SGF by the two compartments, we simulate tumor growth under four different conditions: $\{\nu_{\text{SGFS}}, \nu_{\text{SGFT}}, \nu_H\} = \{15, 0, 5\}, \{15, 0, 15\}, \{0, 15, 5\}, \{0, 15, 15\}$.

In Figure B.1, we observe that production of SGF by only stem cells results in a phenotype qualitatively similar to the original results, whereas in the case of sole terminal cell production of SGF, we observe smaller stem cell spots that tend to cluster together and laterally self-renew along the tumor-host boundary $\lambda_{HGF} = 15.0$. This is due to the higher probability of self-renewal near the stem cell spots and in the interior of the tumor due to the higher concentration of HGF along the tumor-host boundaries (Figure B.1 (b)), causing stem cells to divide and self-renew laterally, rather than outward into the host tissue. Since the dynamics with only stem production of SGF are qualitatively similar to the stem and terminal cell SGF production, we maintain our assumption that $\nu_{\text{SGFS}} = \nu_{\text{SGFT}}$, as the resultant simulation behaves in a similar fashion to the most plausible biological scenarios (either $\nu_{\text{SGFS}} = \nu_{\text{SGFT}}$ or $\nu_{\text{SGFS}} >> \nu_{\text{SGFT}}$).

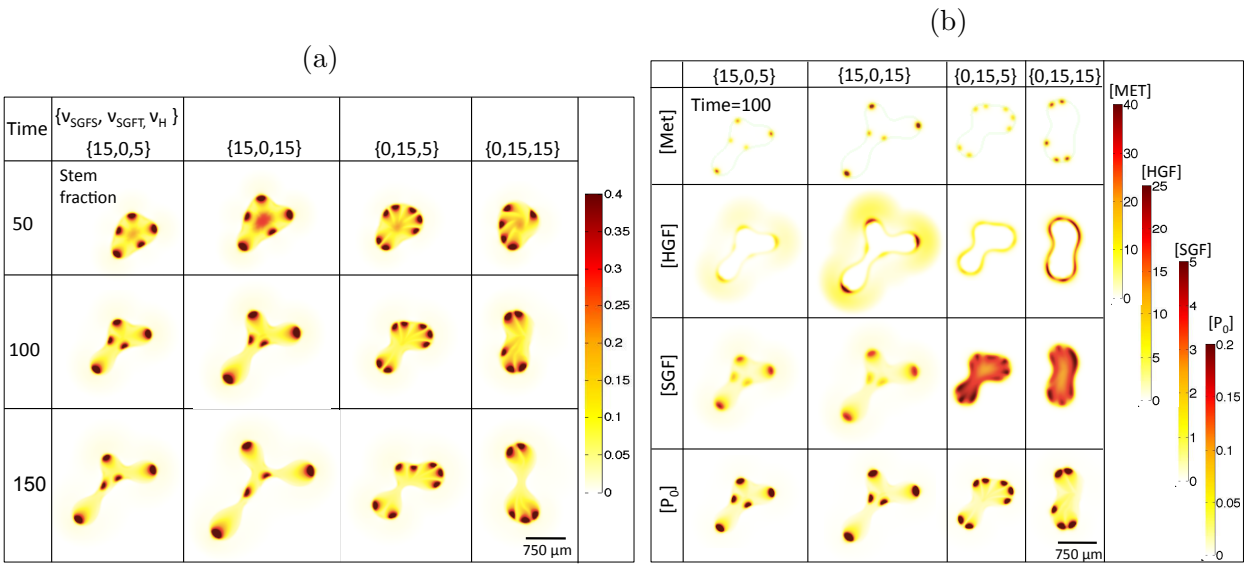

Figure B.1: Asymmetrical SGF production.
(a) Stem cell fraction for T = 50, 100, and 150 and (b) Chemical species and probability of self-renewal for T = 100. SGF production by tumor cells is not assumed to be identical for stem and differentiated cells. The first two columns of (a) and (b) show simulation results from setting SGF production only by stem cells, whereas the last two columns show results from setting SGF production by only terminal cells. The strength of HGF response, ν_H, is also tested with $\nu_H = 5$ for the first and third columns and $\nu_H = 15$ for the second and fourth columns.

B.2 Early Time

Early time evolution of the stem cell fraction for simulations without (Figure B.2 (a)) and with (Figure B.2) (b)) c-Met induced effects on cell dispersal. Loss of spots is evident for higher HGF dynamics, which results in greater heterogeneity of cell type and proliferation rate at the tumor-host boundary at later time (see main text).

B.3 Therapy

We consider how therapy acting on the HGF/c-met axis can be models by changing two parameters: λ_{HGF}, the strength of HGF effect on c-Met activation, and ν_{PM}, the strength of c-Met auto-activation (see Equations (1.19,1.20). Lowering λ_{HGF} represents application of

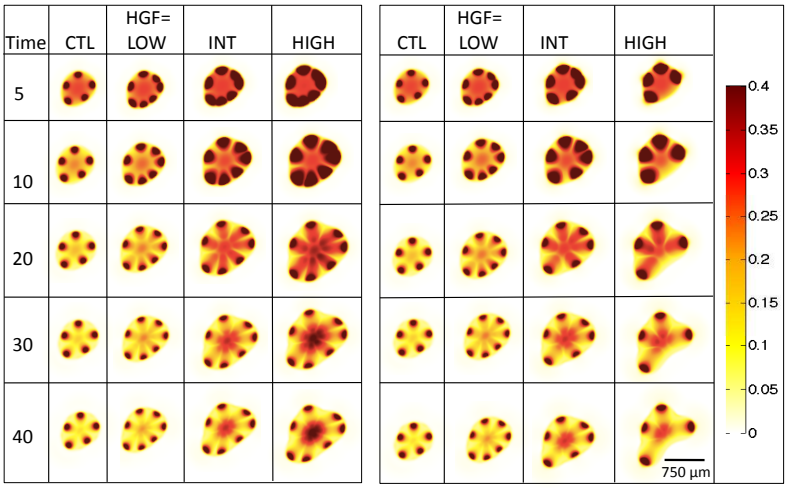

Figure B.2: Stem Cell fraction of early time ($5 \leq T \leq 50$) simulations without (a) and with (b) c-Met-induced cell dispersal.

drugs that either inhibit HGF directly or block HGF binding and c-Met activation. Lowering ν_{PM} along with λ_{HGF} represents anti-c-Met therapy, either by kinase inhibition or inhibition of downstream pathway components (Figure B.3). Two parameter alterations, termed T1 and T2, represent two therapies that are analyzed in the main text. A shorter T2 therapy

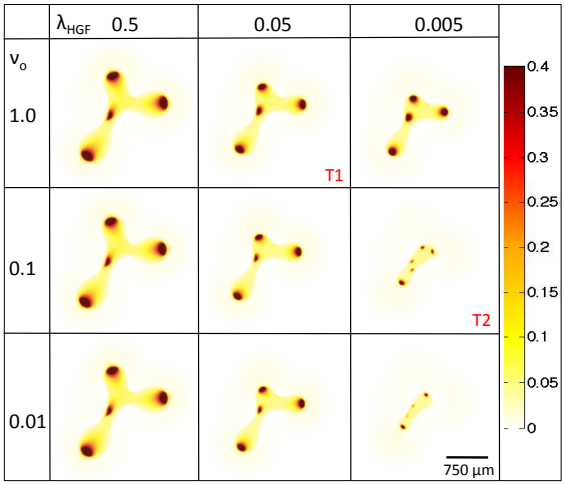

Figure B.3: Stem Cell fraction at T = 100 after therapy applied at T = 50 to the high HGF condition. λ_{HGF} is the strength of HGF effect on c-Met activation and ν_o is the strength of autocrine c-Met activation.

(from T = 50 to T = 100, and returning parameters to original conditions from T = 100 to T = 150) results in rapid tumor regrowth and increase in spot size, indicating that tumor eradication would require surgical treatment and/or combination therapy (Figure B.4).

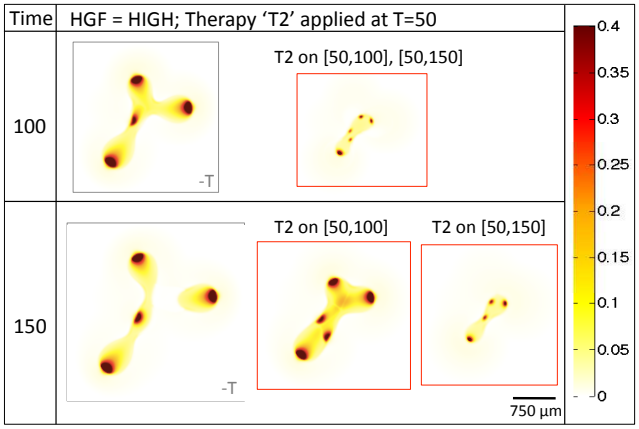

Figure B.4: Stem cell fraction for high HGF condition at T = 100 and T = 150 with therapy T2 applied from T = 50 to T = 100 or to T = 150. Results in main text show therapy results from T = 50 to T = 150. Note that when therapy is only applied until T = 100, tumor regrowth occurs rapidly.

C Approximation of the separatrix for System (3.7) using the Stable Manifold Theorem.

We use the Stable Manifold Theorem (SMT) to approximate the separatrix described in Theorem 3.1 near the equilibrium point $P_2(S_2, A_2)$ of system (3.7). We follow the technique presented in [84]. We recall that P_2 occurs at the unique intersection of the curves $\{p(S,a) = 0.5\}$ and $\{F(S,a) = 0\}$.

C.1 Affine change of coordinates

To apply the SMT, we need to first make the affine change of coordinates: $g : (S,a) \to (S,a) - (S_2, A_2)$. We let $(S^*, a^*) = g(S,a)$. Then, applying g to (3.7), and noting that $(S,a) = (S^*, a^*) + (S_2, A_2)$, and $\frac{\partial}{\partial t}(S,a) = \frac{\partial}{\partial t}((S^*, a^*) + (S_2, A_2)) = \frac{\partial}{\partial t}(S^*, a^*)$, we obtain

$$\begin{aligned} \dot{S^*} &= (2p^*(S^*, a^*) - 1)k(S^* + S_2) = f_1^*(S^*, a^*) \\ \dot{a^*} &= (a^* + A_2)\left(\frac{\beta(S^* + S_2)(a^* + A_2)}{1 + \lambda(a^* + A_2)} - 1\right) = f_2^*(S^*, a^*) \\ p^*(S^*, a^*) &= \frac{\xi_1(a^* + A_2)}{1 + \xi_1(a^* + A_2)} \frac{1}{1 + \xi_2(S^* + S_2)} \end{aligned} \tag{C.2}$$

The Jacobian for (C.2) is

$$J^*(S^*, a^*) = \begin{pmatrix} 2p^*_{S^*}k(S^* + S_2) + (2p^* - 1)k & 2p^*_{a^*}k(S^* + S_2) \\ (f_1)_{S^*} & (f_1)_{a^*} \end{pmatrix},$$

where

$$\begin{aligned} p^*_{S^*} &= \frac{-\xi_1\xi_2(a^*+A_2)}{(1+\xi_1(a^*+A_2))(1+\xi_2(S^*+S_2))^2} \\ p^*_{a^*} &= \frac{\xi_1}{(1+\xi_2(S^*+S_2))(1+\xi_1(a^*+A_2))^2} \\ (f_2^*)_{S^*} &= \frac{\beta(a^*+A_2)^2}{1+\lambda(a^*+A_2)} \\ (f_2^*)_{a^*} &= \frac{\beta(S^*+S_2)(a^*+A_2)(2+\lambda(a^*+A_2))}{(1+\lambda(a^*+A_2))^2} - 1 \end{aligned} \tag{C.3}$$

In this coordinate system, $(S^*, a^*) = (0, 0)$ is an equilibrium point and $P^*(0, 0)$ corresponds to $P_2(S_2, A_2)$. To use the SMT, we need to first determine $A = Df(0) = J^*(0, 0)$. We have

$$A = J^*(0,0) = \begin{pmatrix} 2p^*_{S^*}(0,0)kS_2 & 2p^*_{a^*}(0,0)kS_2 \\ (f_2)_{S^*}(0,0) & (f_2)_{a^*}(0,0) \end{pmatrix} \tag{C.4}$$

We first note, as in the original $J(S_1, S_2)$, that since $p^*_{S^*} < 0$ and $F_{a^*} > 0$, $2p^*_{S^*}(0, 0)kS_2(f_2)_{a^*}(0, 0) < 0$ and since $p^*_{a^*} > 0$ and $(f_2^*)_{S^*} > 0$, $2p^*_{a^*}(0, 0)kS_2(f_2)_{S^*}(0, 0) > 0$. Therefore,

$$\det J^*(0,0) = 2p^*_{S^*}(0,0)kS_2)(f_2^*)_{a^*}(0,0) - 2p^*_{a^*}(0,0)kS_2(f_2^*)_{S^*}(0,0) < 0,$$

and hence $J^*(0, 0)$ has one positive and one negative eigenvalue, and P^* is a saddlepoint. We also recall that S_2 and A_2 satisfy

$$\begin{cases} \dfrac{\xi_1 A_2}{1+\xi_1 A_2}\dfrac{1}{1+\xi_2 S_2} = 0.5 \\ \dfrac{\beta S_2 A_2}{1+\lambda A_2} = 1 \end{cases} \tag{C.5}$$

Using (C.5), we simplify (C.3) to calculate the elements of A,

$$\begin{aligned} p^*_{S^*}(0,0) &= \frac{-A_2\xi_1\xi_2}{(1+\xi_1A_2)(1+\xi_2S_2)^2} = \frac{-\xi_2}{2(1+\xi_2S_2)} \\ p^*_{a^*}(0,0) &= \frac{1}{(1+\xi_2S_2)(1+\xi_1A_2)^2} = \frac{1}{2A_2(1+\xi_1A_2)} \\ (f^*_2)_{S^*}(0,0) &= \frac{\beta A_2^2}{1+\lambda A_2} = \frac{A_2}{S_2} \\ (f^*_2)_{a^*}(0,0) &= \frac{\beta S_2A_2(2+\lambda A_2)}{(1+\lambda A_2)^2} - 1 = \frac{2+\lambda A_2}{1+\lambda A_2} - 1 = \frac{1}{1+\lambda A_2}, \end{aligned} \tag{C.6}$$

Substituting (C.6) into (C.4), we have the following expression for $A = J^*(0,0)$,

$$A = \begin{pmatrix} \dfrac{-\xi_2kS_2}{1+\xi_2S_2} & \dfrac{kS_2}{A_2(1+\xi_1A_2)} \\ \dfrac{A_2}{S_2} & \dfrac{1}{1+\lambda A_2} \end{pmatrix} \tag{C.7}$$

C.2 Preliminary calculations for the SMT

Following [84] and taking $x = (S^*, a^*)$, we can rewrite the system (C.2) as

$$\dot{x} = Ax + F(x), \tag{C.8}$$

where $A = J^*(0,0)$ and $F(x) = f^*(x) - Ax$. We next need to find an invertible matrix C such that

$$B = C^{-1}AC = \begin{pmatrix} L_1 & 0 \\ 0 & L_2 \end{pmatrix}, \tag{C.9}$$

where L_1 and L_2 are the negative and positive eigenvalues, respectively, of $A = (A_{ij})$. We first calculate the trace, T, and determinant, D, of A,

$$\begin{aligned} T &= A_{11} + A_{22} = \frac{-\xi_2 k S_2}{1+\xi_2 S_2} + \frac{1}{1+\lambda A_2}, \\ D &= A_{11}A_{22} - A_{12}A_{21} = \frac{-\xi_2 k S_2}{1+\xi_2 S_2}\frac{1}{1+\lambda A_2} - \frac{k S_2}{A_2(1+\xi_1 A_2)}\frac{A_2}{S_2} \\ &= \frac{-\xi_2 k S_2}{(1+\xi_2 S_2)(1+\lambda A_2)} - \frac{k}{1+\xi_1 A_2}. \end{aligned}$$

We note, from the calculations above, that $D < 0$. We proceed to calculate $0 = \det(A - LI)$ to obtain the quadratic equation

$$0 = L^2 - (A_{11} + A_{22})L + (A_{11}A_{22} - A_{12}A_{21}) = L^2 - TL + D.$$

The quadratic formula gives us:

$$L_{1,2} = \frac{T \mp (T^2 - 4D)^{1/2}}{2} = T/2 \mp (T^2/4 - D)^{1/2}$$

Since $D < 0$, we find that $L_{1,2}$ are both real and have opposite sign, hence $L_1 < 0 < L_2$. It can be verified that $v_1 = [(L_1 - A_{22}), A_{21}]'$ and $v_2 = [(L_2 - A_{22}), A_{21}]'$ are eigenvectors corresponding (respectively) to L_1 and L_2. Therefore, we have

$$A = CBC^{-1} = \frac{1}{A_{21}(L_1 - L_2)} \begin{pmatrix} L_1 - A_{22} & L_2 - A_{22} \\ A_{21} & A_{21} \end{pmatrix} \begin{pmatrix} L_1 & 0 \\ 0 & L_2 \end{pmatrix} \begin{pmatrix} A_{21} & -L_2 + A_{22} \\ -A_{21} & L_1 - A_{22} \end{pmatrix}$$

We make another change of variables, taking $y = C^{-1}(x)$, and writing (C.8) as

$$\dot{y} = By + G(y), \tag{C.10}$$

where B is from (C.9) and $G(y) = C^{-1}F(Cy)$.

C.3 Applying the SMT

By the SMT (taking $a = (a_1, a_2)$),

$$u(t,a) = U(t)a + \int_0^t U(t-s)G(u(s,a))ds - \int_t^\infty V(t-s)G(u(s,a))ds \tag{C.11}$$

is the solution to (C.10), where

$$U(t) = \begin{pmatrix} e^{L_1 t} & 0 \\ 0 & 0 \end{pmatrix} \text{ and } V(t) = \begin{pmatrix} 0 & 0 \\ 0 & e^{L_2 t} \end{pmatrix}.$$

We solve for u using the method of successive approximation. We let $u^{(0)}(t,a) = 0$ and

$$u^{(j+1)}(t,a) = U(t)a + \int_0^t U(t-s)G(u^{(j)}(s,a))ds - \int_t^\infty V(t-s)G(u^{(j)}(s,a))ds. \tag{C.12}$$

To solve for $j = 1$, we note that $G(0) = C^{-1}F(C \cdot 0) = C^{-1}F(0) = 0$ since $f_1(0,0) = f_2(0,0) = 0$. Therefore,

$$u^{(1)}(t,a) = \begin{pmatrix} e^{L_1 t}a_1 \\ 0 \end{pmatrix}$$

For the next approximation, we first calculate $U(t-s)G(u^{(1)}(s,a)) = U(t-s)C^{-1}F(Cw) = H_1F(Cw)$, where $H_1 = U(t-s)C^{-1}$ and $w = (e^{L_1 s}a_1, 0)'$. Simplifying H_1 gives us:

$$\begin{aligned} H_1 = U(t-s)C^{-1} &= \frac{1}{A_{21}(L_1 - L_2)} \begin{pmatrix} e^{L_1(t-s)} & 0 \\ 0 & 0 \end{pmatrix} \begin{pmatrix} A_{21} & A_{22} - L_2 \\ -A_{21} & L_1 - A_{22} \end{pmatrix} \\ &= e^{L_1(t-s)} \begin{pmatrix} \frac{1}{L_1 - L_2} & \frac{A_{22} - L_2}{A_{21}(L_1 - L_2)} \\ 0 & 0 \end{pmatrix} \end{aligned}$$

Then,

$$H_1F(Cw) = e^{L_1(t-s)}\begin{pmatrix} \frac{1}{L_1-L_2} & \frac{A_{22}-L_2}{A_{21}(L_1-L_2)} \\ 0 & 0 \end{pmatrix}\left[\begin{pmatrix} f_1(Cy) \\ f_2(Cy) \end{pmatrix} - e^{L_1 s}a_1\begin{pmatrix} A_{11} & A_{12} \\ A_{21} & A_{22} \end{pmatrix}\begin{pmatrix} L_1 - A_{22} \\ A_{21} \end{pmatrix}\right]$$
$$= e^{L_1(t-s)}\begin{pmatrix} \frac{f_1(Cy)}{(L_1-L_2)} + \frac{f_2(Cy)A_{22}-L_2}{A_{21}(L_1-L_2)} \\ 0 \end{pmatrix} - e^{L_1 t}a_1\begin{pmatrix} \frac{L_1(T-L_2)-D}{L_1-L_2} \\ 0 \end{pmatrix}. \tag{C.13}$$

Hence,

$$\int_0^t U(t-s)G(u^{(1)}(s,a)) = \int_0^t e^{L_1(t-s)}\begin{pmatrix} \frac{f_1(Cy)}{(L_1-L_2)} + \frac{f_2(Cy)A_{22}-L_2}{A_{21}(L_1-L_2)} \\ 0 \end{pmatrix} ds - t\left[e^{L_1 t}a_1\begin{pmatrix} \frac{L_1(T-L_2)-D}{L_1-L_2} \\ 0 \end{pmatrix}\right] \tag{C.14}$$

We note that our stable manifold will be of the form $y_2 = \psi_2^{(2)}(y_1)$, where $\psi_2^{(2)}(a_1) = u_2^{(2)}(0, a_1, 0)$. Since $U(t)a$ and (C.14) only contribute trivially to $u_2^{(2)}$, we will not perform further calculations on them. Next, we calculate $V(t-s)G(u^{(1)}(s,a)) = V(t-s)C^{-1}F(Cw) = H_2F(Cw)$. As before, we first calculate H_2:

$$H_2 = V(t-s)C^{-1} = \frac{1}{A_{21}(L_1-L_2)}\begin{pmatrix} 0 & 0 \\ 0 & e^{L_2(t-s)} \end{pmatrix}\begin{pmatrix} A_{21} & A_{22}-L_2 \\ -A_{21} & L_1 - A_{22} \end{pmatrix}$$
$$= e^{L_2(t-s)}\begin{pmatrix} 0 & 0 \\ \frac{-1}{L_1-L_2} & \frac{L_1-A_{22}}{A_{21}(L_1-L_2)} \end{pmatrix}$$

We thus have ,

$$H_2F(Cw) = e^{L_2(t-s)}\begin{pmatrix} 0 & 0 \\ \frac{-1}{L_1-L_2} & \frac{L_1-A_{22}}{A_{21}(L_1-L_2)} \end{pmatrix}\left[\begin{pmatrix} f_1(Cw) \\ f_2(Cw) \end{pmatrix} - e^{L_1 s}a_1\begin{pmatrix} A_{11} & A_{12} \\ A_{21} & A_{22} \end{pmatrix}\begin{pmatrix} L_1 - A_{22} \\ A_{21} \end{pmatrix}\right]$$
$$= e^{L_2(t-s)}\begin{pmatrix} 0 \\ \frac{-f_1(Cw)}{L_1-L_2} + \frac{f_2(Cw)(L_1-A_{22})}{A_{21}(L_1-L_2)} \end{pmatrix} - e^{s(L_1-L_2)}e^{L_2 t}\begin{bmatrix} 0 \\ g(L_1, L_2, A_{21}, A_{22}) \end{bmatrix}$$

Taking the integral of the right-hand term on the domain $[t, \infty)$ gives us $\frac{e^{L_1 t}}{L_2-L_1}(0, g(\cdot))'$. We find that $g(\cdot) = L_1^2 - TL_1 + D = 0$. Therefore, this term does not contribute to the stable manifold.

The SMT allows us to calculate the second approximation to the separatrix, $\mathrm{M}^* = u_2^{(2)}(0, a_1, 0)$, as

$$\mathrm{M}^* = \frac{1}{L_1 - L_2}\left(\int_0^\infty -e^{-L_2 s}f_1^*(Cw)ds + \frac{L_1 - A_{22}}{A_{21}}\int_0^\infty e^{-L_2 s}f_2^*(Cw)ds\right), \tag{C.15}$$

where $Cw = e^{L_1 s}a_1(L_1 - A_{22}, A_{21})'$, and by (C.2),

$$f_1^*(Cw) = \left(\frac{2\xi_1(e^{L_1 s}a_1A_{21} + A_2)}{(1 + \xi_1(e^{L_1 s}a_1A_{21} + A_2))(1 + \xi_2(e^{L_1 s}a_1(L_1 - A_{22}) + S_2))} - 1\right)k(e^{L_1 s}a_1(L_1 - A_{22}) + S_2) \tag{C.16}$$

$$f_2^*(Cw) = (e^{L_1 s}a_1A_{21} + A_2)\left(\frac{\beta(e^{L_1 s}a_1(L_1 - A_{22}) + S_2)(e^{L_1 s}a_1A_{21} + A_2)}{1 + \lambda(e^{L_1 s}a_1A_{21} + A_2)} - 1\right) \tag{C.17}$$

We now solve $-\int_0^\infty I_1 ds = \int_0^\infty e^{-L_2 s}f_1^*(Cw)ds$ and $\int_0^\infty I_2 ds = \int_0^\infty e^{-L_2 s}f_2^*(Cw)ds$. Substituting (C.16) into I_1, we obtain

$$I_1 = \left(\frac{2\xi_1 e^{-L_2 s}(e^{L_1 s}a_1A_{21} + A_2)}{(1 + \xi_1(e^{L_1 s}a_1A_{21} + A_2))(1 + \xi_2(e^{L_1 s}a_1(L_1 - A_{22}) + S_2))} - e^{-L_2 s}\right)k(e^{L_1 s}a_1(L_1 - A_{22}) + S_2) \tag{C.18}$$

We split I_1 into three parts:

$$\begin{aligned} I_1 &= I_{11} + I_{12} + I_{13} \\ &= \frac{(2\xi_1 e^{-L_2 s}(e^{L_1 s} a_1 A_{21} + A_2)k(e^{L_1 s} a_1 (L_1 - A_{22}) + S_2)}{(1 + \xi_1(e^{L_1 s} a_1 A_{21} + A_2))(1 + \xi_2(e^{L_1 s} a_1 (L_1 - A_{22}) + S_2)} \\ &- k e^{(L_1 - L_2)s} a_1 (L_1 - A_{22}) - e^{-L_2 s} k S_2. \end{aligned}$$

We can directly integrate I_{12} and I_{13} to obtain

$$-\int_0^\infty I_1 ds = -\int_0^\infty I_{11} ds - \frac{k a_1 (L_1 - A_{22})}{L_1 - L_2} + \frac{k S_2}{L_2}. \tag{C.19}$$

We now work to simplify I_{11} by taking $u = e^{L_1 s}$. The change of variables gives us

$$\begin{aligned} -\int_0^\infty I_{11} ds &= -\frac{2k}{L_1} \int_{u_1}^{u_2} u^{-T/L_1} \frac{(u a_1 A_{21} + A_2)(u a_1 (L_1 - A_{22}) + S_2)}{(1 + \xi_1(u a_1 A_{21} + A_2))(1 + \xi_2(u a_1 (L_1 - A_{22}) + S_2))} du \\ &= \frac{2\xi_1 k}{L_1} \int_0^1 u^{-T/L_1} \frac{(u c_1 + A_2)(u c_2 + S_2)}{(1 + \xi_1(u c_1 + A_2))(1 + \xi_2(u c_2 + S_2))} du, \end{aligned} \tag{C.20}$$

where we find that $u_1 = 1$ and $u_2 = \lim_{s \to \infty} e^{L_1 s} = 0$ since $L_1 < 0$. We take $c_1 = a_1 A_{21}$ and $c_2 = a_1(L_1 - A_{22})$.

We would like to do a partial fraction decomposition for the integrand term in (C.20) not containing u^{-T/L_1}, I_{11}^*. Noting that both the numerator and denominator are of degree 2, we first perform long division to obtain a fraction p/q where deg $p <$ deg q. Fully multiplying the terms in the fraction, and setting $c_3 = A_2 c_2 + S_2 c_1$ and $c_4 = A_2 \xi_1 + S_2 \xi_2 + A_2 S_2 \xi_1 \xi_2 + 1$ gives us

$$\begin{aligned} I_{11}^* &= \frac{u^2 c_1 c_2 + u c_3 + A_2 S_2}{u^2 \xi_1 \xi_2 c_1 c_2 + u(\xi_1 \xi_2 c_3 + \xi_2 c_2 + \xi_1 c_1) + c_4} \\ &= \frac{1}{\xi_1 \xi_2} - \frac{u(c_2/\xi_1 + c_1/\xi_2) + (A_2/\xi_2 + S_2/\xi_1 + 1/(\xi_1 \xi_2))}{(1 + \xi_1(u c_1 + A_2))(1 + \xi_2(u c_2 + S_2))} \end{aligned} \tag{C.21}$$

Setting $c_5 = c_2/\xi_1 + c_1/\xi_2$ and $c_6 = A_2/\xi_2 + S_2/\xi_1 + 1/(\xi_1 \xi_2)$, the second term of (C.21)

becomes

$$\frac{uc_5 + c_6}{(1+\xi_1(uc_1+A_2))(1+\xi_2(uc_2+S_2))} = \frac{P_1}{(1+\xi_1(uc_1+A_2))} + \frac{P_1}{(1+\xi_2(uc_2+S_2))},$$

where

$$P_1 = \frac{-c_5(\xi_1 A_2 + 1) + c_1 c_6 \xi_1}{\xi_1\xi_2(c_1 S_2 - A_2 c_2) + c_1\xi_1 - c_2\xi_2}$$

$$P_2 = \frac{-c_5(\xi_2 S_2 + 1) + c_2 c_6 \xi_2}{\xi_1\xi_2(-c_1 S_2 + A_2 c_2) - c_1\xi_1 + c_2\xi_2}$$

Therefore, the integrand in (C.20), $u^{-T/L_1} I_{11}^*$, can be written as

$$u^{-T/L_1} I_{11}^* = u^{-T/L_1}\left(\frac{1}{\xi_1\xi_2} - \frac{P_1}{(1+\xi_1(uc_1+A_2))} - \frac{P_2}{(1+\xi_2(uc_2+S_2))}\right)$$

We note that the first term can be integrated,

$$\frac{2\xi_1 k}{L_1\xi_1\xi_2}\int_0^1 u^{-T/L_1} du = \frac{-2k}{L_2\xi_1\xi_2} u^{-L_1/L_2},$$

where the first equality comes about from the observation that $-T/L_1 = -1 - L_2/L_1$. To summarize, if we set

$$I_{11}^{**} = u^{-T/L_1}\left(\frac{P_1}{(1+\xi_1(uc_1+A_2))} + \frac{P_2}{(1+\xi_2(uc_2+S_2))}\right)$$

We can rewrite (C.19) as

$$-\int_0^\infty I_1 ds = \frac{kS_2}{L_2} - \frac{kC_2}{L_1 - L_2} - \frac{2\xi_1 k}{L_2\xi_1\xi_2} - \frac{2\xi_1 k}{L_1}\int_0^1 I_{11}^{**} du \tag{C.22}$$

To solve $\int_0^1 I_{11}^{**} du$, we will need to use a hypergeometric function and the beta function.

Indeed, we have the formula

$$\int_0^1 t^{b-1}(1-t)^{c-b-1}(1-tx)^{-a}dt = B(b,c-b)_2F_1(a,b;c;x)$$

where $B(a,b) = \int_0^a t^{a-1}(1-t)^{b-1}dt$ and ${}_2F_1(a_1,a_2;b_1;x) = \sum_{k=0}^{\infty} \frac{(a_1)_k(a_2)_k}{(b_1)_k}\frac{x^k}{k!}$. In our case, we split I_{11}^{**} naturally as a sum of two terms, and for the first integral, we have $b-1 = -T/L_1$, hence $b = 1 - T/L_1 = -L_2/L_1$, $0 = c-b-1$, hence $c = b+1 = 2-T/L_1$, $a = 1$, and $x = (-\xi_1 C_1)/(\xi_1 A_2 + 1)$, where we have pulled $(\xi_1 A_2 + 1)^{-1}$ from the denominator. We want to first find an explicit representation for $B(b,c-b)$,

$$B(b,c-b) = B(-T/L_1+1,1) = \int_0^1 t^{-T/L_1}dt = \frac{1}{-L_2/L_1}t^{-T/L_1+1}|_0^1 = \frac{-L_1}{L_2}.$$

Using the hypergeometric function and (C.22), our final formula for $-\int_0^\infty I_1 ds = \int_0^\infty -e^{L_2 s}f_1^*(Cw)ds$ is

$$-\int_0^\infty I_1 ds = k\left(\frac{S_2}{L_2} - \frac{C_2}{L_1-L_2} - \frac{2}{L_2\xi_2} + \frac{2\xi_1 P_1}{L_2(\xi_1 A_2+1)}{}_2F_1^1 + \frac{2\xi_1 P_2}{L_2(\xi_2 S_2+1)}{}_2F_1^2\right), \quad \text{(C.23)}$$

where

$${}_2F_1^1 =_2 F_1\left(1, -L_2/L_1; 1-L_2/L_1; \frac{-\xi_1 c_1}{\xi_1 A_2 + 1}\right)$$

and

$${}_2F_1^2 = 2F_1\left(1, -L_2/L_1; 1-L_2/L_1; \frac{-\xi_2 c_2}{\xi_2 S_2 + 1}\right)$$

We now begin work to solve $\int_0^\infty I_2 ds = \int_0^\infty e^{-L_2 s}f_2(Cw)ds$. Using the same substitution as

earlier, i.e. $u = e^{L_1 s}$, and again taking $c_1 = a_1 A_{21}$ and $c_2 = a_1(L_1 - A_{22})$, we obtain

$$\begin{aligned}\int_0^\infty I_2 ds &= \frac{-1}{L_1}\int_0^1 u^{-T/L_1}(uc_1 + A_2)\left(\frac{\beta(uc_2+S_2)(uc_1+A_2)}{1+\lambda(uc_1+A_2)} - 1\right), \\ &= \frac{-\beta}{L_1}\int_0^1 u^{-T/L_1}\frac{(uc_2+S_2)(uc_1+A_2)^2}{1+\lambda(uc_1+A_2)}du + \frac{1}{L_1}\int_0^1 u^{-T/L_1+1}c_1 + u^{-T/L_1}A_2 du, \\ &= \frac{-\beta}{L_1}\int_0^1 u^{-T/L_1}\left(c_3^* u^2 + c_4^* u + c_5^* + \frac{c_6^*}{\lambda u c_1 + \lambda A_2 + 1}\right)du + \frac{c_1}{L_1 - L_2} + \frac{-A_2}{L_2},\end{aligned} \tag{C.24}$$

where the last equality comes from long division in the first integral and full integration of the second. The constants are as follows:

$$c_3^* = \frac{c_1 c_2}{\lambda},\ c_4^* = \frac{c_2 A_2 + c_1 S_2}{\lambda} - \frac{c_2}{\lambda^2},\ c_5^* = \frac{c_2}{c_1\lambda^3} + \frac{S_2(A_2-1)}{\lambda^2},\ c_6^* = \frac{-1}{\lambda^3} + \frac{S_2 - (A_2 c_2/c_1)}{\lambda^2}.$$

We concentrate now on the first integral in (C.24). The first three terms multiplied by u^{-T/L_1} can be integrated in a straight-forward manner. The last one can be integrated using a hypergeometric function as described earlier. We thus obtain

$$\int_0^\infty I_2 ds = -\beta\left(\frac{c_3^*}{2L_1 - L_2} + \frac{c_4^*}{L_1 - L_2} - \frac{c_5^*}{L_2}\right) + \frac{\beta c_6^*}{L_2(1+\lambda A_2)}{}_2F_1^3 + \frac{c_1}{L_1 - L_2} - \frac{A_2}{L_2}, \tag{C.25}$$

where ${}_2F_1^3 = {}_2F_1\left(1, -L_2/L_1; 1 - L_2/L_1; \frac{-\lambda c_1}{1+\lambda A_2}\right)$. Therefore, using (C.15),(C.23), and (C.25) we obtain an explicit solution for M*,

$$\begin{aligned}\mathrm{M}^* = &\frac{k}{L_1 - L_2}\left(\frac{S_2}{L_2} - \frac{c_2}{L_1 - L_2} - \frac{2}{L_2\xi_2} + \frac{2P_1\xi_1}{L_2(\xi_1 A_2 + 1)}{}_2F_1^1 + \frac{2P_2\xi_1}{L_2(\xi_2 S_2 + 1)}{}_2F_1^2\right) \\ &+ \frac{L_1 - A_{22}}{(L_1 - L_2)A_{21}}\left(-\beta\left(\frac{c_3^*}{2L_1 - L_2} + \frac{c_4^*}{L_1 - L_2} - \frac{c_5^*}{L_2}\right) + \frac{\beta c_6^*}{L_2(1+\lambda A_2)}{}_2F_1^3 + \frac{c_1}{L_1 - L_2} - \frac{A_2}{L_2}\right),\end{aligned} \tag{C.26}$$

where the constants and hypergeometric functions are specified earlier.

C.4 Linear and Quadratic approximation of M*

We take a linear and quadratic portion of M* in order to obtain approximate interpretable results. Using the expansion for the hypergeometric function, and noting that the untransformed stable manifold will intersect $(0,0)$, we remove all nonlinear terms and rewrite M* as $y_2 = my_1$, where m is the slope of the line y_2 to obtain

$$y_2 = \frac{-y_1}{(L_1 - L_2)^2} c_7, \tag{C.27}$$

where c_7 is the constant

$$\begin{aligned} c_7 = &\frac{2P_1\xi_1^2 A_{21} k}{(\xi_1 A_2 + 1)^2} + \frac{2P_2\xi_1\xi_2 k(L_1 - A_{22})}{(\xi_2 S_2 + 1)^2} \\ &- (L_1 - A_{22}) + \frac{L_1 - A_{22}}{A_{21}} \left(-\beta c_4^{**} + A_{21} + \frac{\beta c_6^{**} A_{21} \lambda}{(1 + \lambda A_2)^2} \right), \end{aligned} \tag{C.28}$$

where $c_4^{**} = c_4^*/y_1$ and $c_6^{**} = c_6^*/y_1$. Next, since $(S^*, a^*) = x = Cy$, we can obtain

$$a^* = S^* \left(\frac{(L_1 - L_2)^2 - c_7}{(L_1 - A_{22})(L_1 - L_2)^2 + (-L_2 + A_{22})c_7} \right) A_{21}$$

Keeping all quadratic terms, we obtain

$$y_2 = \frac{-(y_1)^2}{(L_1 - L_2)(2L_1 - L_2)} c_8 - \frac{-y_1}{(L_1 - L_2)^2} c_7 \tag{C.29}$$

where

$$c_8 = -2\xi_1 \left(\frac{P_1 \xi_1^2 k A_{21}^2}{(\xi_1 A_2 + 1)^3} + \frac{P_2 \xi_2^2 (L_1 - A_{22})^2}{(\xi_2 S_2 + 1)^3} \right) + \frac{L_1 - A_{22}}{A_{21}} \left(\frac{-\beta}{\lambda} A_{21}(L_1 - A_{22}) - \frac{\beta c_6^{**} A_{21}^2 \lambda^2}{(1 + \lambda A_2)^3} \right)$$

The system can be solved for $x = (S^*, a^*)$ using the quadratic formula.